Technische Universität München
Max-Planck-Institut für Plasmaphysik

PhD Thesis

Radiative Cooling of the Divertor Plasma with Argon and Nitrogen Seeding in the ASDEX Upgrade Tokamak

Ferdinand Hitzler

01.10.2020

Fakultät für Physik

Radiative Cooling of the Divertor Plasma with Argon and Nitrogen Seeding in the ASDEX Upgrade Tokamak

Ferdinand Hitzler

Vollständiger Abdruck der von der Fakultät für Physik der Technischen Universität München zur Erlangung des akademischen Grades eines Doktors der Naturwissenschaften genehmigten Dissertation.

Vorsitzender: Prof. Dr. Friedrich C. Simmel

Prüfende der Dissertation:

1. Prof. Dr. Ulrich Stroth
2. Prof. Dr. Martin Zacharias

Die Dissertation wurde am 01.10.2020 bei der Technischen Universität München eingereicht und durch die Fakultät für Physik am 20.11.2020 angenommen.

Abstract

Nuclear fusion in magnetic confinement fusion devices is a promising candidate for a sustainable, climate-neutral and hazard-free base load power supply of the future. One of the major challenges for the operation of a future fusion reactor is the power exhaust. In the planned demonstration reactor DEMO, in an unmitigated scenario, peak power loads of more than $100\,\mathrm{MWm^{-2}}$ are expected at the divertor targets. This considerably exceeds the stationary material limits, which are in the order of $5-10\,\mathrm{MWm^{-2}}$. Additionally, the temperatures at the divertor targets have to be limited to 5 eV to avoid excessive erosion of target material. Therefore, a controlled injection of impurities into the plasma, so-called impurity seeding, is applied, which results in radiative power dissipation and a significant reduction of the target temperatures and power loads. Unfortunately, if the impurities are accumulated in the confined plasma region, they can also cause a considerable confinement degradation and fuel dilution. Consequently, for the operation of a future fusion reactor, it will be crucial to find an optimum seeding recipe which provides sufficient power dissipation, and at the same time ensures a minimal detrimental impact on the confined plasma and the burn conditions. For this purpose different impurity species have to be investigated and compared to each other, in order to improve the physical understanding of the impact of impurities on the plasma and to provide better predictive capabilities.

In this work plasma simulations with the scrape-off layer transport code SOLPS 5.0 are employed, based on H-mode plasmas in the experimental ASDEX Upgrade tokamak. In the simulations, the impurity species argon and nitrogen, as well as different mixing ratios of both species are investigated. Nitrogen shows considerably less core radiation compared to argon at comparable divertor conditions (i.e., at similar target temperatures and peak power loads). However, at the same time nitrogen seeding leads to stronger fuel dilution. These properties can be explained by the different impurity radiation efficiencies and differences in the impurity density distributions. A trade-off between core radiation and fuel dilution can be achieved by mixing both impurities.

An analysis of the impurity transport reveals that the impurities lead to a modification of the main ion background plasma flows. This is due to the impact of the

impurities on the main ion ionization sources in the divertor region. The impact is stronger with argon than with nitrogen, which can be attributed to the differences in the radiation efficiency. Due to the friction between main ions and impurities, the modified background plasma flow also strongly affects the impurity transport. Additionally, the modification of the impurity transport is further enhanced by an increasing thermal force acting on the impurities in the scrape-off layer.

Furthermore, the divertor impurity retention is investigated, which is determined by the neutral ionization front and the impurity stagnation point position. A simplified model is developed, which captures the key features relevant for the dependence of the divertor retention on different plasma parameters. The results of the model suggest, that with decreasing temperatures (i.e., with increasing impurity seeding) the divertor retention decreases. As according to the technological constraints low temperatures are required at the divertor targets, this is a critical result, making it even more challenging to overcome the power exhaust problem.

With the modified plasma transport and the reduced impurity retention in the outer divertor, the modification of the argon impurity density distribution which is observed at high impurity seeding levels can be explained. In this argon density redistribution, the argon impurities are shifted from the outer to the inner divertor, as soon as a certain impurity seeding level is exceeded. The impurity redistribution is much less pronounced for nitrogen, which can be explained by a lower nitrogen divertor retention and by the weaker impact on the main ion plasma flow, as described above.

In addition to the impurity seeding scans, a coarse scan of the input power, plasma density and magnetic field strength is performed. The observations in these simulations can mostly be attributed to the same physical processes as described above, and therefore, confirm the analysis. In summary, power exhaust remains a difficult challenge for future fusion devices. However, the impact of impurities on the plasma can be influenced considerably by the choice of the impurity seeding recipe. In this regard, this work contributes to an improving physical understanding of the underlying processes relevant for power exhaust, which facilitates a further optimization of the impurity seeding recipe and the power exhaust scenario.

Zusammenfassung

Kernfusion bietet eine vielversprechende Alternative für eine nachhaltige, klimaneutrale und sichere Grundlastenergieversorgung der Zukunft. Eine der großen Herausforderungen für den Betrieb von zukünftigen Fusionsreaktoren ist die Leistungsabfuhr. Es wird z.B. damit gerechnet, dass in dem geplanten Demonstrationsreaktor DEMO ohne Gegenmaßnahmen Leistungsflüsse von über $100\,\mathrm{MWm^{-2}}$ auf die sogenannten Divertorplatten treffen. Diese Werte überschreiten deutlich die stationären Materialbelastungsgrenzen von $5-10\,\mathrm{MWm^{-2}}$. Auch die Temperaturen an den Divertorplatten müssen auf 5 eV begrenzt werden, um übermäßige Erosion des Oberflächenmaterials zu vermeiden. Daher werden gezielt Verunreinigungen in das Plasma injiziert, wodurch ein Teil der Leistung durch Verunreinigungsstrahlung gleichmäßig auf die gesamte Reaktorwand abgestrahlt wird, und die Temperaturen und Leistungsflüsse an den Divertorplatten deutlich sinken. Leider können diese Verunreinigungen wenn sie in das Hauptplasma gelangen auch zu einer Verschlechterung des magnetischen Einschlusses und zu einer Verdünnung des Fusionsbrennstoffes führen. Bei dem Betrieb eines zukünftigen Reaktors muss also gewährleistet werden, dass die oben genannten technologischen Vorgaben nicht überschritten werden, wobei gleichzeitig der negative Einfluss der Verunreinigungen auf das Hauptplasma und auf die Fusionsrate so gering wie möglich gehalten werden sollte. Dazu muss bekannt sein, was die am besten geeignete Menge und Zusammensetzung aus verschiedenen Verunreinigungsspezies ist. Der Einfluss verschiedener Verunreinigungsspezies auf das Plasma muss daher untersucht, und die verschiedenen Spezies miteinander verglichen werden.

In dieser Arbeit werden dazu Simulationen mit dem Plasma-Randschicht-Transportcode SOLPS 5.0 durchgeführt, basierend auf H-Mode Plasmen die in dem experimentellen ASDEX Upgrade Tokamak erzeugt wurden. In den Simulationen werden die Verunreinigungsspezies Argon und Stickstoff, sowie verschiedene Mischverhältnisse der beiden Spezies untersucht. Dabei zeigt Stickstoff eine deutlich geringere Strahlung im Hauptplasma im Vergleich zu Argon, bei gleichen Bedingungen im Divertor (d.h. bei vergleichbaren Temperaturen und Leistungsflüssen an den Divertorplatten). Gleichzeitig führt Stickstoff allerdings zu einer stärkeren Verdünnung des Plasmas. Diese Eigenschaften lassen sich durch Unterschiede in

der Strahlungseffizienz und der Dichteverteilung der Verunreinigungen erklären. Durch eine Mischung von Argon und Stickstoff und eine Anpassung des Mischverhältnisses können die beiden Effekte (Strahlung im Hauptplasma und Verdünnung) gegeneinander abgewogen werden.

Eine Untersuchung des Verunreinigungstransportes ergibt, dass die Verunreinigungen einen starken Einfluss auf den Hauptionenfluss haben. Verantwortlich hierfür ist der Einfluss der Verunreinigungen auf die Ionisationsquellen der Hauptionen im Divertor. Die Beobachtungen zeigen, dass der Einfluss der Argon Verunreinigungen stärker ist als der von Stickstoff, was sich auf die Unterschiede in der Strahlungseffizienz zurückführen lässt. Aufgrund der Reibungskraft zwischen Hauptionen und Verunreinigungen resultiert aus dem veränderten Hauptionentransport auch ein starker Einfluss auf den Verunreinigungstransport. Zusätzlich verstärkt wird die Veränderung des Verunreinigungstransportes durch thermische Kräfte die in der Randschicht auf die Verunreinigungen wirken.

Des Weiteren wird untersucht wie gut die Verunreinigungen im Divertor zurückgehalten werden. Dieses "Divertor-Rückhaltevermögen" wird durch die Position der Neutralteilchenionisation und des Stagnationspunktes des Verunreinigungsflusses bestimmt. In einem vereinfachten Modell wird der Einfluss verschiedener Parameter auf das Divertor-Rückhaltevermögen untersucht, mit dem Ergebnis, dass das Rückhaltevermögen bei sinkenden Temperaturen abnimmt. Bei der maximal erlaubten Temperatur von 5 eV an den Divertorplatten ist daher bereits mit einem reduzierten Divertor-Rückhaltevermögen zu rechnen, was die Leistungsabfuhr zusätzlich erschwert.

Mit dem veränderten Plasmatransport und dem reduzierten Divertor-Rückhaltevermögen im äußeren Divertor lässt sich eine Umverteilung der Argon Verunreinigungen erklären, die bei hohen Verunreinigungskonzentrationen zu beobachten ist. In dieser Argon Umverteilung werden die Argon Verunreinigungen vom äußeren zum inneren Divertor verlagert, sobald eine gewisse Verunreinigungsmenge überschritten wird. Diese Umverteilung ist für Stickstoff deutlich schwächer ausgeprägt, was sich durch ein generell geringeres Divertor-Rückhaltevermögen für Stickstoff, und wie oben beschrieben durch den schwächeren Einfluss auf den Hauptionenfluss, und damit wieder durch die Unterschiede in der Strahlungseffizienz erklären lässt.

Beobachtungen in zusätzlichen Simulationen mit erhöhter Heizleistung, erhöhter Plasmadichte und verändertem magnetischem Feld lassen sich auf die gleichen physikalischen Prozesse zurückführen wie in den oben genannten Fällen, und bestätigen damit die oben genannten Beobachtungen. Zusammenfassend lässt sich sagen, dass die Leistungsabfuhr in zukünftigen Fusionsreaktoren eine Herausforderung

bleibt. Allerdings lässt sich das Verhalten der Verunreinigungen und deren Einfluss auf das Hauptplasma durch eine geschickte Wahl der Verunreinigungsspezies beeinflussen. Durch das neu gewonnene, vertiefte physikalische Verständnis der zugrundeliegenden Prozesse trägt diese Arbeit dazu bei, dass die Leistungsabfuhr weiter optimiert werden kann.

Contents

Chapter 1

Introduction

In view of the climate crisis and the growing global demand for energy [1, 2], a reformation of the energy sector, which is currently largely based on fossil fuels, is inevitable. This is mostly facilitated by renewable energy sources like wind and solar energy, which have many advantages, but also face technological challenges and are prone to geographic variations as well as to seasonal and daily fluctuations due to their dependence on the local weather and climate conditions [3–5]. These limitations can be attenuated, e.g., by the development and construction of an elaborate power grid and efficient large scale energy storage [6–10]. However, the availability of an additional location-independent base-load power supply would be of great value, allowing more flexibility and stability in the energy sector. Therefore, nuclear fusion – which fulfills these requirements – is a promising candidate for a climate-neutral energy source of the future.

Fusion research is inspired by the processes which power our sun, i.e., predominantly the nuclear fusion of light hydrogen nuclei (protons) into a heavier helium nucleus. The research has a long-standing history – for more than 50 years scientists had the vision to harness fusion power for electricity production [11]. However, the realization of this idea proves to be a challenging task. A hot plasma with temperatures of 150 million °C (ten times hotter than the core of the sun) has to be safely confined [12]. As the hot plasma is an ionized gas, consisting of charged particles, it is possible to hold it in levitation in a magnetic cage in order to avoid direct contact of the hot plasma with the surrounding material surfaces. However, as magnetic forces are weak, only a small plasma pressure can be sustained. Even in large future fusion reactors the pressure will not reach values much higher than the atmospheric pressure, which is about eleven orders of magnitude lower than the pressure in the sun, therefore, limiting the achievable fusion rate [12].

Under these conditions, only negligibly low fusion rates can be achieved with the solar proton-proton reaction. Therefore, a different fusion reaction with a higher reaction rate is exploited: the deuterium-tritium (D-T) reaction. Instead of normal light hydrogen nuclei (i.e., protons), in this reaction the hydrogen isotopes deuterium

(also "heavy hydrogen") and tritium ("super heavy hydrogen") are combined. In this process a helium nucleus, a neutron, and 17.6 MeV of energy are released – about four million times more energy than in a typical chemical combustion process [13]. To put this into perspective, one gram of D-T fuel – which can be processed from sea water and lithium and will be sufficiently abundant for millions of years to come – produces as much energy as eight tons of oil or eleven tons of coal [13].

Apart from the high energy gain, another benefit of nuclear fusion are the uncritical reaction products, as no climate-wrecking gases like CO_2 and also no radioactive waste are produced. Only the longtime neutron exposure of the reactor vessel components results in radioactively activated materials. These materials usually have a half-life in the order of one to five years, compared to 100 to 10.000 years in the case of radioactive waste from conventional fission [14].

The currently most advanced concept of magnetic confinement fusion is the so-called tokamak, for which one of the key challenges which has to be solved on the path to harnessing fusion energy is the power exhaust. In future fusion devices, in an unmitigated scenario, power loads at the plasma facing components in the order of $100\,\mathrm{MWm^{-2}}$ are expected. As a comparison, the heat flux at the surface of the sun is in the order of $60\,\mathrm{MWm^{-2}}$, which demonstrates the severity of the problem. A significant reduction of the heat loads can be achieved by an intentional injection of impurities into the plasma, also denoted as impurity seeding, which results in radiative power dissipation.

In this work, power exhaust and impurity seeding studies are conducted, which are motivated by experimental investigations of impurity seeded plasmas in the ASDEX Upgrade research tokamak. The experiments show, that the impact of the impurities on the plasma differs for different impurity species. Consequently, it is speculated if synergetic effects or an enhanced control on the radiation distribution can be achieved when mixing different impurity species. The expectation that the impact of the impurities on the plasma can be affected by an adjustment of the impurity species mixture is corroborated by dedicated experiments with mixed impurity seeding. Accordingly, a detailed analysis of the processes that determine the behavior of impurities in the plasma is required, in order to facilitate an optimization of the impurity seeding schemes anticipated for future fusion devices. In this context, the key questions which are addressed in this thesis are the following:

- How do different impurity species affect the plasma conditions and how is their radiation distributed within the plasma?
- Are there synergetic effects, when different impurity species are injected simul-

taneously, and is there an ideal impurity seeding mixture, or an "optimum" seeding recipe?

- How does the impurity transport differ for different impurity species, and how is the transport affected by the impurity seeding?
- How much do the impurities penetrate into the confined plasma region or how well can they be retained in the plasma edge?

To answer these questions, systematic experimental investigations, as well as numerical studies are conducted in this work, whereas the focus lies on the numerical simulations. The scope of this thesis is structured in the following way. First, the basic principles of nuclear fusion, the tokamak, power exhaust and impurity seeding are introduced in chapter 2. The experimental background of the ASDEX Upgrade fusion experiment is presented in chapter 3, where also a systematic analysis of the dedicated experimental discharges with mixed impurity seeding is provided. As the focus of this thesis is on numerical studies, the basic working principles of fluid plasma codes are introduced in chapter 4, focusing in particular on the SOLPS 5.0 code package used in this work. The modeling setup of the simulations and the results of the numerical analysis are discussed in chapter 5 and 6, and finally a summary and conclusions are given in chapter 7.

Chapter 2

Nuclear Fusion and Power Exhaust

This chapter introduces the basic concept of nuclear fusion with its potential to satisfy the need for a stable base-load power supply of the future. The tokamak fusion reactor is introduced and some of the major challenges on the path to a nuclear fusion power plant are discussed, with a focus on power exhaust.

2.1 Nuclear Fusion

Nuclear fusion is the process which powers stars like our sun. In this process two (or more) atomic nuclei are combined into a heavier nucleus. According to the binding energy per nucleon, such a reaction can be exothermic if the atomic number of the particles is lower than that of iron, i.e. $Z < 26$. From the processes that come into consideration for energy production, the highest reaction rate is achieved with the D-T fusion. In this reaction – which is foreseen to be used in nuclear fusion power plants – the atomic nuclei of the hydrogen isotopes deuterium (D) and tritium (T) are combined into a helium nucleus:

$$ {}^{2}_{1}\mathrm{D} \;+\; {}^{3}_{1}\mathrm{T} \;\rightarrow\; {}^{5}_{2}\mathrm{He}^{*} \;\rightarrow\; {}^{4}_{2}\mathrm{He}\,(3.5\,\mathrm{MeV}) \;+\; {}^{1}_{0}\mathrm{n}\,(14.1\,\mathrm{MeV}). \tag{2.1} $$

In this process 17.6 MeV of energy are released in every fusion reaction, where 80 % of this energy (according to the mass ratio of the reaction products) is carried by the neutron.

To facilitate nuclear fusion, high temperatures (i.e., high kinetic energies) are required in order to enable the positively charged nuclei to overcome the Coulomb barrier. For the D-T fusion the maximum reaction rate is achieved at a temperature around 64 keV [15], which corresponds to roughly 700 million °C[1]. For comparison, the temperature in the core of the sun is around 15.7 million °C. Fortunately, due to the high-energy tail of the Maxwell distribution, also temperatures of 10 – 20 keV are

[1] In plasma physics the temperature is often given in eV, where $T\,[\mathrm{K}] \mathrel{\widehat{=}} \frac{e}{k_\mathrm{B}} T\,[\mathrm{eV}] \approx 1.2 \cdot 10^4\, T\,[\mathrm{eV}]$, with the elementary charge e and the Boltzmann constant k_B.

sufficient to sustain fusion processes in a future reactor. At these high temperatures, the D-T fuel is ionized, resulting in a hot ionized gas: the plasma.

2.1.1 Inertial and Magnetic Plasma Confinement

In order to facilitate net energy production, the power P_{fusion} generated via fusion processes must be larger than the external heating power P_{in}. The ratio of P_{fusion} and P_{in} is usually denoted as Q-factor: $Q = P_{\text{fusion}}/P_{\text{in}}$. Consequently, for net energy production $Q > 1$ is required. The ultimate goal, however, is to reach ignition, i.e., a self sustained "burning" plasma. In this case the fusion power is so high, that the external heating can be completely replaced by the alpha heating, i.e., by the heat deposited in the plasma by the helium nuclei produced in the fusion reactions. In this case $P_{\text{in}} = 0$ and $Q = \infty$.

To reach $Q > 1$, the plasma must be confined and kept at high temperatures for a sufficiently long period of time. Therefore, one aims for a high energy confinement time τ_E, which is defined as the ratio of the stored energy in the plasma to the power loss rate. From power balance considerations, the Lawson criterion [16] can be deduced, which defines the requirements to achieve ignition. The Lawson criterion sets a lower limit for the so-called triple product $nT\tau_E$ which contains the plasma density n, the temperature T and the energy confinement time τ_E:

$$nT\tau_E > 3 \cdot 10^{24}\,\text{eVsm}^{-3}. \tag{2.2}$$

In order to reach $Q > 1$ and to fulfill the Lawson criterion, different approaches are under consideration.

In inertial confinement small pellets of frozen D-T fuel are homogeneously heated by short and strong laser pulses or ion beams [17, 18]. The sudden heating of about 1 MJ within 20 ns [19] causes an ablation of the outer shells of the D-T pellet. Consequently, the inner shells are strongly compressed and the fuel is inertially confined. Despite a low confinement time τ_E, the high densities and temperatures facilitate fusion reactions. However, due to instabilities (e.g., Rayleigh-Taylor instabilities [20]) and with the requirement of very isotropical and homogeneous heating, this method faces several technological difficulties. Additionally, to provide a steady power generation, this process has to be repeated with a high frequency (in the order of 3 Hz), which is technologically challenging, given the required precision of the pellet positioning. As inertial confinement is not considered in this work, it is not discussed here any further.

In order to harness fusion power for electricity production, the currently most studied and so far also the most advanced approach is magnetic confinement fusion.

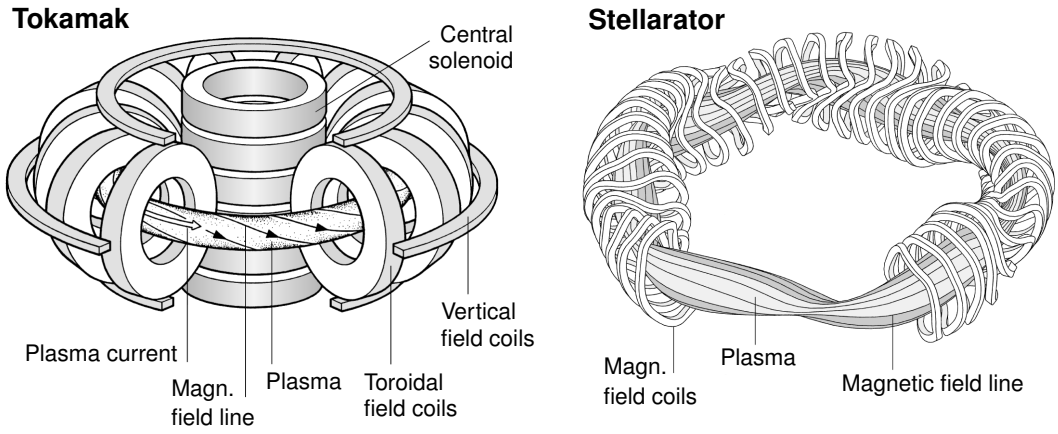

Figure 2.1: Schematic drawings of the tokamak and the stellarator showing the magnetic field coils and the resulting plasma shapes. Figures from [21].

In magnetic confinement fusion, the plasma is held in its place by strong magnetic fields. This is possible due to the Lorentz force, which causes a gyration of the ionized particles around the magnetic field lines, and thereby, restricts the particle motion such, that on average only motion parallel to the magnetic field is possible. In this sense, in the following, "parallel" and "perpendicular" always refers to the corresponding direction with respect to the magnetic field. Early attempts to magnetically confine plasmas have been made in cylindrical linear devices. However, as in such a device the plasma is always in direct contact with the edges of the cylinder, and due to instabilities, good confinement could not be achieved. Therefore, a new design was developed in which the linear device was bent into a ring-shaped torus, creating magnetic field lines that close on themselves without any intersection with a material surface. In this configuration the particle traces circle around the center in closed loops, keeping them confined in the magnetic cage. The resulting machine is the so-called tokamak.

2.1.2 The Tokamak

A schematic drawing of the tokamak (which is a Russian acronym for "toroidal chamber with magnetic coils") is shown in figure 2.1 (left). A strong toroidal magnetic field is generated by the toroidal field coils which surround the plasma volume. However, with a purely toroidal magnetic field, confinement cannot be achieved; due to fluid drifts a charge separation between the upper and lower side of the torus causes electric fields, which in turn cause a fluid drift in radial direction.

Therefore, to achieve confinement, the magnetic field lines are twisted into a helical shape, as it can also be seen in figure 2.1. This results in so-called Pfirsch-Schlüter currents, which connect the upper and lower side of the torus and compensate the charge separation. For this purpose, a plasma current is required within the plasma in toroidal direction, creating the poloidal magnetic field component, which together with the toroidal field yields helical field lines. The plasma current is induced in the charged plasma via the central solenoid acting as a primary transformer coil. This central solenoid, which requires a steadily varying current, determines the pulsed operation of a tokamak. The additional vertical field coils in figure 2.1 are required for the stabilization and shaping of the plasma.

With the toroidal and poloidal components B_t and B_p of the total magnetic field $B = \sqrt{B_\mathrm{t}^2 + B_\mathrm{p}^2}$ in the tokamak, the so-called safety factor q is defined as $q = \frac{rB_\mathrm{t}}{RB_\mathrm{p}}$, where r is the minor radius or radial coordinate and R is the major radius at the magnetic axis of the machine. The safety factor describes the number of toroidal turns necessary for one poloidal turn along a magnetic field line.

For comparison, figure 2.1 (right) shows the schematic drawing of a so-called stellarator. In such a device the helical winding of the field lines is realized by the complex 3D shape of the magnetic field coils. Therefore, a central solenoid is not required, allowing steady state operation. The construction of the sophisticated magnetic field coils of a stellarator is a challenging engineering task which requires high precision. Nevertheless, significant progress in stellarator research has been made in the recent years [22]. However, as this work is based on the tokamak with its simpler design and further advanced development, the stellarator is not considered here any further.

2.1.3 Magnetic Field Configurations

For a plasma in magnetohydrodynamic (MHD) equilibrium [23] the $\boldsymbol{j}\times\boldsymbol{B}$-force has to be balanced by the plasma pressure force, $\boldsymbol{j} \times \boldsymbol{B} = \boldsymbol{\nabla} p$, where $\boldsymbol{j}$ is the current, $\boldsymbol{B}$ is the magnetic field, and p is the pressure. As consequently $\boldsymbol{\nabla} p \cdot \boldsymbol{B} = 0$ and $\boldsymbol{\nabla} p \cdot \boldsymbol{j} = 0$, this implies that the magnetic field lines and currents lie on closed surfaces of constant pressure. These flux surfaces are indicated in figure 2.2, where the poloidal cross-sections of the two magnetic field configurations of the tokamak, i.e., the limiter configuration and the divertor configuration, are opposed. In figure 2.2, also the terminology which is commonly used to refer to certain regions and positions in the tokamak is introduced.

In the limiter configuration, the position of the last closed flux surface is determined by a limiter, a solid material surface which is in direct contact with the plasma.

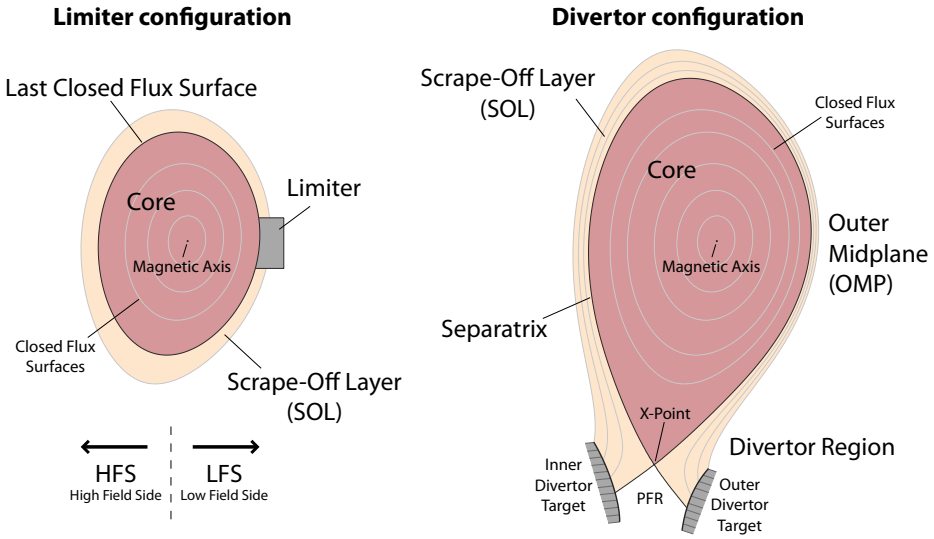

Figure 2.2: Schematic drawing of a poloidal cross-section of the plasma in the tokamak, showing the limiter and the divertor configuration. The different regions in the plasma are depicted, namely the core region, the scrape-off layer (SOL), the divertor region and the private flux region (PFR). The outer midplane position (OMP) is also referred to as "upstream", in opposition to the divertor region "downstream". Due to the $1/R$ dependence of the toroidal magnetic field, the inner side (here on the left in both configurations) is also often denoted as high field side (HFS) and the outer side as low field side (LFS).

As this limiter scrapes off the outermost plasma layers, the region directly outside of the last closed flux surface is denoted as scrape-off layer (SOL). The direct material contact results in strong plasma-wall interaction in the direct vicinity of the confined core region. In this situation, material erosion and sputtering can result in significant impurity contamination of the core plasma with wall material, and cause severe confinement degradation. Additionally, in this configuration the lifetime of the plasma facing components is limited.

Significantly improved properties compared to the limiter configuration are obtained in the divertor configuration. Here, additional magnetic field coils are used to create a quadrupole field, resulting in a magnetic geometry as it is displayed on the right-hand side of figure 2.2. The so-called separatrix (which marks the transition from closed flux surfaces in the confined region to open flux surfaces in the SOL) is directly generated by the magnetic field, with the formation of an X-point at which the poloidal magnetic field vanishes. As a result, the closed flux

surfaces are not in direct contact with any material surface. Still, due to plasma diffusion and turbulence, particles and energy are transported in radial direction and across the separatrix into the SOL. As the radial (or perpendicular) transport is small compared to the parallel transport, the particles and power within the SOL are quickly transported in parallel direction towards the divertor targets. However, as these divertor targets are at remote locations, distant from the confined region, this significantly reduces the risk of core contamination with eroded target material and at the same time allows better control of the power exhaust. Furthermore, in the remote divertor region it is possible to sustain high neutral densities. This is important to control the particle exhaust, i.e., the pumping of impurities and (in future devices) the helium particles which are produced in the fusion reactions (also denoted as "helium ash") and which result in an undesired dilution of the D-T fuel.

While figure 2.2 (right) shows a lower single null configuration, with the X-point and the divertor at the bottom, also upper single null configurations are possible with the X-point and the divertor on top of the machine. Furthermore, in double null configuration two X-points are created within the plasma vessel and the SOL is connected to both the upper and lower divertor. There are also attempts to exploit alternative divertor configurations, which aim for an enhancement of the flux expansion (see section 2.2.2), or split up the power flux onto several additional divertor targets via a more elaborate choice of the magnetic field configurations (see, e.g., the X-divertor [24], the super X-divertor [25], or the snowflake divertor [26, 27]). Such alternative divertor configurations are an active area of research which is not considered in this work.

With the definition of the magnetic axis and the separatrix, the coordinate ρ_{pol} which is often used to describe the position of a certain flux surface in the plasma can be defined:

$$\rho_{\mathrm{pol}} = \sqrt{\frac{\Psi - \Psi_{\mathrm{axis}}}{\Psi_{\mathrm{sep}} - \Psi_{\mathrm{axis}}}}, \tag{2.3}$$

where Ψ is the poloidal magnetic flux. With the subscripts "axis" and "sep", Ψ denotes the magnetic flux at the magnetic axis and at the separatrix position, respectively. Hence, the coordinate ρ_{pol} is zero at the magnetic axis and one at the separatrix.

2.1.4 Plasma Heating

As discussed above, high temperatures in the order of several million °C are required to facilitate nuclear fusion reactions. In order to heat the D-T fuel in a fusion plasma (or the pure deuterium gas in an experimental device) to sufficiently high

temperatures, appropriate heating systems have to be provided. In present day fusion experiments, this is usually realized via a combination of different systems which exploit different physical mechanisms.

An intrinsic heating mechanism in the tokamak is the ohmic heating, which is provided by the plasma current I_p induced by the central solenoid. Due to the finite electrical resistance R_p of the plasma, a power of $P = R_p I_p^2$ is deposited. However, as the electrical resistance decreases with increasing temperature, this mechanism alone is not sufficient to reach the high temperatures required for a fusion plasma.

Electron cyclotron resonance heating (ECRH) and ion cyclotron resonance heating (ICRH) are based on electromagnetic waves, which are injected into the plasma, where they couple to the gyro motion of the electrons and ions, respectively. The energy of the electromagnetic wave is absorbed by the plasma, which results in efficient heating.

Finally, with the neutral beam injection (NBI) high energetic neutral hydrogen or deuterium particles are injected into the plasma, which can penetrate the magnetic field. The particles are ionized in the plasma, where they thermalize with the colder plasma. As the NBI uses a particle beam, this method also provides a particle source, and therefore contributes to the plasma fueling.

2.1.5 The Low- and High-Confinement Modes

In the early phase of fusion research, where only low heating power was available, the basic operation regime of tokamaks was the low-confinement mode or L-mode. In this regime significant radial transport due to turbulence limits the quality of the confinement. However, an increase of the heating power above a certain threshold value led to the discovery of the so-called high-confinement mode, or H-mode. This operation regime is characterized by confinement which is by a factor of about two higher than in L-mode [28]. The commonly accepted explanation for the occurrence of the H-mode is an $E \times B$ shear flow which significantly reduces the turbulent radial transport

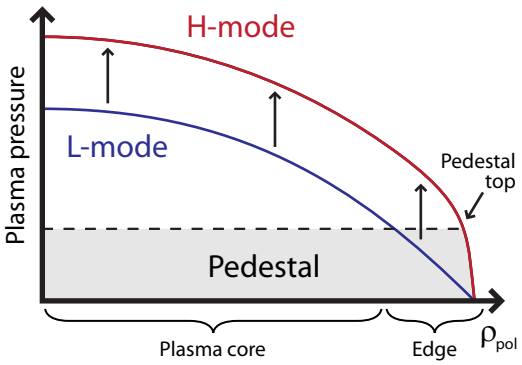

Figure 2.3: Schematic illustration of the difference between a typical radial profile (e.g., of the plasma density, temperature, or pressure) in L-mode and H-mode.

in the edge [29]. This results in an edge transport barrier with strongly increased density and temperature gradients in the edge region. Due to the experimentally observed stiffness of the gradients within the confined region, the transport barrier results in an increase of the plasma parameters in the core region. Therefore, the H-mode profiles are often described as if they are raised onto a pedestal. This is also illustrated in the schematic comparison of a typical radial pressure profile in L-mode and in H-mode shown in figure 2.3. Due to the improved confinement properties, the H-mode is the foreseen operation regime for future fusion reactors.

In practice, the quality of the confinement is often characterized by the so-called H_{98} factor. This factor describes the energy confinement time τ_E with respect to the $H_{\mathrm{IPB98(y,2)}}$ scaling [30]: $H_{98} = \tau_E / \tau_{\mathrm{IPB98(y,2)}}$. A good confinement is indicated by $H_{98} \approx 1$.

The H-mode is typically accompanied by quasi-periodic relaxations of the edge gradients, the so-called edge localized modes (ELMs). ELMs are a consequence of MHD instabilities. They can expel huge amounts of energy and particles in a short period of time, resulting in intolerably high transient heat loads onto the plasma facing components. Different types of ELMs, which differ in terms of the ELM size and the frequency are observed. In the experiment so-called type I ELMs and smaller type III ELMs are the most relevant. An overview with a detailed characterization of the different ELM types can be found in [31].

2.1.6 Next-Step Devices: ITER and DEMO

The currently existing experimental tokamak devices are not yet capable of net energy production, i.e, reaching $Q > 1$. Due to the special requirements and legal stipulations that come with the handling of the radioactive tritium isotope, most of the present day machines only investigate pure deuterium (or hydrogen or helium) plasmas with a negligible fusion rate. One noteworthy exception is the JET tokamak, which also investigates D-T plasmas and was able to reach $Q = 0.64$ [32], the highest value of Q ever reached. Still, it was not yet possible to reach break-even (i.e., $Q = 1$).

With the international tokamak ITER, which will be equipped with superconducting magnetic field coils, it is foreseen to demonstrate energy production with a Q-value of up to 10 [33]. As the maximum achievable fusion power increases with the plasma volume, and therefore, with the machine size, ITER will be considerably larger than any existing tokamak. The major radius of ITER will be 6.2 m. For comparison, JET (currently the largest tokamak in the world) has a major radius of 2.96 m. ITER is currently under construction in Cadarache, in the south of France and is scheduled to start operation in 2025.

Finally, in a next step after ITER, it is intended to demonstrate electricity generation in the demonstration reactor DEMO [34]. Currently, a DEMO-like device is foreseen to be operated with a fusion power around 3 GW [35]. As this also results in an enormous amount of energy which has to be exhausted in the SOL, this makes power exhaust a serious challenge, which requires intensive investigation. Therefore, power exhaust is discussed in more detail in the following section.

2.2 Power Exhaust and Impurity Seeding

Power exhaust is a critical issue for the operation of any future fusion device. Due to the strong parallel transport compared to the perpendicular transport (with roughly two orders of magnitude difference) the power in the SOL is directed onto a relatively small plasma wetted area on the divertor targets (in the order of a few m^2, depending on the machine and the divertor geometry). For an ITER-like device, a power flux across the separatrix of $P_{SOL} = 100\,MW$ entering the SOL is expected [36]. In an unmitigated scenario this results in a target heat load in the order of $50\,MWm^{-2}$, while for a DEMO-like device this value increases to several $100\,MWm^{-2}$ [37] (assuming a radial power fall-off length at the outer midplane around $\lambda_q \approx 1\,mm$, see section 2.2.2). This considerably exceeds the foreseen stationary technological material limits at the divertor target plates, which are in the order of $5-10\,MWm^{-2}$ [38–43].

Additionally, the plasma temperature in front of the target plates[2] has to be limited to avoid excessive erosion of the target material. In a purely hydrogenic plasma, only moderate erosion is expected. However, the situation becomes more critical if ions with higher charge states are accessible, i.e., with impurities (either intrinsic, e.g., due to plasma-wall interaction, or extrinsic due to intentional impurity seeding, see section 2.2.3). Depending on the impurity content in the plasma and the impurity mix, it was shown in [41] that the target temperatures must be kept below 5 eV to limit the erosion to an acceptable value of 5 mm within a period of two years in a DEMO-like device.

In this section an overview over the processes relevant for power exhaust will be provided (sections 2.2.1 and 2.2.2), as well as a discussion of impurity seeding (section 2.2.3), which can be applied to reduce the peak power loads and temperatures at the divertor targets, and to induce divertor detachment (section 2.2.4).

[2] In the following we will refer to the plasma temperature in front of the target plates only as "target temperature", even though it is not the temperature of the target plate itself.

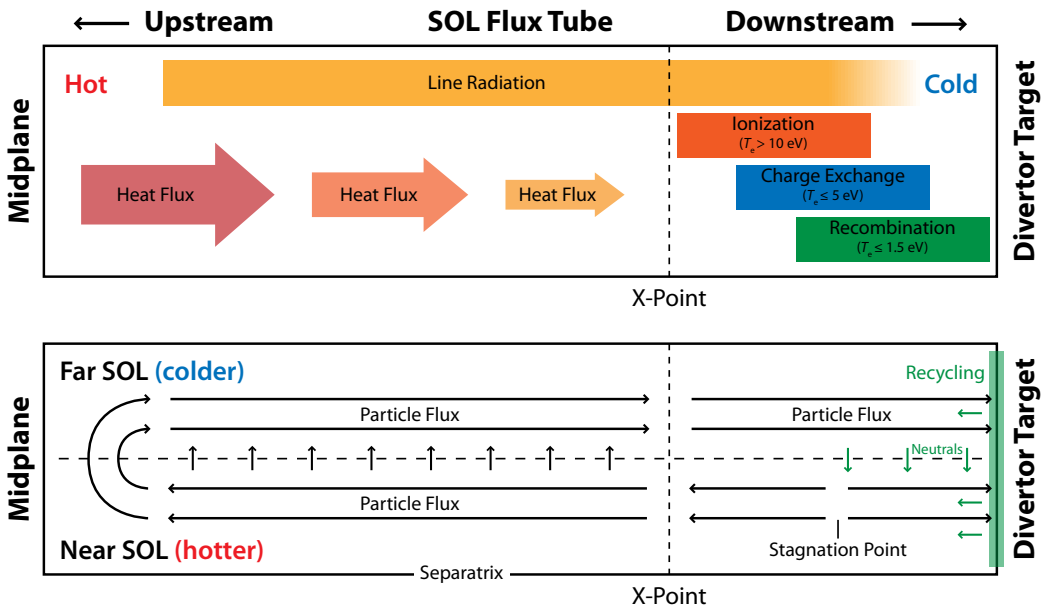

Figure 2.4: A simplified representation of the SOL, going from the midplane on the left to the divertor target on the right. The heat flux and the volumetric processes in the SOL (top), as well as the main ion particle flux patterns (bottom) are schematically illustrated.

2.2.1 Volumetric Processes and Plasma-Wall Interaction in the Scrape-Off Layer

A schematic overview over the most important volumetric processes in the SOL is provided in figure 2.4 (top). According to the varying temperature in the SOL, which is highest at the midplane position and decreases towards the divertor targets, different volumetric processes dominate in different regions. As indicated in figure 2.4, line radiation can occur within the whole SOL, depending on the composition of the plasma, i.e., on the presence of impurity species, and their specific radiation efficiencies (see section 2.2.3). Ionization is dominant in regions with temperatures above 10 eV, according to the ionization potential of the particles in the plasma. In regions closer to the divertor targets, i.e., at temperatures below 5 eV, charge exchange reactions become important, where an electron is transferred from a neutral atom to a charged ion. As a result, in charge exchange reactions, the neutralized particle can escape independently from the magnetic field lines and carry away its momentum. Therefore, charge exchange reactions can result in momentum loss. The same is true for volumetric recombination reactions, which only dominate over ionization

at low temperatures around $T_e \leq 1.5\,\mathrm{eV}$. As indicated in figure 2.4, the volumetric processes result in power dissipation, and in a reduction of the heat flux along the flux tube. The role of the volumetric processes for divertor detachment is discussed in more detail in section 2.2.4.

Apart from volumetric processes, another important issue in the SOL is the plasma-wall interaction. On scales which are larger than the Debye length $\lambda_D = \sqrt{\epsilon_0 T / e^2 n_e}$, the plasma is quasi-neutral. However, when the plasma is in direct contact with a material surface, on a short scale electrons accumulate at the surface, due to their higher mobility compared to ions. As a result, a strong potential drop evolves in a thin boundary layer in front of the material surface. This layer has an extension in the order of the Debye length and is denoted as the Debye sheath or simply as sheath. Due to the electric potential, ions are accelerated towards the material surface, and according to the Bohm-Chodura sheath boundary condition [44] they reach sound speed $u_{ion} \geq c_s$ at the sheath entrance. In sum one obtains an ambipolar particle flux onto the material surface.

At the surface, the ions recombine with the electrons and the resulting neutrals either escape, or re-enter the plasma where they are re-ionized. This process is denoted as recycling. In figure 2.4 (bottom), the situation is schematically illustrated for the so-called high-recycling regime, in which high particle fluxes onto the divertor targets result in strong recycling in the SOL. According to the temperatures in the SOL some of the neutrals originating from recycling in the (colder) far SOL are able to reach the (hotter) near SOL, i.e., they get closer to the separatrix. This results in a particle sink in the far SOL and in an "over-ionization", i.e., in a strong ion source in the near SOL [45]. As the parallel particle flows are mainly determined by sources and sinks, this results in a particle flux pattern as it is shown in figure 2.4 (bottom), with a stagnation point in the near SOL between divertor and X-point and a flow reversal at the midplane, due to the diffusive radial transport.

2.2.2 The Power Decay Length

With the diffusive nature of the perpendicular transport of energy and particles in the SOL, one obtains an exponential decay of the radial upstream profiles of the plasma parameters (like density, temperature, pressure) and also of the parallel heat flux density $q_\parallel$:

$$q_\parallel(s) = q_{\parallel,\mathrm{sep}} \cdot \exp\left(-\frac{s}{\lambda_{q_\parallel}}\right). \tag{2.4}$$

Here, s is the radial distance from the separatrix at the outer midplane position, and $q_{\parallel,\mathrm{sep}}$ is the heat flux value at the separatrix position. The power decay length $\lambda_{q_\parallel}$ is

an important parameter for power exhaust, as it can be used to estimate the peak heat loads onto the divertor targets in future fusion devices. In a simplified picture, all the power in the SOL (P_{SOL}) enters the SOL at the outer midplane position and is transported towards the divertor region along the field lines trough a channel with a characteristic width of $\lambda_{q_\parallel}$ and a cross-sectional area of $A_\parallel = 2\pi R \lambda_{q_\parallel} \frac{B_\mathrm{p}}{B}$ (with the field line inclination $\frac{B_\mathrm{p}}{B}$). In this case, the maximum parallel power flux in the SOL is determined as

$$q_{\parallel,\mathrm{sep}} = \frac{P_{\mathrm{SOL}}}{A_\parallel} = \frac{P_{\mathrm{SOL}} B}{2\pi R \lambda_{q_\parallel} B_\mathrm{p}}. \tag{2.5}$$

At the divertor targets it has to be taken into account, that $\lambda_{q,\,\mathrm{trgt}}$ differs from the upstream value, due to the magnetic flux expansion and the divertor broadening. The flux expansion describes how the flux surfaces widen as the poloidal magnetic field strength decreases along the field line. The effect is strongest in the vicinity of the X-point (cf. figure 2.2), but also at the divertor targets the flux tubes are expanded (i.e., the width of the flux tube at the target location δs_{trgt} is larger than its width at the outer midplane δs_{OMP}). The flux expansion is determined by the ratio of the poloidal and toroidal magnetic field strength upstream and at the target:

$$f_x^* = \frac{\delta s_{\mathrm{trgt}}}{\delta s_{\mathrm{OMP}}} \approx \frac{B_\mathrm{p}^{\mathrm{OMP}}}{B_\mathrm{t}^{\mathrm{OMP}}} \frac{B_\mathrm{t}^{\mathrm{trgt}}}{B_\mathrm{p}^{\mathrm{trgt}}}. \tag{2.6}$$

To obtain the effective flux expansion $f_x = \frac{f_x^*}{\sin\alpha}$, additionally also the poloidal inclination angle of the divertor target α can be taken into account. The extent of the flux expansion depends on the machine and on the divertor geometry, but it usually has a value around 5. With a tilting angle of the divertor targets of $\alpha \gtrsim 3^\circ$ (the minimum is set by engineering limits regarding the precise alignment of the target structure), an effective flux expansion around 100 can be achieved.

Additionally, in the divertor region (i.e., below the X-point) the parallel heat flux can diffuse into the private flux region. The resulting heat flux profile shape at the divertor targets can be described by a convolution of an exponentially decaying heat flux, similar to equation (2.4), and a Gaussian, caused by the diffusion, which is characterized by the divertor broadening or divertor spreading factor S. The divertor broadening results in an additional reduction of the peak power loads at the divertor targets. Nevertheless, the power loads onto the divertor targets are still a critical issue for future fusion devices.

2.2.3 Impurity Seeding for Radiative Plasma Cooling

A reduction of the target heat loads and divertor plasma temperatures can be achieved by a controlled injection of selected impurity species, so-called impurity seeding. This leads to radiative power dissipation by the injected impurities, and to a more uniform distribution of the power onto the vessel walls, instead of a very focused impact on the small plasma wetted area on the divertor targets. However, immoderate impurity seeding can result in an intolerable core contamination and fuel dilution, and consequently in a reduced fusion rate and severe confinement degradation, or even in a disruption (i.e., a sudden loss of confinement) [47]. The radiative behavior, the impurity transport, and thus also the impurity density distributions can vary considerably for different impurity species [48]. Therefore, in order to guarantee no detrimental impact on the confined plasma, but at the same time prevent severe damage of the plasma facing components, it is important to identify an "optimum" seeding recipe for the safe operation of future fusion devices.

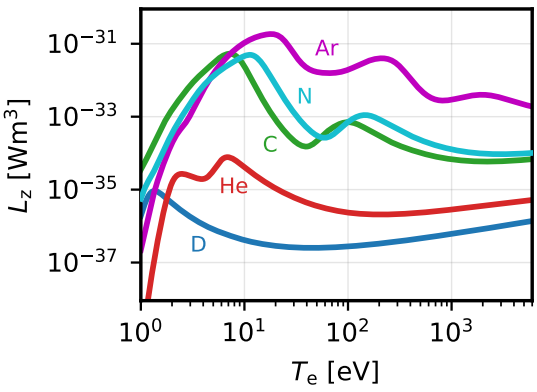

Figure 2.5: Radiation efficiency of different atomic species in coronal equilibrium at $n_e = 10^{19}\,m^{-3}$ according to the ADAS database [46].

The power $P_{rad,z}$ radiated by an impurity can be expressed as the product of the impurity density n_z, the radiation efficiency L_z, and the electron density n_e:

$$P_{rad,z} = n_z \cdot L_z \cdot n_e. \tag{2.7}$$

In coronal equilibrium the radiation efficiency L_z can be derived from atomic databases as it is shown in Fig. 2.5 in dependence of the electron temperature T_e for different atomic species [46, 48]. The radiation efficiency varies considerably between atomic species and has a strong temperature dependence. The dependence on the electron density is negligible and not depicted here. If we focus on argon and nitrogen – which are the impurity species studied within this work – it can be seen that at high temperatures, i.e., especially in the core region, argon is characterized by a much higher radiation efficiency compared to nitrogen. On the other hand, nitrogen is a typical divertor radiator, as its radiation efficiency exceeds that of argon at temperatures below 5 eV.

In practice, in a dynamic system impurity transport results in a deviation from the coronal equilibrium and to enhanced radiation efficiencies [41]. This so-called non-coronal enhancement of the radiation efficiency is quantified by the non-equilibrium parameter $n_e\tau$ (described in [49]). The value τ can be interpreted as the characteristic residence time of an impurity within a region characterized by certain plasma conditions. The radiation efficiency approaches the coronal values for $\tau \to \infty$ (i.e., the system approaches equilibrium), while in regions with a short residence time (i.e., with strong transport), a significant non-coronal enhancement can be expected.

Figure 2.5 also reveals, that a temperature drop can be a self-amplifying process, depending on the slope of the L_z curve at the considered temperature. With a negative L_z slope decreasing temperatures result in an increase of the radiation efficiency, which leads to increased radiation and to a further temperature reduction. Here this is also the case in the hot core region, where the temperatures are above the local L_z maximum positions around 150 eV (nitrogen) and 220 eV (argon).

A related mechanism is the radiation condensation, which results in so-called Marfes [50]. Instead of the temperature dependence of L_z, the radiation condensation is attributed to the dependence of $P_{rad,z}$ on the plasma density n_e. With equation (2.7) and a constant pressure $p_e = n_e T_e$ on a closed flux surface, the impurity radiation can be expressed as

$$P_{rad,z} = n_z \cdot L_z \cdot \frac{p_e}{T_e}. \tag{2.8}$$

This leads to the conclusion, that the radiation can increase even further with decreasing temperature T_e.

As it was stated above, it will be crucial not to harm the confined plasma and the burn conditions. On the other hand, sufficient power dissipation in the divertor region is required. Hence, in an ideal case, the impurities should be well retained in the divertor region and not be able to reach the confined plasma, i.e., one aims for something which is denoted as a good divertor impurity retention. A detailed review on previous publications on the impurity transport in the divertor and the divertor impurity retention can be found, e.g., in [51]. Most of the previous publications mainly focus on the role of the forces acting on the impurity ions in the plasma [45, 52–54], where the most important force acting on the impurities is the friction force

$$F_{fr} \propto (u_{D^+} - u_{imp}), \tag{2.9}$$

which is determined by the discrepancy between the main ion plasma flow u_{D^+} and the impurity ion flow u_{imp}. If no other forces were present, F_{fr} would equilibrate the velocities of impurities and main ions, until as a result F_{fr} vanishes. Therefore, the

main ion plasma flow determines the baseline of the impurity ion flow. A deviation of the impurity flow from this baseline is mainly due to the thermal force

$$F_{\text{th}} \propto \nabla T \tag{2.10}$$

caused by temperature gradients ∇T. Due to the parallel temperature profile in the SOL, which is peaked around the outer midplane position, F_{th} drags particles away from the targets towards the outer midplane. Additional pressure gradient forces and electrostatic forces are small in the main chamber SOL, and even though they become stronger closer to the targets, they do not turn out to be relevant for the impurity transport and the divertor retention. Consequently, the approximate steady state force balance can be written as $F_{\text{th}} \approx -F_{\text{fr}}$.

The forces acting on the impurities determine the impurity ion flows, and therefore also the impurity stagnation point position, which is shifted away from the main ion stagnation point (cf. figure 2.4, bottom) towards the target, due to the thermal force. However, crucial for the explanation of the divertor impurity retention are the relative positions of the impurity stagnation point and the ionization front position of neutral impurities [55]. As for the main ions, the impurity ion flux onto the divertor target is recycled, which results in a strong particle source of neutral impurities at the target plate. The recycled neutrals are able to move upstream towards the stagnation point only as long as they are not ionized, since as ions they would adapt to the plasma flow and stream back towards the target plate. Only if the ionization of the impurities occurs beyond the impurity stagnation point, the ionized particles are able to stream out of the divertor region, according to the particle flux pattern (cf. figure 2.4, bottom). A longer ionization mean free path of the impurity neutrals results in increased divertor leakage.

A measure to assess the quality of the divertor retention is the impurity compression, defined as the ratio of the impurity densities in the divertor region and in the core region: $C = n_{\text{imp,div}}/n_{\text{imp,core}}$. Similarly, the divertor enrichment can be defined as the ratio of the impurity concentrations: $E = c_{\text{imp,div}}/c_{\text{imp,core}}$. The higher the impurity compression or impurity enrichment values are, the better are the impurities retained in the divertor region.

2.2.4 Divertor Detachment

With sufficient impurity seeding or at high plasma densities, i.e., with strong deuterium fueling, it is observed that the divertor enters a regime which is denoted as the detachment state. Detachment is characterized by a pressure loss along the flux tube between midplane and target, significantly reduced power and particle fluxes

to the divertor targets and low target temperatures ($T_e \lesssim 5-10\,\mathrm{eV}$ [56]). The classification of the different detachment stages in the literature is not always consistent, however, in this work complete or full detachment, pronounced detachment and partial detachment are distinguished, as discussed in the following. If the divertor is not in a detachment state, it is denoted as attached, which typically indicates high power loads and temperatures at the divertor targets.

In the high-recycling regime (cf. section 2.2.1), the divertor targets are still attached. However, it can be interpreted as a pre-stage of (partial) detachment. Apart from the ionization, no significant volumetric processes have to be considered. Nevertheless, strong parallel temperature gradients in the SOL are observed and (especially with impurity seeding) low target temperatures in the order of $5-10\,\mathrm{eV}$ can be achieved. This is sometimes also referred to as "power detachment" [57].

In present day machines, the high recycling regime is already sufficient to fulfill the power exhaust requirements and protect the plasma facing components. With relatively low particle fluxes in the existing machines, the potential energy which is released when the deuterium ions recombine to neutral molecules at the divertor targets ($E_{pot} \approx 15.8\,\mathrm{eV}$ per deuterium ion) can be neglected [37]. However, in future fusion devices like ITER or DEMO high particle fluxes to the divertor targets are expected [37]. In this case the potential energy flux to the targets becomes a significant contribution and also a reduction of the particle flux (i.e., "particle detachment") is required [57].

If the electron temperature is reduced to values below roughly $5\,\mathrm{eV}$ via strong radiation cooling or high plasma densities, the divertor targets can start to detach (denoted as partial detachment). In this regime volumetric processes like charge exchange and recombination, which can remove energy, momentum and particles from a flux tube, begin to play a crucial role. As a result, parallel pressure loss along the flux tube is observed in the region close to the strike point. On the other hand, in the far SOL (i.e., further away from the separatrix) the target stays attached, facilitating good neutral divertor compression with high neutral densities and good control on the power and particle exhaust (e.g., pumping of impurities and helium ash).

Below temperatures of $1.5\,\mathrm{eV}$ strong volumetric processes set in and recombination dominates over ionization. In this case, a significant parallel pressure loss is observed and the plasma completely detaches from the divertor target, which means that both power and particle flux are reduced significantly. While in pronounced detachment still a small particle flux in the far SOL is sustained, complete detachment is characterized by almost completely flat target profiles of the ion saturation current $j_{sat} \propto n\sqrt{T}$ and the electron temperature T_e along a large fraction

of the target [37]. The heat and particle fluxes are reduced by at least one order of magnitude compared to attached cases with similar upstream conditions.

It is commonly observed, that there is an asymmetry between the particle fluxes and power loads towards the inner and the outer divertor, typically with higher fluxes and temperatures at the outer divertor target. This often results in a situation where the inner divertor is already detached, while the outer divertor is still attached or in the high recycling regime. This asymmetry is not yet fully understood, but can at least partly be explained by geometrical effects and plasma drifts, which are a result of forces acting on the charged particles in the magnetic field, and are able to move plasma both in radial and in poloidal direction in the tokamak (cf. section 4.2.4). Furthermore, the detachment is not always necessarily a steady state condition, as also fluctuating detachment states are observed, in which the divertor oscillates between two detachment states [58].

The investigation of power exhaust and impurity seeding is the focus of this thesis. Impurity seeding studies with argon and nitrogen seeding are conducted in the following, both in the experiment (chapter 3), as well as with numerical simulations (chapters 4 – 6).

Chapter 3

Experimental Investigations and the ASDEX Upgrade Tokamak

Experimental studies are crucial for the preparation of a future fusion reactor. In this chapter, first a brief overview over the current status of experimental studies concerning power exhaust and impurity seeding is provided. Then the ASDEX Upgrade tokamak and the main plasma diagnostics are introduced, and finally, a basic analysis of a set of dedicated ASDEX Upgrade discharges for the investigation of mixed impurity seeding with nitrogen and argon is presented.

3.1 Current Status of Power Exhaust and Impurity Seeding Studies

As discussed in section 2.2, power exhaust and impurity seeding studies are of great relevance for the development of future fusion devices. Therefore, power exhaust is an active field of research and several experiments are dedicated to the investigation of the impact of impurities on the divertor operation and plasma performance [37, 41, 59–74]. Some of the experimental devices and the current status of research are discussed in the following.

3.1.1 Experimental Devices

One of the most important experimental devices for tokamak research is the Joint European Torus, short JET [75]. With a large radius of 2.96 m and a plasma volume of 100 m^3 it is currently the largest operating research tokamak. JET is located at the Culham Centre for Fusion Energy in the UK. Between 2009 and 2011 all carbon components in the JET vacuum vessel were replaced by tungsten and beryllium to allow studies with an "ITER-like" full metal wall [76]. JET is currently the only machine in which apart from pure deuterium plasmas also deuterium-tritium operation can be studied.

The Alcator C-Mod tokamak [77, 78] with a major radius of 0.67 m and a plasma volume of 1 m^3 was operated until 2016 at the Massachusetts Institute of Technology (MIT) in the United States. It was able to operate at a relatively high magnetic field of up to 8 T. Alcator C-Mod was the first major divertor tokamak with exclusively metal high-Z (molybdenum) plasma facing components [79].

A selection of further tokamaks relevant for power exhaust includes, e.g., DIII-D, located in the United States and operated by General Atomics, with a major radius of 1.66 m [80]. The JT-60 [81] tokamak, a device with a major radius of 3.4 m and a plasma volume of 90 m^3 was operated until 2010 in Japan. It is currently upgraded to JT-60SA, which will be operated with superconducting coils and is foreseen to start operation in 2020 [82]. The EAST tokamak [83] is located in China and has a major radius of 1.85 m.

Finally, a key device for power exhaust studies is the medium sized tokamak ASDEX Upgrade at the Max Planck Institute for Plasma Physics (IPP) in Garching, Germany. As the investigations conducted within this thesis are based on experiments performed on ASDEX Upgrade, this device is introduced in more detail in section 3.2.

3.1.2 Experimental Power Exhaust Studies

In the following, an overview over various experimental studies concerning power exhaust and impurity seeding in different tokamaks is provided. The existing studies reveal, that the investigation of the impact of impurities on the plasma is an active field of research. This motivates the systematic investigations conducted in this work, which extend the existing studies via both, experimental and numerical methods.

In Alcator C-Mod, a series of dedicated discharges was performed to investigate the impact of different engineering parameters (input power, toroidal magnetic field, plasma current, plasma density) on the heat flux footprint (i.e., on the peak power load q_{max} and its radial fall-off length λ_q) at the outer divertor target plate [84]. The experiments have been performed under attached divertor conditions in L-mode and H-mode and in lower single-null and double-null configuration. It is reported that discharges with high thermal energy content are characterized by a narrow power channel width, which is attributed to the plasma current I_{P}. The observed fall-off length λ_q scales approximately with $1/I_{\mathrm{P}}$. The shape of the heat flux profile is independent of the toroidal magnetic field and of the power flux in the SOL. Instead, the magnitude and the width of the target heat flux profile follows the upstream electron pressure profile, while the pressure gradients in the boundary scale with I_{P}^2.

However, the dependence of the pressure gradient on the plasma current is lost as the divertor enters a high-recycling regime. The heat flux footprint is observed to be insensitive to different magnetic configurations (single-null versus double-null). Since a future reactor is foreseen to be operated at high I_P, this shows the importance of taking measures.

In [71] the development of a feedback system in Alcator C-Mod to control the target heat flux via impurity seeding is reported. Typically nitrogen seeding is applied to reduce the peak heat flux to the target to values below $10\,\mathrm{MWm^{-2}}$. It is reported that excellent core confinement can be maintained with nitrogen seeding. However, the feedback system only works reliably in steady state conditions. During transients the plasma can reattach, or X-point Marfes can result in a severe confinement degradation.

In JET H-mode plasmas total radiated power fractions of up to 70 % with argon and nitrogen are reported in [63]. While with argon seeding about 40 % of the injected power is radiated in the pedestal top region on closed flux surfaces, the nitrogen radiation is mostly located in the divertor region where a radiation fraction of 50 % is measured. In both cases good confinement with $H_{98} \approx 1$ can be maintained. However, in the analyzed discharges, it is observed that the characteristics of the Type I ELMs remain unchanged with impurity seeding, whereas a regime with Type III ELMs has to be achieved to reduce the transient heat loads onto the divertor targets to acceptable values for ITER.

Also in JET a real-time control system for the divertor detachment was developed [69]. The performance of the system is successfully demonstrated in H-mode discharges performed with the ITER-like wall. Impurity seeding of nitrogen, neon or argon is applied to reduce the target heat loads to acceptable values.

Elaborate detachment studies have also been conducted on ASDEX Upgrade. Until 2003 ASDEX Upgrade was equipped with a carbon wall which facilitated detachment, probably due to intrinsic carbon impurity contamination [57]. However, since the device is equipped with a full tungsten wall, complete divertor detachment in H-mode cannot be achieved anymore with deuterium fueling alone, even at high plasma densities. Only by applying significant nitrogen seeding it is possible to achieve complete detachment in H-mode [37]. In [37] it is shown that with nitrogen seeding the radiated power fraction increases to up to 85 % with a strongly localized radiation in the vicinity and above of the X-point. This X-point radiation is also accompanied by a pedestal top pressure loss of about 60 %, whereas the core pressure is only reduced slightly, by roughly 10 %. During the onset of detachment and the so-called fluctuating state (a transition from the onset of detachment to partial detachment) the inner target is detached in inter-ELM phases, while during

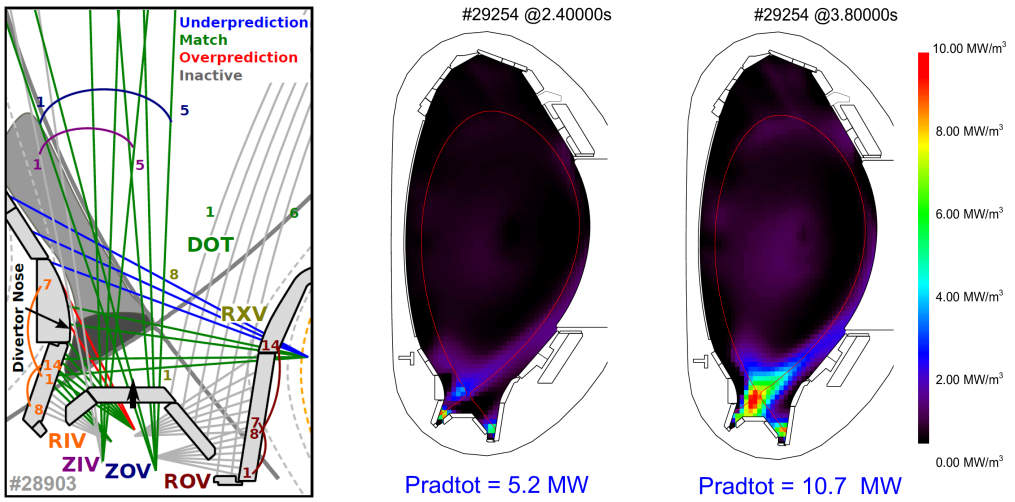

Figure 3.1: Left: Illustration of the extent of the HFSHD region (grey region) as described in [85], with the spectroscopy lines of sight used to detect the high density. Figure from [85]. Right: Radiation distribution calculated as tomographic reconstruction from the foil bolometer measurements before and during nitrogen seeding in the ASDEX Upgrade discharge #29254 [41]. Figure from [41].

the ELMs, the target reattaches. However, as soon as (partial) detachment of the outer target is achieved, induced by the nitrogen seeding, considerably decreased ELM sizes with an increased ELM frequency are observed. With the reduced ELM size, the ELMs are finally not able to cause the targets to reattach anymore.

Nitrogen seeding also has a strong impact on the High Field Side High Density (HFSHD) region, which is observed to appear in the SOL on the HFS above the X-point [37, 68], as displayed in figure 3.1 (left). The HFSHD region typically arises at high heating power and when the inner divertor is detached, while the outer divertor is still attached. It causes increased core fueling via diffusion across the separatrix and is correlated to a reduction of the plasma confinement [86]. The HFSHD region could also be reproduced by modeling, where the importance of drifts for its formation was revealed [85]. However, nitrogen seeding was shown to be applicable to suppress or even extinguish the HFSHD region. This can be explained by the radiative power dissipation, which reduces the power flux into the region. As the power dissipation limits the power available for the ionization processes which are required to sustain the high density, the impurity seeding finally results in its disappearance.

Apart from the investigations discussed above, moderate nitrogen seeding is

routinely applied in ASDEX Upgrade to reduce the target power loads [87]. However, also several other impurity species (like, e.g., argon, neon, krypton) have been investigated in various impurity seeding experiments (see, e.g., [41, 63, 70, 74]). A comparison of two ASDEX Upgrade H-mode discharges with argon and nitrogen seeding is presented in [41]. The observed radiation distribution before and during nitrogen seeding is shown in figure 3.1 (right). As expected from the radiation efficiency (see section 2.2.3), nitrogen radiates strongly in the divertor region, while argon predominantly radiates in the core in these experiments (with a divertor radiation around 5 MW for nitrogen, and 2 MW for argon, at roughly 12 MW of total radiation). In [41] also a considerable energy confinement improvement is observed with nitrogen seeding and a moderate improvement with argon, which is related to a better pedestal performance (i.e., due to a higher pedestal top temperature and an increased total plasma pressure [88]). However, at the same time impurity accumulation in the core leads to fuel dilution which should be limited, as it results in a reduced fusion rate in future fusion devices [47, 48].

3.2 The ASDEX Upgrade Experiment and Diagnostics

The upgraded *Axially Symmetric Divertor EXperiment*, short ASDEX Upgrade or AUG, is a research divertor tokamak located in Garching near Munich (Germany), operated by the Max Planck Institute for Plasma Physics (IPP). ASDEX Upgrade strongly contributes to the research of tokamak physics and to the extrapolation to future machines. The basic operational parameters of the device are summarized in table 3.1. With a full-tungsten first wall and high heating power, ASDEX Upgrade is one of the leading fusion experiments for ITER-relevant power exhaust and divertor studies.

ASDEX Upgrade – Operational parameters	
Major radius	1.65 m
Minor radius	0.5 m
Plasma volume	14 m^3
Plasma current	0.4 – 1.6 MA
Max. magnetic field	3.9 T
Max. heating power	27 MW
Max. pulse length	10 s
First wall material	Tungsten

Table 3.1: Operational parameters of the ASDEX Upgrade tokamak.

For the measurement of different plasma parameters within the plasma volume and on the wall surfaces, a variety of different plasma diagnostics are installed on

the machine. The most important diagnostics, especially those relevant for power exhaust studies, are briefly described in the following.

3.2.1 Magnetic Equilibrium Reconstruction

To allow a correct interpretation and localization of the different diagnostic signals, it is a key requirement to provide a magnetic equilibrium reconstruction which is as precise as possible. For this purpose a set of Mirnov coils [89] is distributed poloidally around the plasma vessel (as shown in figure 3.2a) to measure temporal changes in the magnetic flux outside of the plasma. These measurements are then used as boundary conditions in the CLISTE code [90] to reconstruct the magnetic equilibrium. This is achieved by numerically solving the Grad-Shafranov equation [91], which is a partial differential equation that connects the poloidal magnetic flux to the current in the plasma on surfaces of constant magnetic flux.

For the determination of fall-off lengths of density or temperature profiles at the plasma edge, it is not crucial to know the exact positions of measurements, if the gradient of the considered parameter is homogeneous. However, for the measurement of absolute local values, even small uncertainties in the equilibrium reconstruction can have a significant impact on the outcome. E.g., for steep radial profiles, characterized by small fall-off lengths in the order of a few mm (which is a typical value for, e.g., the heat flux fall-off length), a radial shift of the alleged separatrix position of a few mm can already make a substantial difference for the absolute values. Unfortunately, the uncertainty of the separatrix position can actually be on the scale of cm for ASDEX Upgrade in the worst case [92], which is a critical issue that should be kept in mind.

For plasma simulations (see chapters 4 – 6), the computational mesh is usually based on the magnetic equilibrium reconstruction obtained from experimental discharges. Therefore, a good reconstruction is also relevant for modeling.

3.2.2 Thomson Scattering

With the Thomson scattering system [93, 94] it is possible to obtain radial profiles of the electron density and temperature at the edge and in the core region (see figure 3.2a). The fundamental process is the elastic scattering of photons on free electrons in the plasma. A Nd-YAG laser beam is directed vertically into the plasma and the scattered light is detected by avalanche photo diodes. From the intensity of the scattered light it is possible to derive the electron density, while the electron temperature can be deduced from the Doppler broadening of the signal. Different measurement channels with a vertical spacing of 6 cm along the laser path allow

measurements at different radial positions and the reconstruction of radial profiles. The measurement positions are indicated in figure 3.2a. The profiles obtained from the Thomson scattering system can be strongly scattered, with statistical uncertainties in the order of 10 % for the electron density and 7 % for the electron temperature, and systematic uncertainties around 7 % in both cases.

As the Thomson scattering system measures electron density and temperature simultaneously, the obtained profiles are inherently aligned correctly. This circumstance can also be used for the proper alignment of profile measurements from other diagnostics. For this purpose the temperature profile from Thomson scattering is shifted such, that the electron temperature at the separatrix is at 100 eV (which is the typical value for ASDEX Upgrade in H-mode according to considerations from the Spitzer-Härm heat conductivity [45]). Then the same shift is applied to the density profile, which then acts as reference for other diagnostics measuring the electron density profile.

The availability of experimental upstream profiles is also relevant for the plasma simulations (chapters 4 – 6), as the profiles provide a guideline for the adaption of the transport coefficients which have to be specified by the user. This also applies to other diagnostics which provide data on upstream profiles (e.g., the lithium beam and ECE diagnostics in sections 3.2.3 and 3.2.4).

3.2.3 Lithium Beam

The lithium beam diagnostic [95, 96] provides profile measurements of the electron density in the edge region (see figure 3.2a). A neutral lithium beam with an energy of 60 keV is injected into the plasma, where the neutral lithium atoms undergo excitation and ionization by electron impact collisions or charge exchange processes. In this process the excited lithium particles emit line radiation, which is then measured by filtered photomultiplier tubes with a spatial resolution of roughly 5 mm. From the intensity of the spectral emissions, the electron density can be deduced. Due to the attenuation of the lithium beam in the plasma the measurement is limited to the edge region ($\rho_{\mathrm{pol}} \gtrsim 0.9$). Like the other diagnostics which provide data on upstream profiles, this diagnostic is also relevant for the reconstruction of profiles in plasma simulations. For the studies conducted in this work, lithium beam data was not available for all investigated discharges.

3.2.4 Electron Cyclotron Emission Radiometry (ECE)

The ECE diagnostic [97] is based on the emission of radiation at the second harmonic of the electron cyclotron frequency in a hot plasma. If the plasma is optically thick,

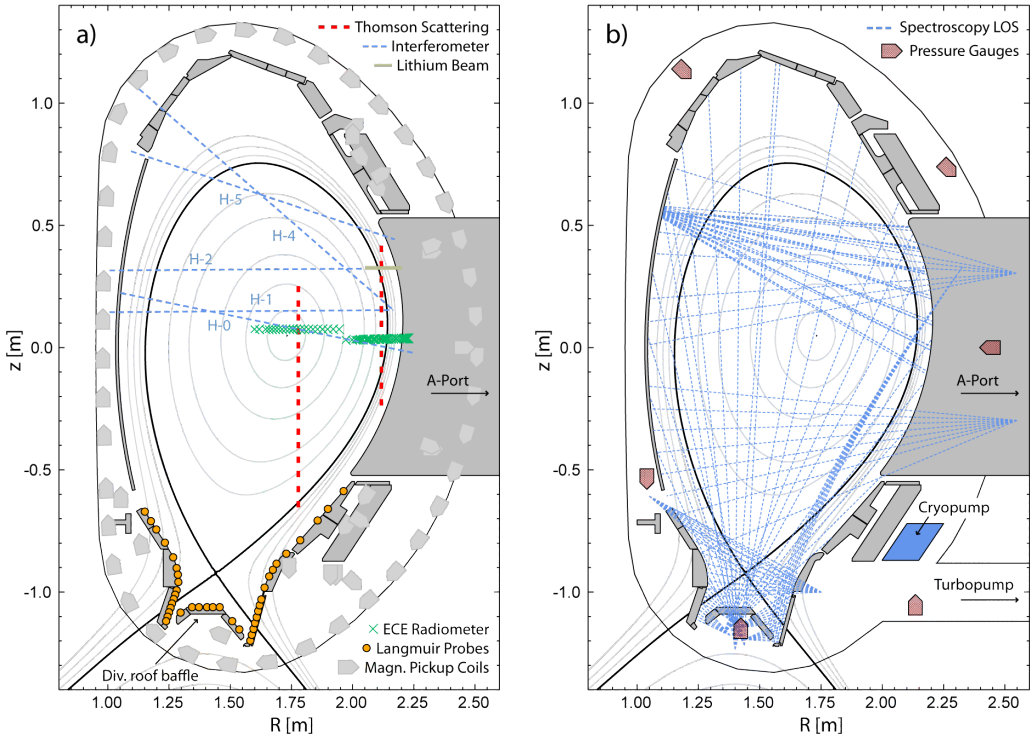

Figure 3.2: Overview over a selection of diagnostics installed on ASDEX Upgrade. a) The Thomson scattering system, interferometer lines of sight (LOS), lithium beam, ECE radiometer, lower divertor Langmuir probes and the magnetic pickup coils. b) The most important available spectroscopic LOS, a selection of ionization pressure gauges, and the pumping system with the cryopump and the turbopump. LOS which appear curved here have a toroidal component causing a seeming curvature in the poloidal projection, but are straight in physical space. The displayed magnetic equilibrium is taken from discharge #35358 (at $t = 3\,\mathrm{s}$).

it can be considered as black body radiator, and the electron temperature can be identified from the ECE intensity. As the electron cyclotron frequency depends on the magnetic field strength, which depends on the radial position, spectrally resolved ECE measurements allow the reconstruction of the radial electron temperature profile. However, in the edge and SOL, the ECE measurements are not very reliable, due to the low optical thickness in these regions, which results in shine through and apparently too high temperatures. In addition to the standard deviation of the statistical scatter of the data within the considered time frame, a systematic

uncertainty of 7 % plus a digitization error of 15 eV have to be taken into account [97]. The measurement regions of the ECE diagnostic are depicted in figure 3.2a. Like the other diagnostics which provide data on upstream profiles, this diagnostic is also relevant for the reconstruction of profiles in plasma simulations.

3.2.5 Interferometry

Via interferometric measurements, the line integrated electron density along five different lines of sight (LOS) in the plasma edge and core can be determined. For this purpose a laser beam is split into a reference beam (bypassing the plasma) and a sample beam, which is sent through the plasma. As the phase velocity of electromagnetic waves in a plasma depends on the plasma density, the density can be deduced from the phase shift between reference and sample beam. The ASDEX Upgrade interferometry system uses phase-modulated Mach-Zehnder interferometers and a DCN laser with a wavelength of 195 μm [98]. The uncertainty of the interferometry measurements is about 2 %. The different interferometer LOS are displayed in figure 3.2a. As this diagnostic does not provide spatially resolved data, it is less relevant for modeling, but it is very useful to display the time evolution of the density along the different LOS throughout an experimental discharge.

3.2.6 Spectroscopy

The spectroscopy system in ASDEX Upgrade allows to record spectrograms measured along various different LOS within the divertor and main chamber, which are shown in figure 3.2b. Via a glass fiber system, the different LOS can be connected to the spectrometers allowing variable configurations optimized for the specific requirements. The available spectrometers offer measurements at different spectral ranges. In the standard configuration a spectral range of 396 – 411 nm is applied. With this setting, the Balmer D_ϵ and D_δ lines (at 397 nm and 410 nm), the NII-singlet (at 399.5 nm) and the NIII-doublet (409.7 nm and 410.3 nm) lines are recorded by default. From the data several plasma parameters can be determined in a single measurement. From the Stark broadening of the Balmer lines it is possible to determine the electron density [99, 100]. With the ratio of the discrete-to-continuum background emission it is possible to assess the electron temperature [101].

To allow detailed studies of impurity seeded plasmas, improved methods to measure the impurity content in the plasma had to be developed, as this information is not provided by default by the basic standard diagnostics. Often only inaccurate estimates, e.g., based only on the atomic influx taken from the gas valves [102] are available. However, to assess the nitrogen content in the plasma, the nitrogen lines

from the spectroscopy measurements can be used [103, 104]. For this purpose, a method based on the sensitivity of the NII line intensities to the electron density and temperature is applied, which substantially extends the spectrum of measurable plasma parameters.

3.2.7 Bolometry

With the bolometry systems [105] in ASDEX Upgrade it is possible to measure the total radiation distribution within the plasma volume. For this purpose an elaborate system of various different bolometer channels, each measuring the integrated radiation along a single LOS, is installed. Two different bolometer types are used: 128 channels of absolutely calibrated foil bolometers [106] and 256 channels of fast AXUV diode bolometers [107]. The foil bolometers are based on the measurement of the temperature dependent resistance of a meander structure attached to the foil, which is heated by the radiation. In the diode bolometers the incoming radiation induces a photocurrent that can directly be measured. While the diode bolometers have a higher data acquisition rate of 200 kHz (compared to 2 kHz for the foil bolometers), they are not absolutely calibrated and have a lower sensitivity in the ultraviolet spectral range. Apart from the consideration of single LOS also a 2D representation of the radiation distribution can be deduced from the bolometry measurements via a tomographic reconstruction. The reconstruction of the radiation distribution is of great importance to investigate the impact of impurity seeding on the plasma, and therefore, bolometry is an important tool for power exhaust studies.

3.2.8 Infrared Thermography

The heat load onto the outer divertor target can be determined by infrared thermography [108] with a spatial resolution of 0.6 mm. This diagnostic uses an infrared camera observing the outer divertor target. The photon flux emitted by the target surface is related to the surface temperature according to Planck's law. With the temporal evolution of the measured infrared temperature and the heat diffusion equation in the target tile material the heat flux onto the target surface is reconstructed via the 2D heat transport code THEODOR [109]. Consequently, the infrared thermography is of great relevance for power exhaust studies. However, under detached conditions and at high divertor densities the infrared thermography has a poor signal to noise ratio and the heat flux cannot be reliably determined.

3.2.9 Pressure Gauges

With the pressure gauges [110, 111] distributed in the plasma vessel at different positions in ASDEX Upgrade, the neutral particle pressure outside the plasma can be determined. This is done with ionization pressure gauges. If a neutral particle enters the pressure gauge, it is ionized by electron impact, resulting in an ion current which is then detected. With this setup flux densities are measured. These can be converted to a neutral density or pressure under the assumption of an isotropic thermal flux and with the average velocity $v_{\mathrm{av}} = 1240\,\mathrm{ms}^{-1}$ of D_2 particles at room temperature by the simple conversion formula $\Gamma_0 = n_0 v_{\mathrm{av}}/4$. The positions of a subset of the available ionization pressure gauges in ASDEX upgrade are provided in figure 3.2b.

With the pressure gauges it is possible to compare the neutral pressure from the simulations with the experiment, which is important for the plasma fueling. Unfortunately, it turns out, that it is often difficult to match simulation and experiment. However, with modifications to the neutral conductance in the subdivertor structure in the simulations, it is at least possible to match the neutral compression (i.e., the ratio of upstream and divertor pressure) to the experiment.

3.2.10 Langmuir Probes

Langmuir probes [112] can be used to measure different plasma parameters, like the electron density, the electron temperature, the electric potential of the plasma and the electron and ion saturation current $j_{\mathrm{sat}} \propto n\sqrt{T}$. As the Langmuir probes have to be in direct contact with the plasma, they are used to measure the plasma parameters at the material surfaces of the vessel walls. Usually, a Langmuir probe measurement is performed by sweeping the operational voltage and recording the resulting current-voltage (I-V) characteristic. From this characteristic I-V curve and with the effective probe surface area it is possible to derive the plasma parameters.

In the ASDEX Upgrade divertor in addition to single probes, predominantly so-called triple probes [113] are used. These consist of three electrodes that measure three different points of the I-V curve simultaneously. This method provides less information compared to the conventional single probe measurement, however, without the necessity of voltage sweeps, a considerably higher data acquisition rate can be achieved.

The power supply of the Langmuir probes in ASDEX Upgrade is provided by batteries with a limited voltage, which only allows a reliable measurement of temperatures below 25 eV, while the lower temperature limit for a reliable measurement is at

roughly 2 eV. The spatial resolution of the Langmuir probe diagnostics is around 2 – 3 cm, and strike point sweeps are required to obtain target profiles with an increased resolution. The positions of the Langmuir probes in the ASDEX Upgrade experiment are indicated in figure 3.2a.

Providing information on different plasma parameters at the divertor targets, the Langmuir probes are a very important tool for power exhaust studies. In plasma simulations the transport coefficients are usually only adjusted according to the experimental upstream profiles. However, in the ideal case, also the target profiles should be similar to the Langmuir probe data, especially if it is aimed to obtain a detailed reconstruction of the experimental discharge.

3.2.11 Shunt Current Measurements

Temperature differences between the inner and outer divertor target result in (thermo-)electric currents into the target tiles [87, 114]. As the inner divertor plasma is usually at low temperatures, this allows to obtain an indirect measure of the outer target temperature. For this purpose shunt current measurements are performed at the target plates for which a shunt resistor is embedded in the tile mounting. To obtain a parameter which can be interpreted as a divertor temperature, the measured current is rescaled by a fixed factor which is determined according to a comparison to Langmuir probe data. The resulting value is expressed in electronvolts and denoted as T_{div}. It was shown that this simple and robust method serves as a good indicator to assess the divertor conditions in real-time and that T_{div} usually also agrees well with the actual plasma temperature at the divertor target [87]. However, it has to be noted that due to the origin of this parameter, T_{div} can also have negative values. A negative value of T_{div} is a robust indication for pronounced divertor detachment [56], whereas $T_{\mathrm{div}} \lesssim 10\,\mathrm{eV}$ can be interpreted as partial detachment. Consequently, the shunt current measurements are very useful for investigations of divertor detachment and power exhaust.

3.2.12 Gas Puff and Pumping Systems

For the investigation of impurity seeding and power exhaust, the behavior of neutral particles within the device is of great importance. As this behavior is directly affected by the gas puff and pumping systems, these are presented briefly in the following.

For the deuterium fueling and the impurity seeding various gas valves are distributed around the torus. Typically the deuterium fueling is done from the so-called DuX and DuB valves which provide fueling from the private flux region. Several DuX and DuB valves exist with a total of 12 outlets, located in the divertor roof

baffle (see figure 3.2a) with a regular toroidal distribution. Additional valves are also available at different poloidal positions, e.g., to test different deuterium fueling positions or for impurity seeding. Here only the valves in the so-called A-port (see figure 3.2) are to be mentioned, which allow seeding (or fueling) from the outer midplane position as it is also applied in this work.

The pumping system consists of turbomolecular pumps and a toroidally symmetric cryopump. The turbopumps are high-performance vacuum pumps with a pumping speed of $14\,\mathrm{m^3 s^{-1}}$ [115]. The cryopump is cooled by liquid nitrogen and helium and works via condensation of particles on a 4.2 K cold surface of the cryopanel, resulting in a pumping speed of $100\,\mathrm{m^3 s^{-1}}$ [116]. As the cryopump collects particles over time it has to be regenerated regularly. Both pumping systems are located on the LFS at the bottom of the machine, behind the outer divertor (see figure 3.2b).

3.3 Experimental Investigations of Mixed Impurity Seeding

Considering power exhaust and the expected impurity radiation in a next-step device like ITER or DEMO, it is often discussed that impurity radiation in the SOL alone will not be sufficient to protect the plasma facing components [42]. A considerable fraction of the fusion power, in the order of 75 % for DEMO, will be required to be radiated from within the core [117], assuming an ITER-like divertor geometry. Therefore, impurity seeding of higher Z species, which are characterized by enhanced radiation within the closed flux surfaces, might be well suited for such devices. In order to optimize the radiation distribution it might also be beneficial to consider a mixture of different impurity species. For this purpose, a set of dedicated ASDEX Upgrade discharges has been performed with simultaneous impurity seeding of nitrogen and argon [73]. As discussed in sections 2.2.3 and 3.1.2, with this choice of impurity species, a typical divertor radiator (nitrogen) is opposed to an impurity with an enhanced radiation contribution in the SOL and edge region (argon). The experimental setup and the analysis of these dedicated discharges is presented in the following.

3.3.1 Experimental Setup

To be able to compare different argon to nitrogen mixing ratios, the experimental setup of the ASDEX Upgrade discharges #35157, #35158, #35358 and #35381 was designed to provide experimental data under similar steady state conditions with (partially) detached divertor targets at different Ar/N fractions. The experiments

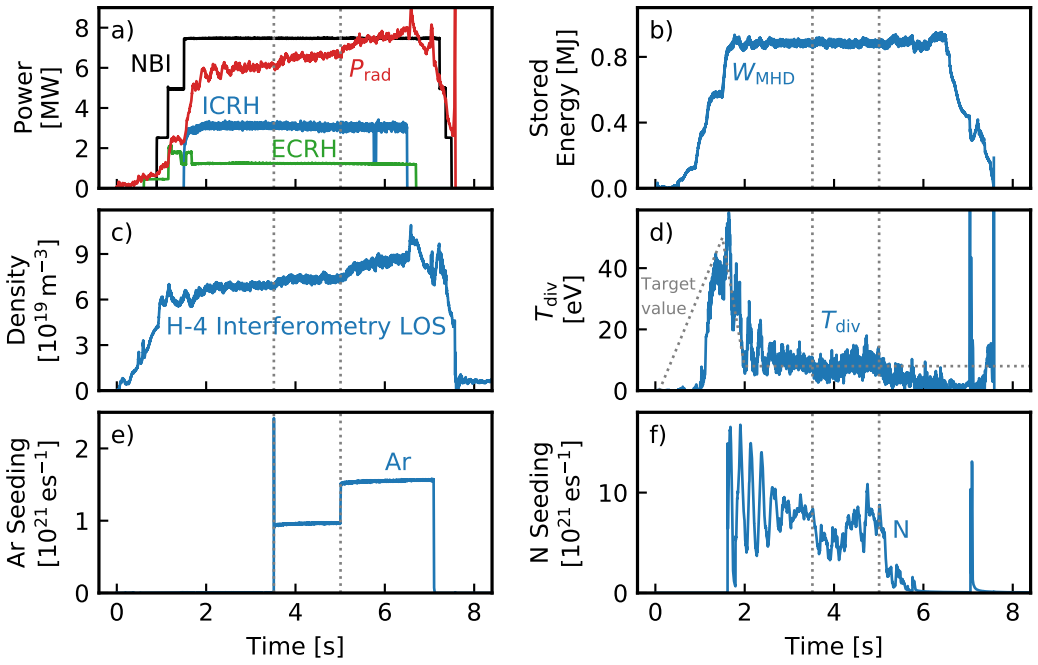

Figure 3.3: Time traces of the ASDEX Upgrade discharge #35358. a) Heating power of the neutral beam injection (NBI), the ion cyclotron resonance heating (ICRH) and the electron cyclotron resonance heating (ECRH) as well as the total radiation power (P_{rad}). b) Stored plasma energy W_{MHD}. c) Density measurements from the DCN interferometry. d) Outer divertor control signal T_{div} and the target value $T_{\mathrm{div,\,trgt}}$ (dashed line). e, f) Nitrogen and argon impurity seeding level.

have been performed with increasing argon seeding steps, and a feedback scheme on the nitrogen seeding, aimed to keep the divertor stable in a (partially) detached state. For this purpose T_{div} was used as a control signal, which is obtained from shunt current measurements and is a good indicator for the divertor state (cf. section 3.2.11). The experiments were conducted in forward field configuration (i.e., with the ∇B-drift pointing down) at a toroidal magnetic field of 2.5 T and a plasma current of 1 MA. The safety factor q_{95} (i.e., the safety factor close to the separatrix at $\rho_{\mathrm{pol}} = \sqrt{0.95}$) was around 4.0 in all conducted discharges and the heating power was set to values between 12.5 MW and 13.5 MW. To obtain partial and complete detachment, the feedback target value for T_{div} was either set to 8 eV, or to 0 eV and argon seeding levels of up to $1.7 \cdot 10^{21}\,\mathrm{es}^{-1}$ were applied (in electron equivalent units).

For argon seeding levels below the calibration limit of the gas valves, an on-off

modulation had to be used to obtain the desired average seeding level values. It was shown in [73] that a modulation period of 170 ms was longer than the argon residence time in the divertor, resulting in an undesired modulation of the argon content. However, with a modulation duration of 60 ms (i.e., 20 ms on and 40 ms off or 40 ms on and 20 ms off), a constant argon content could be achieved [73].

3.3.2 Time Traces and Choice of Considered Time Slices

Some exemplary time traces of the ASDEX Upgrade discharge #35358 – one of the mixed Ar/N discharges – are shown in figure 3.3. In panel a) the heating power contributions from NBI, ICRH and ECRH with a total power of 12.5 MW are displayed, as well as the total radiation loss, which keeps increasing with higher argon seeding steps. Panel b) shows the stored energy in the plasma, which remains constant throughout the discharge. The plasma density deduced from interferometry is depicted in panel c) showing a slight increase, especially during the last argon seeding step. The control signal T_{div} and the specified target value $T_{\mathrm{div,\,trgt}}$ (dashed line) are plotted in panel d). Finally, the argon and nitrogen impurity seeding levels are displayed in panels e) and f). The increasing argon seeding steps are marked by the vertical dashed lines in all plots. It can be seen how the nitrogen seeding is reduced with increasing argon seeding, according to the feedback scheme on the

Discharge	Time	$T_{\mathrm{div,\,trgt}}$	Γ_{N} [es^{-1}]	Γ_{Ar} [es^{-1}]	f_{Ar}
#35157	2.7 – 3.0 s	8 eV	$1.64 \cdot 10^{22}$	-	0 %
#35157	4.7 – 5.0 s	8 eV	$1.24 \cdot 10^{22}$	$3.0 \cdot 10^{20}$	2.4 %
#35158	2.7 – 2.9 s	0 eV	$1.96 \cdot 10^{22}$	-	0 %
#35158	3.7 – 4.0 s	0 eV	$1.75 \cdot 10^{22}$	$3.3 \cdot 10^{20}$	1.9 %
#35158	4.3 – 4.6 s	0 eV	$1.57 \cdot 10^{22}$	$6.7 \cdot 10^{20}$	4.1 %
#35158	5.7 – 6.0 s	0 eV	$1.07 \cdot 10^{22}$	$1.0 \cdot 10^{21}$	8.5 %
#35358	3.2 – 3.5 s	8 eV	$8.14 \cdot 10^{21}$	-	0 %
#35358	4.2 – 4.5 s	8 eV	$6.65 \cdot 10^{21}$	$9.5 \cdot 10^{20}$	12.5 %
#35358	5.5 – 5.8 s	8 eV	$6.34 \cdot 10^{20}$	$1.6 \cdot 10^{21}$	71.6 %
#35381	2.1 – 2.4 s	8 eV	$1.71 \cdot 10^{22}$	-	0 %
#35381	3.0 – 3.3 s	8 eV	$8.03 \cdot 10^{21}$	$1.0 \cdot 10^{21}$	11.1 %

Table 3.2: Time slices selected for the mixed Ar/N seeding studies. The last column also shows the argon seeding fraction $f_{\mathrm{Ar}} = \frac{\Gamma_{\mathrm{Ar}}}{\Gamma_{\mathrm{Ar}}+\Gamma_{\mathrm{N}}}$. Choice of time slices according to [73].

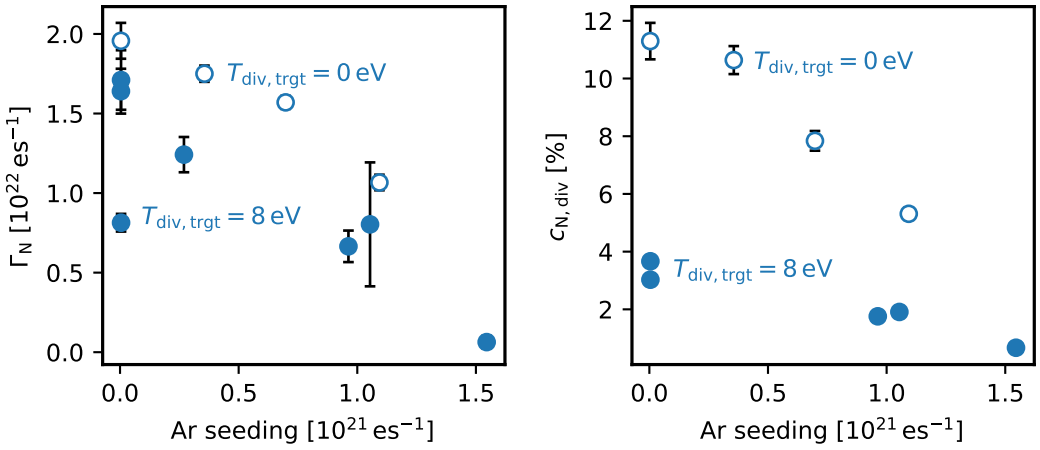

Figure 3.4: The nitrogen seeding level Γ_N and the nitrogen concentration $c_{N,div}$ in the outer divertor according to spectroscopy measurements [103, 104] for the selected time slices from the mixed Ar/N discharges. The data is plotted against the argon seeding level which determines the argon fraction in the impurity mixture. Filled symbols represent time slices with $T_{div,trgt} = 8$ eV, hollow symbols depict time slices with $T_{div,trgt} = 0$ eV. The values are determined as the average of the quantity within the considered time window and the error bars show the standard deviation of the data.

control signal T_{div}. However, in the last argon seeding step after $t \approx 5.8$ s, the target value of $T_{div,trgt} = 8$ eV cannot be met anymore, as the argon seeding has already completely replaced the nitrogen seeding, which therefore, cannot be reduced any further by the feedback scheme. As indicated by the H-4 interferometer signal, this also has an impact on the upstream conditions. Therefore, if the intention is to compare different time slices with similar plasma and divertor conditions, care has to be taken regarding their choice. In the shown example time slices after $t \approx 5.8$ s should be disregarded, while the earlier part of

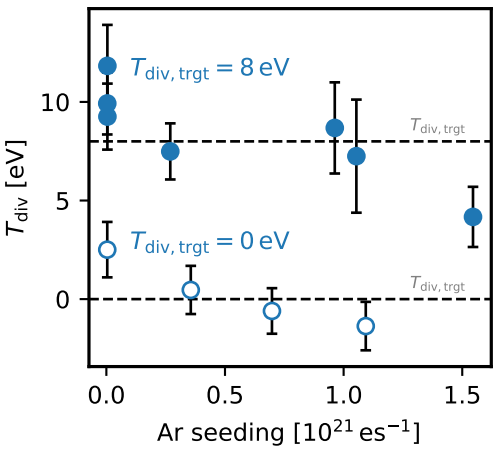

Figure 3.5: The measured control signal T_{div} plotted against the argon seeding level for the selected time slices from the mixed Ar/N discharges.

the discharge with almost steady state conditions provides a reasonable comparability due to similar plasma conditions. The same considerations are also taken into account for the other discharges.

Table 3.2 lists a summary of all time slices from the different discharges considered in the following analysis, including the target values $T_{\mathrm{div,\,trgt}}$ and the impurity seeding levels. For all selected time slices, figure 3.4 shows the evolution of the feedback controlled nitrogen seeding level and the nitrogen concentration in the outer divertor with increasing argon seeding. As expected, the nitrogen seeding is gradually reduced as the argon seeding increases, according to the feedback scheme. In figure 3.5, the resulting values of the control signal T_{div} are plotted against the argon seeding level. Time slices with a target value of $T_{\mathrm{div,\,trgt}} = 8\,\mathrm{eV}$ are represented by filled symbols, and time slices with $T_{\mathrm{div,\,trgt}} = 0\,\mathrm{eV}$ by hollow symbols. In some of the cases a considerable deviation of the actual values of T_{div} from the specified target values (dashed lines in figure 3.5) can be observed.

The difference between the time slices with $T_{\mathrm{div,\,trgt}} = 8\,\mathrm{eV}$ and $T_{\mathrm{div,\,trgt}} = 0\,\mathrm{eV}$ is illustrated in figure 3.6, showing the target profiles of the ion saturation current j_{sat}. The plots contain the combined Langmuir probe data of all time slices with the respective target temperature. The errorbars indicate the standard deviation of the data points. The difference between the profiles is visible close to the separatrix, where the ion saturation current decreases as $T_{\mathrm{div,\,trgt}}$ is reduced from 8 eV to 0 eV, indicating increasing detachment. However, in the PFR and in the far SOL the difference between the two different profiles is remarkably small, which is surprising and currently not fully understood.

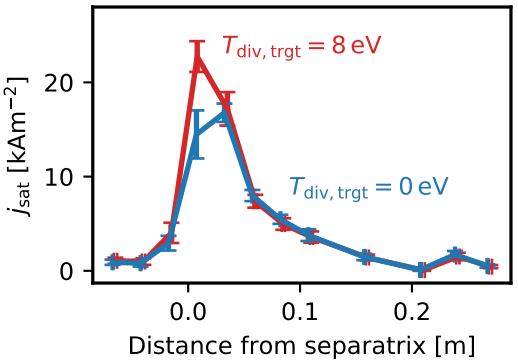

Figure 3.6: Target profiles of the ion saturation current j_{sat} at the outer divertor target, according to Langmuir probe data.

3.3.3 Experimental Observations and Analysis

In figure 3.7 several upstream profiles of electron density and temperature from different time slices of the mixed Ar/N seeding discharges are plotted. The profiles are taken from the time intervals with a target value of $T_{\mathrm{div,\,trgt}} = 8\,\mathrm{eV}$ (i.e., only a subset of the time slices given in table 3.2 is used). To obtain the profiles, the Thomson scattering diagnostic was used, as well as the lithium beam data, when it

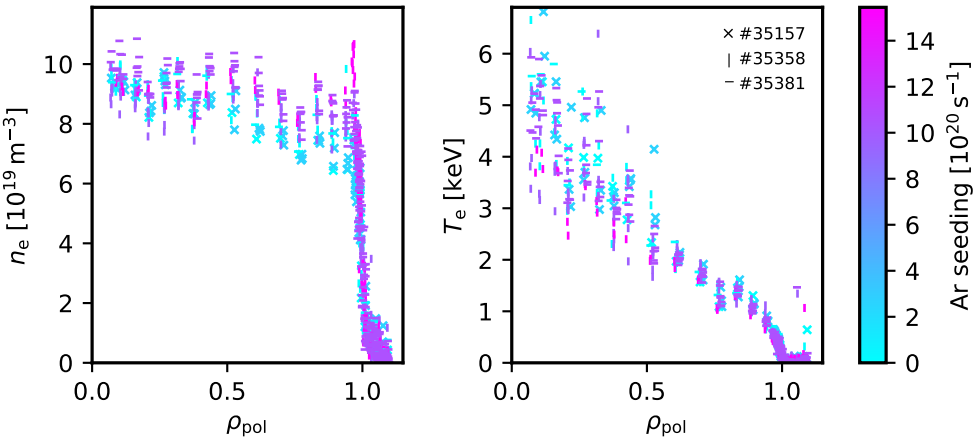

Figure 3.7: Experimental upstream profiles of electron density and temperature from different discharges and time slices with different argon seeding levels (as indicated by the color coding), but otherwise comparable plasma conditions. All cases are with mixed impurity seeding, i.e., they also contain nitrogen seeding, which is reduced with increasing argon seeding level, as shown in figure 3.4 (left). The data was obtained via Thomson scattering and (if available) via the lithium beam diagnostic.

was available. An outward shift of 9 mm had to be applied to the edge Thomson scattering data to set the electron temperature at the separatrix position to 100 eV (cf. section 3.2.2). Subsequently, the data from the core Thomson scattering was shifted inwards by 25 mm, in order to align the core and edge measurements. These shifts (which are typical for the Thomson scattering system) were applied to all Thomson scattering measurements (i.e., to both, temperature and density) and to all considered discharges and time intervals. The average argon seeding level within the particular time window of the profiles in figure 3.7 is indicated by the color coding. Considering the data points at the highest argon seeding level, figure 3.7 indicates that the electron temperature in the core region drops with increasing argon content by about 25 – 30 %, whereas the electron density slightly increases. This can also be seen in figure 3.8, where the average electron density and electron temperature in different radial regions in the plasma core and edge are plotted against the argon seeding level for all considered time slices (now also including $T_{\mathrm{div,trgt}} = 0$ eV, again represented by hollow symbols). The core temperature drops considerably with increasing argon fraction, while the temperature in the plasma edge stays rather constant. This is caused by a strongly increasing core radiation, while the total radiation only increases slightly (see figure 3.9), as it is expected for argon due to the higher core radiation efficiency (cf. figure 2.5).

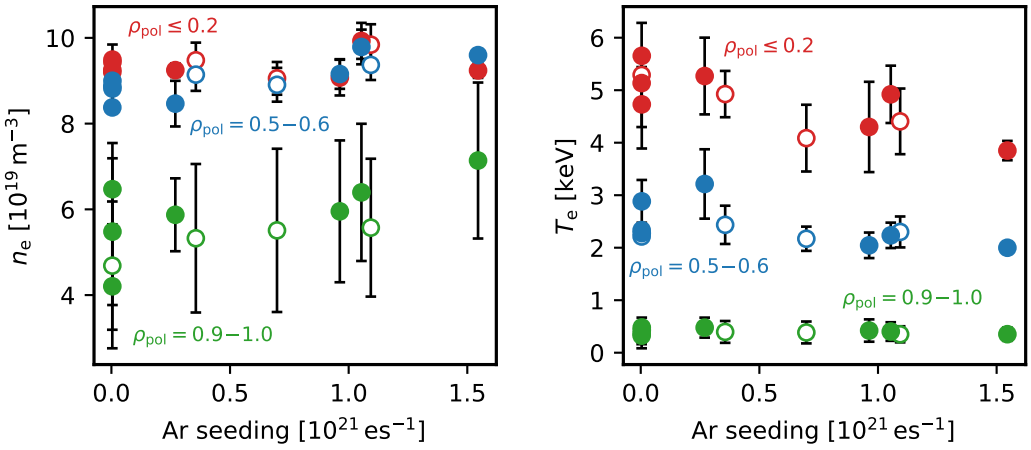

Figure 3.8: Electron density n_e and electron temperature T_e, obtained from the Thomson scattering profiles via a binning of the data within radial ranges of $\rho_{pol} \leq 0.2$, $\rho_{pol} = 0.5-0.6$ and $\rho_{pol} = 0.9-1.0$. The errorbars indicate the standard deviation of the data points within the corresponding radial range. Filled and hollow symbols discriminate different values of $T_{div,trgt}$, as in figure 3.4.

In summary, the experimental observations indicate that there is a smooth transition in which the nitrogen impurities are replaced by argon, gradually shifting the radiation distribution into the confined region. With this, the initial speculation that the impact of the impurities on the plasma can be influenced by the choice of the impurity mixture can be corroborated. This motivates a more detailed analysis of the processes that determine the behavior of impurities in the plasma, in order to facilitate an optimization of the impurity seeding schemes anticipated for future fusion devices. In this work, such an extended analysis is performed via plasma simulations, which are described in more detail in the following chapters. It will

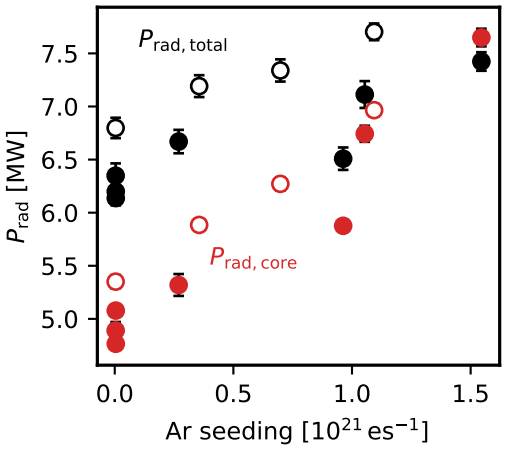

Figure 3.9: Main chamber (red) and total radiation (black), derived from bolometric measurements, plotted against the argon seeding level. Filled and hollow symbols discriminate different values of $T_{div,trgt}$, as in figure 3.4.

be investigated whether the experimental observations can be reproduced in the simulations, and the underlying physical mechanisms determining the radiative behavior and the radiation distribution will be analyzed.

Chapter 4

Fluid Codes and the SOLPS 5.0 Code Package

Numerical simulations are an important tool in various scientific fields, especially where experiments are costly, not feasible, not (yet) available or difficult to interpret. Consequently, numerical simulations are applied in different fields of fusion research, where they can be used for interpretative studies of experimental discharges, for comprehensive parameter scans, or to a certain degree also for predictive studies concerning future fusion devices like ITER or DEMO to guide their development. In this chapter, the general functionality of scrape-off layer fluid codes is presented with a focus on the SOLPS 5.0 code package and an overview over the current status of SOLPS modeling is provided.[1]

4.1 Scrape-Off Layer Fluid Codes

One major drawback of experimental analyses is the lack of measurability of certain plasma parameters, or insufficient measurement precision (like, e.g., for the impurity concentrations in the divertor [102, 103, 119]). Therefore, in addition to the experimental investigations, also several numerical studies are dedicated to power exhaust and impurity seeding [55, 120–128]. These studies cover different issues, like comparisons of the radiative properties of different impurity species in linear devices [121] and in tokamaks [122], the divertor impurity retention [55], alternative divertor configurations [124–126] and also predictive modeling for ITER [127].

Various code applications have been developed during the progression of fusion research, supported by the continuously increasing computational capabilities over the last decades. A few examples of such codes used for simulations of the SOL and edge plasma are SOLPS [129–131], EDGE2D [132], or UEDGE [133]. These are 2D codes, which are based on a two-dimensional numerical treatment. In addition to 2D codes, also 3D codes have been developed, like BoRiS [134], TOKAM3X [135]

[1] Part of this material was already published in [118].

or EMC3 [136]. These 3D codes can also be used for the modeling of toroidally asymmetric systems, like stellarators or magnetic perturbations in tokamaks [137]. However, since calculations in three dimensions are computationally more expensive, and usually also not required in a toroidally symmetric system like a tokamak, it is often sufficient to reduce the problem to a two-dimensional geometry.

The existing codes do not only differ in terms of geometry (1D, 2D or 3D) and required computational effort (from a few minutes to weeks of CPU time), but also in the physics addressed (time dependent or steady state simulations, self consistent simulations or calculations on a fixed plasma background, fluid or (gyro-)kinetic treatment of particles, etc.) [138]. Accordingly, some of the codes have certain drawbacks, e.g., the lacking implementation of volume recombination and drifts in EMC3. As SOLPS incorporates the description of a vast amount of physical processes and also supports the treatment of a large number of impurity species, it is well equipped for the power exhaust studies conducted in this work and is chosen as preferred numerical tool for this thesis. More details about the SOLPS code are provided in the following section 4.2.

Many of the codes are often coupled to EIRENE [139] for the treatment of neutral particles (e.g., EDGE2D-EIRENE [140], EMC3-EIRENE [136, 141]). As this is also the case for SOLPS, the coupling to EIRENE is also explained in more detail in section 4.2.6.

4.2 SOLPS 5.0

SOLPS (which stands for *"Scrape-Off Layer Plasma Simulation"*) is a code package combining the fluid plasma code B2.5 and the kinetic Monte Carlo neutral code EIRENE. Additionally, some tools for the grid generation (DivGeo, Carre, Uinp) and for post-processing (B2plot) are provided within the SOLPS code package. Apart from these tools, various individual routines have been developed during the work on this thesis, e.g., for the monitoring of large numbers of simultaneously running simulations, for automatic case generation, pre- and post-processing as well as for elaborate data analysis. The most recent version of the SOLPS code is SOLPS-ITER [130, 131]. However, by the time when the work on this thesis was started, SOLPS-ITER was not yet fully developed, which is why for this thesis the previous version (i.e., SOLPS 5.0 [129]) is used, which is described in this section.

The main part of the SOLPS code is B2.5, a multi-fluid plasma transport code solving a system of modified Braginskii equations on a two-dimensional curvilinear, topologically rectangular mesh. Some details of the code are discussed in the

following, in particular the generation of the computational mesh, the description of the parallel transport via the fluid approach and the Braginskii equations, the diffusive perpendicular transport, boundary conditions and the B2.5 neutral fluid model.

4.2.1 Computational Grid Generation

For the computational mesh, a magnetic equilibrium has to be specified by the user, usually taken from the magnetic reconstruction from a plasma discharge. From the magnetic equilibrium a two-dimensional numerical grid is generated that is aligned to the magnetic flux surfaces. A typical SOLPS grid based on a magnetic equilibrium from ASDEX Upgrade is presented in figure 4.1, showing the physical grid on the left, and the corresponding numerical grid on the right, including a description of the different regions and boundaries. Since SOLPS is a SOL and edge code, the computational domain does not contain the whole core region, but only a part of the core, as it can be seen in figure 4.1, left. The x-direction in the numerical grid corresponds to the poloidal direction in physical space, and the y-direction corresponds to the radial direction. Usually the grid is chosen to have a high spacial resolution around the separatrix in radial direction (i.e., narrow flux surfaces) and in front of the divertor target plates in poloidal direction (i.e., a high density of cells close to the divertor targets). The numerical grid resolution (i.e., the total number of poloidal and radial grid cells) is specified by the user. A typically recommended grid resolution for ASDEX Upgrade or machines of similar size is 48x18 or 96x36 (number of poloidal times radial cells). While a higher resolution is beneficial for resolving strongly localized effects, like sharply peaked or steep profiles, it also requires more computational effort and, therefore, increases the computational time required for a simulation.

4.2.2 The Braginskii Equations

In the following, the derivation of the Braginskii equations is briefly presented on the basis of a more detailed discussion as it can be found in [142]. The probability to find a particle within a certain phase space volume $d^3r d^3v$ around the position $\boldsymbol{r}$ and velocity $\boldsymbol{v}$ is determined by the Boltzmann distribution function $f(\boldsymbol{r}, \boldsymbol{v})$. With this the kinetic equation can be formulated:

$$\frac{\partial}{\partial t} f(\boldsymbol{r}, \boldsymbol{v}) + \boldsymbol{v} \cdot \nabla f(\boldsymbol{r}, \boldsymbol{v}) + \boldsymbol{b} \cdot \nabla_v f(\boldsymbol{r}, \boldsymbol{v}) = 0, \tag{4.1}$$

with the acceleration $\boldsymbol{b}$. Considering only electromagnetic forces, i.e., $\boldsymbol{b} = \frac{q}{m}(\boldsymbol{E} + \boldsymbol{v} \times \boldsymbol{B})$ (with particle charge q and mass m, the electric field $\boldsymbol{E}$ and the

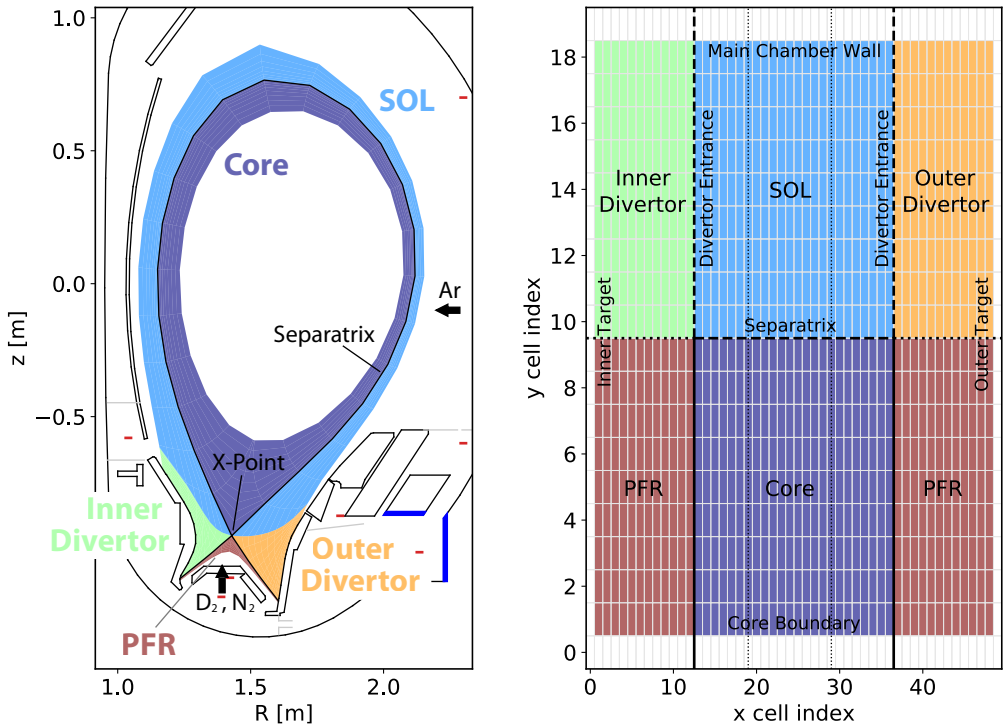

Figure 4.1: A SOLPS computational grid, based on the magnetic equilibrium of the ASDEX Upgrade discharge #29256. The numerical grid is shown on the right, and the corresponding representation in physical space on the left, where also parts of the vessel structure, including the neutral pumping surfaces behind the outer divertor (blue surfaces) and test surfaces to determine the neutral pressure (red surfaces) are displayed. The gas puff positions of D_2, N_2 and Ar are indicated by arrows. As it can be seen, the computational domain only contains a part of the core region (in this case $\rho_{pol} \gtrsim 0.9$).

magnetic field $\boldsymbol{B}$), the Vlasov-Equation is obtained:

$$\frac{\partial}{\partial t} f(\boldsymbol{r}, \boldsymbol{v}) + \boldsymbol{v} \cdot \nabla f(\boldsymbol{r}, \boldsymbol{v}) + \frac{q}{m} (\boldsymbol{E} + \boldsymbol{v} \times \boldsymbol{B}) \cdot \nabla_v f(\boldsymbol{r}, \boldsymbol{v}) = 0. \tag{4.2}$$

Under consideration of collisions with the Boltzmann collision term $\left(\frac{\partial f(\boldsymbol{r},\boldsymbol{v})}{\partial t}\right)_{coll.}$ this becomes the Boltzmann-Equation:

$$\frac{\partial}{\partial t} f(\boldsymbol{r}, \boldsymbol{v}) + \boldsymbol{v} \cdot \nabla f(\boldsymbol{r}, \boldsymbol{v}) + \frac{q}{m} (\boldsymbol{E} + \boldsymbol{v} \times \boldsymbol{B}) \cdot \nabla_v f(\boldsymbol{r}, \boldsymbol{v}) = \left(\frac{\partial f(\boldsymbol{r}, \boldsymbol{v})}{\partial t}\right)_{coll.}. \tag{4.3}$$

Considering a population of non-thermal particles in a thermalized background, one obtains the Fokker-Planck-equation by replacing the Boltzmann collision term with the Fokker-Planck collision operator:

$$\left(\frac{\partial f_1(\boldsymbol{v},t)}{\partial t}\right)_{coll.} = \gamma f_1(\boldsymbol{v},t) + \gamma \boldsymbol{v}\cdot\nabla_v f_1(\boldsymbol{v},t) + \frac{T}{\alpha}\nabla_v^2 f_1(\boldsymbol{v},t) \tag{4.4}$$

with the distribution function of the non-thermal part $f_1(\boldsymbol{v},t)$, the temperature T of the thermalized background, the friction coefficient α and the deceleration time $\gamma = \frac{m}{\alpha}$.

With the distribution function $f_a = f_a(\boldsymbol{r},\boldsymbol{v})$ for species a and an additional source or sink term $S_a(\boldsymbol{r},\boldsymbol{v})$, the kinetic equation reads

$$\frac{\partial}{\partial t}f_a + \boldsymbol{v}\cdot\boldsymbol{\nabla}_r f_a + \frac{q_a}{m_a}\left(\boldsymbol{E}+\boldsymbol{v}\times\boldsymbol{B}\right)\cdot\boldsymbol{\nabla}_v f_a = \sum_b C_{ab}(f_a,f_b) + S_a(\boldsymbol{r},\boldsymbol{v}) \tag{4.5}$$

where C_{ab} is the Fokker-Planck collision operator for collisions between species a and b. The fluid equations for particle, momentum and energy conservation can be derived by multiplying this equation with moments of the velocity $\boldsymbol{v}$ (i.e., 1, $m\boldsymbol{v}$ and $\frac{1}{2}m\boldsymbol{v}^2$) and integrating over the velocity phase space.

From the zeroth order moment one obtains the particle conservation or continuity equation:

$$\frac{\partial n_a}{\partial t} + \boldsymbol{\nabla}\cdot\left(n_a\boldsymbol{u}_a\right) = S_a^n \tag{4.6}$$

with the particle density $n_a = \int f_a d\boldsymbol{v}$, the fluid velocity $\boldsymbol{u}_a = \frac{1}{n_a}\int \boldsymbol{v} f_a d\boldsymbol{v}$ and $S_a^n = \int S_a d\boldsymbol{v}$ describing particle sources or sinks (e.g., resulting from ionization or recombination reactions).

The momentum conservation equation is obtained from the first order moment of the kinetic equation ($m\boldsymbol{v}$):

$$m_a n_a\left[\frac{\partial \boldsymbol{u}_a}{\partial t} + \left(\boldsymbol{u}_a\cdot\boldsymbol{\nabla}\right)\boldsymbol{u}_a\right] - q_a n_a\left(\boldsymbol{E}+\boldsymbol{u}_a\times\boldsymbol{B}\right) + \boldsymbol{\nabla}p_a + \boldsymbol{\nabla}\cdot\Pi_a = \boldsymbol{F}_{\mathrm{fr},ab} + S_a^m \tag{4.7}$$

with the isotropic pressure $p_a = n_a T_a$, the anisotropic viscosity tensor Π_a, the friction force between two species $\boldsymbol{F}_{\mathrm{fr},ab} \propto (\boldsymbol{u}_a - \boldsymbol{u}_b)$ and a momentum source or sink S_a^m (e.g., from cold neutrals that contribute their momentum as ions after ionization). Another important momentum source or sink is the thermal force $F_{\mathrm{th}} \propto \boldsymbol{\nabla}T$, whereas the electrostatic force $F_{\mathrm{el}} \propto \boldsymbol{E}$, the pressure gradient force $F_{\mathrm{pr}} \propto \boldsymbol{\nabla}p$ and the friction force $\boldsymbol{F}_{\mathrm{fr},ab}$ already appear explicitly in equation (4.7). Under steady state conditions all forces acting on the particles must be balanced.

Finally, from the second order moment $\frac{1}{2}m\boldsymbol{v}^2$ the energy conservation equation is obtained:

$$\frac{\partial}{\partial t}\left[\frac{3}{2}p_a + \frac{m_a n_a}{2}\boldsymbol{u}_a^2\right] + \boldsymbol{\nabla}\cdot\left[\left(\frac{5}{2}p_a + \frac{m_a n_a}{2}\boldsymbol{u}_a^2\right)\boldsymbol{u}_a + \boldsymbol{q}_a + \boldsymbol{v}_a \otimes \Pi_a\right] = Q_{ab} + Q_{\text{ohm}} + S_a^e \tag{4.8}$$

with the heat flux $\boldsymbol{q}_a$, the collisional energy transfer Q_{ab} between species, the ohmic heating Q_{ohm} and the energy source term S_a^e (e.g., from ionization or recombination).

As each fluid equation of order k contains moments of higher order $k+1$, higher order moments have to be approximated to achieve a closure of the fluid equations. For the high collisionality limit the fluid equations are known as the Braginskii-Equations. In this case the closure of the fluid equations is achieved by a description of the parallel heat flux $q_\parallel$ of ions and electrons as Spitzer-Härm heat flux [143] with the heat conduction coefficients χ and κ:

$$q_{\parallel,a} = n_a \chi_{\parallel,a} \boldsymbol{\nabla} T_a = -\kappa_{\parallel,a} \boldsymbol{\nabla} T_a = -\kappa_{0,a} T_a^{5/2} \nabla T_a, \tag{4.9}$$

where $\kappa_{0,e} \simeq 2000\,\mathrm{Wm^{-1}eV^{-7/2}}$ for electrons and $\kappa_{0,i} \simeq 60\,\mathrm{Wm^{-1}eV^{-7/2}}$ for ions in a pure hydrogenic plasma [45].

With these equations, the parallel transport can be described. The exact equations used in B2.5 are modified Braginskii equations, i.e., they are extended by specific metric coefficients to account for the curvilinear orthogonal coordinate system. Additionally, the classical parallel transport coefficients (cf. equation (4.9)) are replaced by expressions by Balescu [144], which include a dependence on the local effective charge Z_{eff} [145]. A detailed description of the modified Braginskii equations implemented in B2.5 can be found in [129, 146]. In each internal iteration the code sequentially solves the momentum conservation equation, the continuity equation and the energy conservation equation for electrons, main ions and for all impurity ion species, in order to calculate the plasma background. Usually, for the ions this is done for each charge state separately. However, to reduce the number of equations that have to be solved, it is also possible to combine the treatment of several different charge states into a single set of equations. Consequently, with this so-called charge state bundling, only single plasma parameters are derived for the whole charge state bundle (e.g., a single combined density for all corresponding charge states).

It has to be noted, that the validity of the fluid description of the plasma is not always assured, as the fluid approach can only be applied if the distribution function is close to a Maxwellian [23]. For this purpose, the mean free path of the particles must be small compared to the characteristic scale size of the system, which is

determined by the parallel connection length or by gradient lengths of the plasma parameters. This requirement is only fulfilled if the plasma is sufficiently coupled via collisions. However, especially in the SOL and in the PFR, where the density can be low, this is not always the case, and for a correct treatment, sometimes a kinetic approach would be required [147–149]. However, it is usually considered to be sufficient to introduce kinetic corrections (i.e., flux limiters for the electron and ion heat flux and for the viscosity [129]) and special boundary conditions in such regions, to reasonably justify a fluid description of the whole plasma. In a direct comparison of a fully kinetic and a simple fluid model in a completely collisionless system, it was observed that the discrepancies of the different solutions are surprisingly small [45, 149].

4.2.3 Perpendicular Transport

In general, perpendicular transport (i.e., transport in y-direction in the SOLPS terminology) can be described by a convective-diffusive approach for the radial particle flux Γ_y:

$$\Gamma_y = -D\frac{\mathrm{d}n}{\mathrm{d}y} + v_y n, \tag{4.10}$$

with a diffusion coefficient D, particle density n and a convective radial velocity v_y. However, in practice, the convective part is often integrated into an effective diffusion coefficient D_{eff}, in order to obtain better numerical stability [57]. This yields a purely diffusive equation with the same radial particle flux

$$\Gamma_y = -D_{\mathrm{eff}}\frac{\mathrm{d}n}{\mathrm{d}y}. \tag{4.11}$$

The perpendicular transport deduced from experiments is observed to be several orders of magnitude larger than expected from collisional transport theory. Consequently, the major contribution of the perpendicular transport is of turbulent nature [45] and sometimes denoted as anomalous transport.

For the perpendicular electron and ion heat conduction $q_{y,e}$ and $q_{y,i}$ a similar formulation can be applied with the electron and ion heat diffusion coefficients χ_e and χ_i:

$$q_{y,e} = -n_{\mathrm{e}}\chi_e\frac{\mathrm{d}T_{\mathrm{e}}}{\mathrm{d}y} \tag{4.12}$$

$$q_{y,i} = -\sum_i n_i\chi_i\frac{\mathrm{d}T_i}{\mathrm{d}y}. \tag{4.13}$$

It should be noted, that in order to obtain the total heat flux, additional contributions of the convective energy transport attributed to the particle flux Γ_y have to be considered.

As the transport coefficients cannot be deduced from first principles so far, they are free parameters in the simulations and have to be specified by the user in a way that experimental profiles are reproduced. The transport coefficients can either be set to be constant in the whole computational domain, or radial profiles can be specified. This is especially important for simulations of H-mode plasmas, for which a radial transport barrier (i.e., a dip in the radial profiles of the transport coefficients) has to be implemented. Such a transport barrier produces the typical H-mode profiles for electron density and temperature with the increased pedestal and enhanced edge gradients.

Additionally, also poloidal asymmetries of the perpendicular transport are observed in the experiment. This so-called ballooning of transport is caused since the plasma is more MHD unstable on the LFS of the tokamak, resulting in increased perpendicular transport across the separatrix at the outboard midplane [142]. In SOLPS a simplified scheme to account for the poloidal variation of the perpendicular transport is implemented, which allows a rescaling of the transport coefficients in dependence of the local toroidal magnetic field B_t [129, 145]. The rescaling factor is calculated as $\alpha \cdot (B_\mathrm{avg}/B_\mathrm{t})^\beta$, where α and β are free parameters, and B_avg is the average of the total magnetic field strength over the entire computational domain.

Additional effects that have an influence on the radial transport of both energy and particles are, e.g., $E{\times}B$ and diamagnetic drifts, which are discussed below, blob filaments [150, 151] or ELMs [31, 152] (causing ELM flushing [153]). In the simulations ELMs can be emulated if the transport coefficients are strongly increased for a short period of time (i.e., for a few iterations). However, under steady state conditions, apart from drifts these additional transport mechanisms are not included in the SOLPS code and, therefore, cannot be considered in the simulations.

4.2.4 Drifts

An important contribution to both radial and poloidal transport are drifts. Drifts are a consequence of the gyro-motion of the charged particles in the magnetic field, in combination with external forces acting on the particles (e.g., due to an electric field, or a pressure gradient). In the fluid picture, the gyro-motion of the individual particles is reduced to an average motion of the guiding center. In this case, drifts can be expressed as drift velocities of the fluid, with the most important drifts being

the $E\times B$-drift and the diamagnetic drift:

$$\boldsymbol{E}\times\boldsymbol{B}-\text{drift}: \qquad v_{E\times B} = \frac{\boldsymbol{E}\times\boldsymbol{B}}{B^2} \tag{4.14}$$

$$\text{Diamagnetic drift}: \qquad v_{\text{dia}} = -\frac{\nabla p \times \boldsymbol{B}}{nqB^2}, \tag{4.15}$$

where $\boldsymbol{E}$ is the electric field, $\boldsymbol{B}$ is the magnetic field, p is the pressure, n is the density, and q is the particle charge. Drifts play a significant role and cannot be disregarded if a detailed match between experiment and simulation should be achieved. However, due to numerical instabilities, the activation of drift terms in SOLPS proves to be a difficult and protracted task. Problems can arise with the formulation of the transport equations and boundary conditions, and especially in high recycling regimes large radial gradients in the divertor region result in strong variations of the drift fluxes [57]. Therefore, due to their numerically challenging nature, drifts are not taken into account in this work. Nevertheless, the expected impact of drifts on the simulation results will be discussed later in section 6.7.3.

4.2.5 Boundary Conditions

At the boundaries of the computational domain (cf. figure 4.1), boundary conditions for the energy, momentum and continuity equation have to be specified for all particle species. Two different types of boundaries can be distinguished, as they can either be aligned to the magnetic field, or perpendicular to it. Therefore, the particle and heat flux to these boundaries can also be either due to parallel or perpendicular transport.

At the inner core boundary, which is aligned to the magnetic field, the particle and heat flux across the boundary into the computational domain has to be specified. This is done according to the sources within the core region, such as power sources from the plasma heating, or particle sources due to neutral beam injection. Alternatively, also a certain particle density or temperature can be specified. In this case, the code automatically tries to find the appropriate particle or heat flux across the particular boundary, via a feedback scheme, to achieve the requested density or temperature. If the simulations yield an inward particle flux across the core boundary into the core region, then usually an ionizing core option is applied, which means that all particles (ions and neutrals) are returned into the computational domain in a fully ionized state, to maintain particle balance.

At the outer boundaries, towards the main chamber wall, usually a density leakage option and a certain temperature decay length are specified. Usually, 100 % of the particles crossing the outer boundary due to perpendicular transport are recycled

as neutrals, although it is also possible to reduce the recycling coefficient to mimic wall pumping. The perpendicular energy flux towards the main chamber wall is partly absorbed, while 30 % (in the default setting) of the energy is carried back by the recycled neutrals.

At the divertor targets parallel fluxes have to be considered. In this case the appropriate sheath boundary condition [154] has to be applied, to fulfill the Bohm criterion $u \geq c_s$ [44], where $c_s = \sqrt{T/m}$ is the sound speed. For the particle fluxes, the target surfaces are typically also set to be fully recycling, providing strong neutral particle sources in the divertor regions. The energy recycling is by default again set to 30 % as for the outer boundary.

In practice, for each boundary various different boundary conditions are available, either with a specific purpose or functionality, or simply with slightly different implementations, resulting in different levels of physical correctness and numerical stability. For a complete description of all available boundary conditions, the reader is referred to [145]. Theoretically, the properties at the boundaries can be modified arbitrarily by the user, by applying different boundary conditions or modified particle and energy recycling coefficients. However, sometimes certain boundary conditions are not compatible with each other or with some configurations in the modeling setup, and therefore, the actual set of boundary conditions has to be chosen with care.

4.2.6 Modeling of Neutrals and EIRENE

For the treatment of neutrals, a simple neutral fluid model is implemented in B2.5. In this model the neutrals are treated in a similar way as the ions (i.e., as described above), but with their own particle and momentum transport equations, in which terms associated with charged particle motions or currents are disregarded. However, in many situations this model is not valid, especially in regions with low collisionality where the neutrals have a long mean free path [155]. Therefore, B2.5 alone is often insufficient to provide a satisfactory plasma solution. Hence, for the treatment of neutrals, B2.5 is usually coupled to the kinetic Monte Carlo code EIRENE. In this case, a rescaling factor (typically 10^{-10}) is applied to the B2.5 fluid neutral sources, to eliminate them and replace them by the sources and sinks calculated by EIRENE.

The Monte Carlo code EIRENE [139, 156, 157] is designed to solve multi-species systems of coupled Boltzmann-like kinetic equations. EIRENE can either be run in time-dependent or stationary mode on an arbitrary 3D geometry. Initially EIRENE was only developed as a standalone tool for investigations of neutral gas transport

in tokamak plasmas. However, due to its flexibility it is also used for a variety of different purposes, mostly within, but also outside of fusion research [156], whenever a linear kinetic transport model is required that is based on a stochastic approach, instead of numerical or analytical methods. However, it should be noted, that such a stochastic approach also leads to statistical noise in the results which is a drawback of the Monte Carlo method. A simplified picture of the working principle of EIRENE is presented here.

Using linear collision operators, EIRENE simulates test particle trajectories on a defined (fixed) background plasma solution. After determining the location of the next interaction of the test particle with the background plasma, or the next intersection with a material surface, the appropriate ion-neutral or neutral-surface interaction model is called, depending on the type of the interaction. According to the test particle species, the physical model and the availability of the corresponding atomic and molecular data or surface interaction databases, different processes can occur, e.g., elastic collisions, excitation, ionization, dissociation, charge exchange, surface reflection, absorption, etc. After the interaction, the particle trajectory is updated and the test particle continues until it is absorbed by a surface, converted, or until a specific time limit is reached which is defined for each test particle. If the particle is converted, e.g., by ionization, dissociation or charge exchange, the reaction products are considered as new test particles in EIRENE or as a particle source for the background plasma in the next iteration, depending on the type of the particles.

In practice, a statistically relevant amount of particles is launched from different so-called strata (typically in the order of 50.000 test particles per stratum). Each stratum corresponds to a specific origin of the neutral particle (i.e., gas puff, volume recombination or recycling from different locations) and to a specific test particle species, characterized by an appropriate set of possible interactions and rate coefficients. From the resulting bulk of simulated test particle trajectories and interactions, the sources and sinks for particles, momentum and energy are extracted and fed into the plasma equations.

For neutral particles, also their trajectories outside of the hot ionizing plasma have to be considered, as their distribution within the vessel is important for the plasma fueling. Therefore, the computational domain considered by EIRENE is not limited to the B2.5 grid presented in figure 4.1, but also includes the regions outside of the B2.5 grid within the plasma vessel. Consequently, the neutrals are able to reach remote locations, which allows to include pumping of neutral particles behind the outer divertor, according to the location of the pumping system in the experiment. For this purpose, absorbing surfaces can be defined in the simulation

at the respective pumping locations (see figure 4.1, left, blue surfaces), with an albedo corresponding to the pumping speed of the real pumps. Additionally, test surfaces can be implemented to determine the neutral particle flux at a certain position, mimicking the experimental neutral pressure gauges (see figure 4.1, left, red surfaces). In order to achieve an agreement of the neutral compression in the simulations with the experiment (i.e., the ratios of the neutral fluxes at different test surfaces or pressure gauges), the neutral conductance below the divertor region often has to be artificially reduced in the simulation by the implementation of additional surfaces (see figure 4.1, left, gray surfaces).

The atomic and molecular processes in EIRENE are described by external databases (e.g., AMJUEL [158], HYDHEL [159], METHANE [160]), from which the corresponding rate coefficients can be calculated according to the local plasma parameters. The different reactions can be classified in different reaction types.

Elastic collisions (or elastic scattering) are the most basic processes that can occur. In an elastic collision, two colliding particles change their direction of propagation, whereas the total momentum and kinetic energy are conserved. The type of the involved particles remains unchanged.

This is not the case in inelastic electron impact events, which can either result in excitation, ionization, or if molecules are involved also in dissociation of the particles. After an excitation process, the particle remains in an excited state for a short period of time and emits line radiation when it falls back into the ground state. If the particle is ionized, the neutral particle trajectory is stopped in EIRENE, providing an ion source for the fluid code. In a dissociation reaction a molecule is split into its individual components, which again means, that the particle trajectory is stopped, and the trajectories of the new particles are followed in EIRENE.

If a neutral particle collides with another charged atom, a charge exchange reaction can occur. In this case, a valence electron is exchanged from one particle to the other. This process also produces a typical excitation spectrum, again resulting in line radiation. Additionally, the charge exchange process can cause significant momentum loss and a reduction of the plasma pressure, if the neutralized particle which is not bound to the magnetic field anymore, but still carries lots of momentum (as it was a hot ion before), escapes from the plasma region.

Finally, radiative recombination or three-body recombination describe a process, in which an ion is neutralized by a collision with an electron or with two electrons in three-body recombination. This process becomes dominant only at low temperatures ($T_e \lesssim 1.5\,\mathrm{eV}$), and causes a sink of ions, energy and momentum. Recombination is an important process to reach divertor detachment.

A selection of different reactions that are implemented in EIRENE is presented in table 4.1 for the atomic species deuterium (D), helium (He), carbon (C), nitrogen (N) and argon (Ar) and the molecular species D_2 and N_2. In all of the cases, if one of the reaction products is an ion, the process provides a particle source for the fluid

Database	**Label**	**Type**	**Reaction**		
AMJUEL	H.4 2.1.5	EI	$D + e^-$	$\rightarrow$	$D^+ + 2e^-$
AMJUEL	H.1/3 3.1.8	CX	$D + D^+$	$\rightarrow$	$D^+ + D$
AMJUEL	H.4/10 2.1.8	RC	$D^+ + e^-$	$\rightarrow$	$D + h\nu$
AMJUEL	H.4 2.2.9	EI	$D_2 + e^-$	$\rightarrow$	$D_2^+ + 2e^-$
AMJUEL	H.4 2.2.5g	DS	$D_2 + e^-$	$\rightarrow$	$D + D + e^-$
AMJUEL	H.4 2.2.10	DS	$D_2 + e^-$	$\rightarrow$	$D + D^+ + 2e^-$
AMJUEL	H.2 3.2.3	CX	$D_2 + D^+$	$\rightarrow$	$D_2^+ + D$
AMJUEL	H.1/3 0.3T	EL	$D_2 + D^+$	$\rightarrow$	$D_2 + D^+$
AMJUEL	H.4 2.2.11	DS	$D_2^+ + e^-$	$\rightarrow$	$D^+ + D^+ + 2e^-$
AMJUEL	H.4 2.2.12	DS	$D_2^+ + e^-$	$\rightarrow$	$D + D^+ + e^-$
AMJUEL	H.4 2.2.14	DS	$D_2^+ + e^-$	$\rightarrow$	$D + D$
AMJUEL	H.4 2.3.9a	EI	$He + e^-$	$\rightarrow$	$He^+ + 2e^-$
AMJUEL	H.3 3.3.1	CX	$He + D^+$	$\rightarrow$	$He^+ + D$
AMJUEL	H.1/3 0.2T	EL	$He + D^+$	$\rightarrow$	$He + D^+$
AMJUEL	H.4 2.6A0	EI	$C + e^-$	$\rightarrow$	$C^+ + 2e^-$
METHANE	H.3 3.2	CX	$C + D^+$	$\rightarrow$	$C^+ + D$
AMJUEL	H.4 2.7A0	EI	$N + e^-$	$\rightarrow$	$N^+ + 2e^-$
AMJUEL	H.4/10 2.3.7A0	RC	$N^+ + e^-$	$\rightarrow$	$N + h\nu$
AMJUEL	H.2 2.7.5	DS	$N_2 + e^-$	$\rightarrow$	$N + N + e^-$
AMJUEL	H.2 2.18B0	EI	$Ar + e^-$	$\rightarrow$	$Ar^+ + 2e^-$
AMJUEL	H.4 2.3.18B0	RC	$Ar^+ + e^-$	$\rightarrow$	$Ar + h\nu$

Table 4.1: A selection of the atomic and molecular reactions implemented in EIRENE. According to the label, the reaction can be identified in the atomic database. The following reaction types are listed: elastic scattering (EL), electron impact ionization (EI), molecular dissociation (DS), charge exchange (CX) and recombination (RC), which for deuterium includes radiative and three-body recombination.

code, while for molecules and neutral atoms, the new particle trajectories are again followed by EIRENE.

4.2.7 Code Coupling

To combine the B2.5 fluid plasma description and the EIRENE Monte Carlo approach for the treatment of neutrals the codes have to be coupled. B2.5 and EIRENE interact via sink and source terms for particles, momentum and energy. The codes are executed iteratively, where one (external) iteration involves the following steps:

- B2.5 calculates a background plasma solution, for which a specified number of internal B2.5 iterations (typically around 10) is executed. The resulting plasma solution is then provided to EIRENE.
- On the basis of this background plasma solution, EIRENE simulates a set of test particle trajectories.
- From the simulated test particle trajectories, the sink and source terms for particles, momentum and energy are extracted and provided to B2.5.
- B2.5 recalculates the background plasma solution according to the new information, and provides the new resulting plasma solution to EIRENE, etc.

This procedure is then repeated for an appropriate number of iterations, until the case reaches convergence, i.e., until all relevant plasma parameters remain more or less unchanged – apart from the Monte Carlo noise introduced by EIRENE. As there are no generally agreed upon "correct" criteria for code convergence, a few basic possible convergence criteria which are also applied in this work are discussed in more detail below in section 4.2.9.

4.2.8 Operating the Code

After the computational grid (cf. section 4.2.1), and the required B2.5 and EIRENE input files have been generated, the SOLPS simulations can be initiated. For a detailed description of the numerous different input parameters which have to be specified, the reader is referred to the SOLPS 5.0 and EIRENE user manuals [145, 157]. Here only a few of the most basic parameters are mentioned.

As already stated above, the number of internal B2.5 iterations after which EIRENE is called to complete one external iteration is usually set to a small number in the order of 10. On the other hand, the number of total external iterations should be sufficiently large, e.g., in the order of 10.000, to allow the simulations to evolve.

During the run, the updated plasma parameters (or a subset of parameters to reduce the amount of data) are stored after each iteration. The evolution of a certain parameter during the run is usually called time trace. If the simulation parameters remain constant, i.e., if the time traces are flat, the simulation is possibly converged (see section 4.2.9 for further convergence criteria). Otherwise, if the simulation still evolves, it has to be continued until convergence is reached.

According to the Braginskii equations (4.6 – 4.8), in every iteration the evolution of the plasma parameters within a small time step ∂t is calculated. Therefore, it is important to define the size of the time step, i.e., the amount of time that elapses within a single iteration in the simulations. The size of the time step has to be specified by the user. With a larger time step the simulations evolve faster, and less iterations are required to reach a final state. However, with a too large time step, the changes of the parameters within a single iteration become too large, and the simulations become numerically unstable. Therefore, a compromise has to be found with a sufficiently large time step, which still provides numerically stable behavior. For ASDEX Upgrade simulations on a computational grid with 48 poloidal and 18 radial cells, and without drift terms activated, a time step in the order of 10^{-4} s or 10^{-5} s per iteration is a reasonable choice. It should be noted, that when drift terms are activated, the simulations become numerically much more unstable, and consequently the time step has to be reduced by at least a factor of 100.

From the operational point of view much more relevant is the actual run time of the simulations in CPU-time. The run time depends on various parameters, like the number of iterations, the resolution of the computational grid (i.e., the number of grid cells), the number of fluid species, the number of strata and test particles launched in EIRENE, as well as on the complexity of the included physics. In an average simulation including several different impurity species without charge state bundling (i.e., with a rather large number of fluid species), a computational grid with 48 poloidal and 18 radial cells, and without drifts, about one week of computational time (on a single CPU core) is required to complete a single run with 10.000 iterations.

Under these conditions, and with a time step of 10^{-4} s, convergence of a simulation can usually be achieved after a few runs, i.e., within a timescale in the order of several weeks, unless numerical instabilities are encountered. However, as stated above, when drift terms are activated, the time step usually has to be reduced to something between 10^{-6} s and 10^{-8} s, resulting in several years of total computational time for a single case to reach convergence (and additionally requiring lots of effort for the intense maintenance of such simulations). In [57], it is reported that experimentally validated SOLPS 5.0 drift simulations including seed impurities reached convergence

after a timescale of two years. Even though the numerical stability is considerably increased in the new SOLPS-ITER code version, it still takes several months to obtain a single converged drift simulation [125]. Therefore, creating a comprehensive dataset with various modifications of different input parameters and with full drifts activated in all simulations is unfeasible, and drifts are neglected in the simulations presented in this work.

Unfortunately, also without drifts, the operation of the code can sometimes be challenging due to numerical instabilities, oscillations, or other issues, and therefore, require lots of maintenance and much more time to reach convergence. However, as this is a rather technical aspect, the discussion of a few of the problems encountered during this work is restrained to appendix A.

4.2.9 Convergence Criteria

It is a crucial issue and the responsibility of the user to ensure that all simulations are properly converged. If this is not the case, the results and interpretations cannot be trusted [130]. However, there are no generally agreed upon criteria for code convergence, since such an assessment depends on various factors. With the countless variety of different possible modeling setups and different requirements for certain studies, the particular convergence criteria have to be judged individually according to the current situation. Therefore, unfortunately the assessment of convergence is somehow arbitrary and different approaches are used (e.g., [130, 161, 162]). Some possible basic convergence criteria, especially those applied in this work, are presented here.

To consider a simulation as converged, the plasma solution must approach steady state conditions in which all plasma parameters remain constant, apart from the Monte Carlo noise introduced by EIRENE. In practice, to determine if steady state conditions are reached for a certain parameter X, the time trace of the variable during the last run (i.e., its evolution during a sequence of N iterations) is considered. A linear trend line is fitted to the time trace, which yields the slope m_X of the trend line. Consequently, the variable X is only considered to be constant, if the total variation of the fit during the complete run, i.e., the slope multiplied by the total number of iterations $m_X N$ is small compared to the maximum variation of the data $\Delta X = max(X) - min(X)$:

$$m_X \cdot N \ll \Delta X. \tag{4.16}$$

As a convergence criterion an (arbitrary) user specified factor $c < 1$ can be introduced to guarantee a shallow slope:

$$m_X \cdot N \leq c \cdot \Delta X. \tag{4.17}$$

With this approach steady state conditions of certain parameters can be determined independently of the actual value of the variable. This would not be the case if, e.g., the relative standard deviation is considered, resulting in problems for variables which are close to zero.

Alternatively, also the characteristic time scale τ_X of a parameter X can be utilized, which can be deduced from the inverse slope m_X of the linear fit, as discussed in [162]. Steady state conditions are described by a value of τ_X which is larger than the longest characteristic time scale in the plasma – usually determined by the balance between gas puff and pumping, and typically in the order of 1 s [163].

In practice, the described convergence criterion requiring constant time traces should be applied to a selection of several different relevant parameters within the simulations. Such relevant parameters are, e.g., densities or particle fluxes in certain regions, the total amount of particles, or the total energy content.

Apart from constant time traces, another important indicator for convergence is the particle balance in the simulations. On the B2.5 side, the particle balance is simply determined by the particle fluxes across the boundaries of the computational domain and the particle sources and sinks within the grid. The B2.5 particle balance is usually well fulfilled.

If the code is coupled to EIRENE, then particle balance is usually considered as a balance between gas puff and pumping. To calculate the EIRENE particle balance, the particle influx Γ_{in} must be compared to the pumped flux Γ_{out} at the absorbing surfaces. The influx is determined by the gas puff and, if available, by additional sources, e.g., from fluxes according to certain boundary conditions, like the D^+ flux across the core boundary from the NBI source. For the pumped flux, also molecular contributions, e.g., from D_2 or N_2 have to be considered. Depending on the modeling setup, also the flux absorbed at the core boundary has to be included in Γ_{out}. With the ionizing core option this flux is returned (cf. section 4.2.5) and this contribution vanishes.

It is up to the user to specify which amount of discrepancy between particle influx and outflux is accepted to consider a simulation as converged. As a guideline one can consider the recycling fluxes at the boundaries of the computational domain, which should be significantly larger than the discrepancy of the particle balance.

It should be noted, that especially at low particle throughput, i.e., predominantly for impurities, large relative discrepancies between particle influx and outflux are observed, which is a known problem within the community. Unfortunately, no satisfactory solution could be provided for this issue so far. Therefore, using the

particle balance of impurities as convergence criterion can be problematic, while the particle balance of the main ions should normally be fulfilled in a converged case.

Similar to the influx and outflux of particles, in a converged case, also the total power leaving the system P_{out} should be equal to the input power P_{in}. Usually, the only contribution to the input power in the simulations is the specified power flux crossing the core boundary. For P_{out} all contributions of the power flux to the plasma facing components, as well as the radiated power P_{rad} have to be combined: $P_{\text{out}} = P_{\text{inner target}} + P_{\text{outer target}} + P_{\text{main chamber wall}} + P_{\text{PFR}} + P_{\text{rad}}$. The discrepancy between P_{in} and P_{out} should be small, however, as before, also here the level of confidence to consider a simulation as converged has to be specified by the user. According to experience, the energy balance is typically not a critical criterion, as it is well satisfied in most cases.

For an automatic identification of converged cases, post-processing routines can be implemented to check the convergence criteria described above, to monitor all finished simulations. However, experience shows that the convergence of each case should additionally be verified manually. Such a manual verification is necessary, as, e.g., the slope of the fit to the data can sometimes also be flat by accident, even though convergence is not achieved, e.g., if a value oscillates. Strictly speaking, the convergence should also be verified on different grid resolutions, to rule out that strongly localized effects (e.g., strongly peaked profiles) remain undetected due to a too coarse grid. However, such a procedure is often unfeasible in practice.

4.3 Current Status of SOLPS Modeling

As the SOLPS code package is widely used in the fusion community, various projects are dedicated to SOLPS modeling. In this section, a small selection of recent publications in which SOLPS is applied is presented to give a rough overview over the current status of SOLPS modeling, before the results of the numerical studies performed in this work are presented in the following chapters.

In [124] SOLPS 5.1 modeling is used to investigate the in-out asymmetry and detachment bifurcation [164] in an alternative divertor configuration – the so-called snowflake minus configuration – in the HL-2M tokamak. Constant transport coefficients were applied, and $E{\times}B$ drifts were activated, while diamagnetic drifts were disregarded due to numerical instabilities. A significant impact of the $E{\times}B$ drift on the in-out asymmetry was reported and the conditions under which a detachment bifurcation appears were identified.

A comparison of a standard divertor and X-divertor configuration in the DIII-D

tokamak has been performed in [126] using the SOLPS-ITER code package. It is shown that the X-divertor is able to boost the carbon line radiation, allowing similar detachment conditions as in the standard divertor with half the upstream density. The simulations were performed with spatially constant transport coefficients, without drifts, and coupled to EIRENE for the treatment of neutrals.

For TCV SOLPS-ITER modeling of the divertor upgrade has recently been conducted in [165] to study the expected effect of the planned gas baffle on the neutral particle distribution. The simulations without baffle agree well (i.e., within a factor of 2) with the experiment in terms of the gas puff required to match simulation and experimental data. With the new baffle, the simulations predict an increase of the neutral particle density in the divertor region by a factor of about 5 and an increased neutral compression by one order of magnitude. The simulations have been performed with spatially constant transport coefficients, coupled to EIRENE for the kinetic neutrals, and without drifts.

The formation of an electric potential well at the X-point is observed in SOLPS-ITER simulations for TCV in [166] under detached conditions. The simulations have been performed with spatially constant transport coefficients and activated drifts terms in reversed field configuration. The analysis reveals that the dominant contributions to the formation of the potential well are the diamagnetic and parallel currents. With the potential well, the particle flux patterns are observed to differ substantially from the classic drift pattern, with enhanced and reversed $E \times B$-flux. It is reported that the simulations are the first simulations for TCV with kinetic neutrals (i.e., coupled to EIRENE) and with full drifts activated, which has been facilitated by recent improvements of the numerical stability and speed enhancement methods within the SOLPS-ITER code package [163].

In [125] SOLPS-ITER simulations with full drifts activated are used to study a low-field side snowflake minus divertor configuration in ASDEX Upgrade. As in [166] it is reported that due to speed-up methods implemented in SOLPS-ITER (presented in [163]), and with a more complete treatment of drifts and currents (compared to SOLPS 5.0), it was possible to obtain converged drift simulations within a few months. Neutrals are treated by EIRENE, however, so far the simulations only cover a pure deuterium plasma without impurities and without radial transport barrier. The drifts result in a larger asymmetry between LFS and HFS, enhanced radial cross-field transport, and a redistribution of the flux between the primary and secondary strike points.

SOLPS-ITER modeling for the EAST tokamak was performed in upper single null, double null and lower single null configurations [167]. The simulations are coupled to EIRENE, and the transport coefficients have been modified to include an edge

transport barrier. Drifts have been activated, enhancing the divertor asymmetry and resulting in a better agreement between experiment and simulation.

An analysis of impurity seeded plasmas (comparing neon and nitrogen) in ASDEX Upgrade is presented in [55], where the importance of the ionization front and stagnation point position for the divertor impurity retention is discussed. For the analysis, SOLPS-ITER simulations of an ASDEX Upgrade H-mode plasma, including an edge transport barrier and with drifts activated have been performed. It is emphasized, that the drift terms have a great impact on the impurity transport.

Some predictive modeling for ITER is presented in [127]. To study the influence of the machine size on impurity seeded plasmas, SOLPS-ITER simulations based on ITER and ASDEX Upgrade geometries are compared. The simulations have been performed with neon and nitrogen seeding, drifts were fully activated, and an edge transport barrier was specified to obtain H-mode profiles. The force balance between thermal and friction force is studied and it is shown that drifts have a stronger impact in ASDEX Upgrade, compared to ITER. Additionally, less core radiation is observed in ITER, and it is concluded that both nitrogen and neon are acceptable impurity species for the usage in ITER.

In summary, it can be concluded that SOLPS-ITER has clearly become the preferred and most used version of the SOLPS code. The recent progress in code development and an improved numerical treatment of drifts resulted in more simulations with drift terms activated. Apart from the code version, it can be noted that many projects are currently dedicated to the investigation of alternative divertor configurations, for which numerical simulations are obviously a valuable tool.

In this work, the SOLPS 5.0 code package is used to investigate argon and nitrogen seeded H-mode plasmas in ASDEX Upgrade, without drift terms activated. An extensive dataset is generated, with elaborate impurity seeding scans, and a detailed analysis of the impurity transport and the divertor retention is conducted, which significantly extends previous investigations as provided, e.g., in [123] and in [55]. The modeling setup and the results of the numerical investigations are presented in the following chapters.

Chapter 5

Modeling Setup for the Numerical Plasma Simulations

In this section a brief overview over the ASDEX Upgrade discharge #29256, the discharge on which the simulations in this work are based, is given. Furthermore, the specific modeling setup and convergence criteria applied to the simulations performed in this work are described in detail.[1]

5.1 The ASDEX Upgrade Discharge #29256

The SOLPS 5.0 simulations presented here have been performed on the basis of a reference magnetic equilibrium, which was already used for impurity seeding studies previously [123]. The magnetic equilibrium was obtained from the ASDEX Upgrade H-mode discharge #29256, which was performed at a magnetic field of 2.5 T in forward field configuration (∇B-drift pointing down) and a plasma current of 1 MA. The discharge is similar to the discharges analyzed in section 3.3 which were performed after the modeling activities have been started. A total heating power of 14 MW was applied, and around 7 – 9 MW of radiation in the main plasma were determined by bolometric measurements. The deuterium fueling rate was around $2.4 \cdot 10^{22}\,\mathrm{es}^{-1}$ resulting in a line integrated core density in the order of $8 \cdot 10^{19}\,\mathrm{m}^{-3}$. An argon gas puff of roughly $0.5 \cdot 10^{21}\,\mathrm{es}^{-1}$ was active, and the shunt current measurement was around $T_{\mathrm{div}} \approx 10 - 15\,\mathrm{eV}$. Consequently, under the given experimental conditions, the outer divertor has to be considered as attached or on the transition to partial detachment, whereas the inner divertor was detached, according to Langmuir probe data [123].

[1] Part of this material was already published in [118].

5.2 The Basic Modeling Setup

Several simulation parameters have been varied within the scope of this thesis to investigate different phenomena. The "basic" modeling setup (for which the setup from [123] was used as a starting point) is presented in the following. Unless stated otherwise, the setup described in this section applies to all simulations performed in this work.

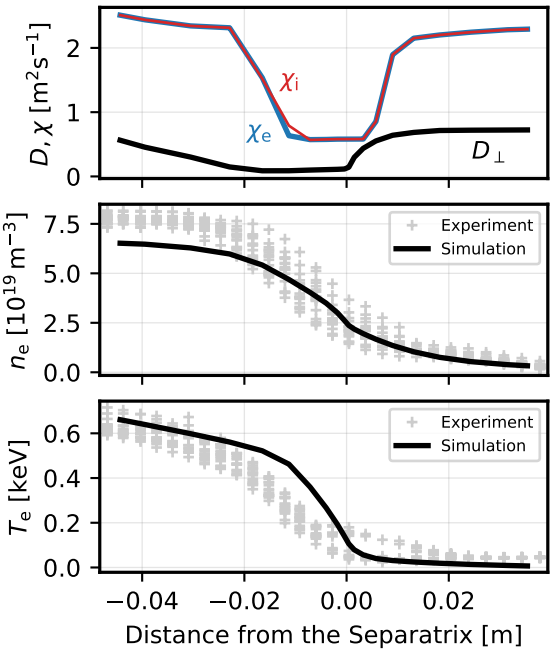

Figure 5.1: Transport coefficients for the SOLPS simulations (adapted from [123]) and the resulting upstream profiles of electron density and temperature from a single exemplary simulation. For comparison, also the experimentally measured profiles are displayed.

With the magnetic equilibrium of the experimental ASDEX Upgrade discharge #29256, a computational mesh with a grid resolution of 48 poloidal and 18 radial cells was created. The resulting grid is already displayed in figure 4.1. The deuterium fueling rate is feedback controlled in the simulations to maintain an electron density at the outer midplane separatrix of $n_{e,sep} = 2.5 \cdot 10^{19}\,\mathrm{m}^{-3}$, as measured in the experiment. According to the determined value of the core radiation and the heating power applied in the experiment, the input power (i.e., the power crossing the core boundary of the computational domain) is set to $P_{input} = 5\,\mathrm{MW}$, equally split between ions and electrons. At the divertor targets the Bohm-Chodura sheath boundary condition is enforced. To allow kinetic corrections if the system approaches low collisionality, electron and ion heat flux limiters and a viscous flux limiter with values of 0.3, 10 and 0.5 are applied, respectively (see [129] for a detailed description). The perpendicular electron and ion heat and particle transport coefficients χ_e, χ_i and $D_\perp$ have been adjusted in [123], including the H-mode transport barrier, to roughly reproduce the experimental profile shapes. They are shown in figure 5.1, together with the experimental and simulated upstream profiles of electron density and temperature. To account for a ballooning-like

asymmetry of the perpendicular transport, with an enhanced transport across the separatrix at the outboard side, a poloidal variation of the transport coefficients is implemented as discussed in section 4.2.3, with the parameters $\alpha = 0.834$ and $\beta = 1$. However, a detailed reproduction of the experimental profiles is not attempted here. To avoid an additional degree of freedom for the simulation parameters, the transport coefficients are kept fixed for all simulations presented in this work. With fixed upstream density, input power and transport coefficients, similar upstream parameters are obtained for all cases and, therefore, a reasonable comparability between different simulations is provided.

For the treatment of neutrals, all simulations are coupled to EIRENE (cf. section 4.2.6). As atomic species deuterium, helium, carbon, nitrogen and argon are included. On the B2.5 side this results in 39 individual species (5 neutral species plus 34 corresponding ion charge states). Charge state bundling is not applied. In addition to the atomic neutrals, the molecular species D_2, D_2^+ and N_2 are taken into account in EIRENE. As in the experiment, for the deuterium fueling a D_2 gas puff is located at the divertor roof baffle in the private flux region (PFR) and the impurity seeding positions are at the outer midplane for argon and in the PFR for N_2, at the same position as the D_2 puff (see figure 4.1). To investigate the impact of impurities on the plasma, different levels of argon and nitrogen seeding are applied in the simulations. Additionally, a D^+ flux across the core boundary of $10^{21}\,\mathrm{s}^{-1}$ is specified to account for the particle source from the neutral beam injection (NBI) in the experiment, and the C^{6+} density at the core boundary is fixed to $5 \cdot 10^{17}\,\mathrm{m}^{-3}$ to reproduce experimental values [123]. The implemented set of reactions is identical to the selection presented in table 4.1. A possible additional N_2 break-up chain, with N_2^+ as intermediate step, similar to the processes involving D_2^+ (cf. table 4.1), is not considered. The required reactions for such an additional N_2 break-up chain are not available in the atomic databases [158] used in this work. Technically, this leads to a mean free path of the N_2 molecules in the simulations that is too long, due to missing dissociation processes. However, also in the present simulations (i.e., with the incomplete set of dissociation reactions), the N_2 mean free path is typically only below 0.1 mm, and it is also reported in [57], where a simple N_2/N_2^+ molecule break-up model has been implemented, that such an additional mechanism does not have a significant influence on the plasma solution. Concerning the recycling, carbon is defined as a sticking species, where the recycling coefficient is set to 0, whereas the remaining species are fully recycling, with a recycling coefficient of 1. While this assumption of full recycling is well justified for the noble gas argon, it should be noted, that this is in general not the case for nitrogen. It can be expected, that with realistic nitrogen recycling (i.e., with wall pumping of up to 10 % of the

Basic modeling setup				
Impurity species	P_{in} [MW]	$n_{\text{e,sep}}$ [m^{-3}]	Imp. seeding [es^{-1}]	Cases
Ar scan	5	$2.5 \cdot 10^{19}$	$\leq 1.8 \cdot 10^{21}$	46
N scan	5	$2.5 \cdot 10^{19}$	$\leq 1.8 \cdot 10^{21}$	57
Mixed impurity seeding				
Mixing ratio	P_{in} [MW]	$n_{\text{e,sep}}$ [m^{-3}]	Imp. seeding [es^{-1}]	Cases
100 % Ar	5	$2.5 \cdot 10^{19}$	$\leq 1.8 \cdot 10^{21}$	46
66 % Ar	5	$2.5 \cdot 10^{19}$	$\leq 1.8 \cdot 10^{21}$	21
50 % Ar	5	$2.5 \cdot 10^{19}$	$\leq 1.8 \cdot 10^{21}$	30
33 % Ar	5	$2.5 \cdot 10^{19}$	$\leq 1.8 \cdot 10^{21}$	22
100 % N	5	$2.5 \cdot 10^{19}$	$\leq 1.8 \cdot 10^{21}$	57
Other mixing ratios	5	$2.5 \cdot 10^{19}$	$\leq 1.8 \cdot 10^{21}$	26
Feed-forward cases				
D fueling [es^{-1}]	P_{in} [MW]	$n_{\text{e,sep}}$ [m^{-3}]	Imp. seeding [es^{-1}]	Cases
$2 \cdot 10^{21}$	5	$1.7 - 2.9 \cdot 10^{19}$	$\leq 1.8 \cdot 10^{21}$	33
$3 \cdot 10^{21}$	5	$1.9 - 2.8 \cdot 10^{19}$	$\leq 1.8 \cdot 10^{21}$	27

Table 5.1: Summary of all SOLPS simulations conducted in this work. The list is continued in table 5.2.

impinging nitrogen flux [168]), higher nitrogen seeding levels would be required to obtain similar impurity concentrations and radiation fractions. Deuterium is recycled as molecular D_2, and all other species as atomic neutrals. Sputtering is not included in the simulations. Differences in the plasma-wall interaction between nitrogen and argon are not taken into account and hydrocarbon or ammonia production is disregarded. For the neutral pumping of deuterium atoms, impurities and molecules, pumping surfaces are implemented as shown in figure 4.1, left (blue surfaces behind the outer divertor), according to the locations of the turbopump and the cryopump in the experiment (cf. figure 3.2, right). To obtain a similar pumping speed as in the experiment, the albedo of the cryopump is set to 0.7 and the albedo of the turbopump to 0.993. Drifts are neglected in the simulations. However, the implications for the analysis due to the absence of drift terms and the expected impact of drifts on the simulation results, as well as other limitations of the code are discussed in more detail in section 6.7.

Regarding the numerical parameters discussed in section 4.2.8, the number of internal B2.5 iterations after which EIRENE is called to complete one external iteration is usually set to 10 in the present simulations. However, sometimes convergence of a

Power and density scan				
	P_{in} [MW]	$n_{\text{e,sep}}$ [m^{-3}]	Imp. seeding [es^{-1}]	Cases
Very low power	5	$1.5-4\cdot10^{19}$	$\leq 1.8\cdot10^{21}$	215
Low power	10	$2.5-4\cdot10^{19}$	$\leq 1.1\cdot10^{22}$	38
Medium power	15	$2.5-5\cdot10^{19}$	$\leq 1.4\cdot10^{22}$	42
High power	20	$2.5-5\cdot10^{19}$	$\leq 1.4\cdot10^{22}$	55
Very high power	25	$2.5-5\cdot10^{19}$	$\leq 1.4\cdot10^{22}$	59
Magnetic field scan			($B_{\text{t}} \in [1, 2, 2.5, 3, 4, 5, 6\,\text{T}]$)	
	P_{in} [MW]	$n_{\text{e,sep}}$ [m^{-3}]	Imp. seeding [es^{-1}]	Cases
Unseeded	5	$2.5\cdot10^{19}$	–	20
Ar seeding	5	$2.5\cdot10^{19}$	$1.1\cdot10^{21}$	13
N seeding	5	$2.5\cdot10^{19}$	$1.4\cdot10^{21}$	18
Mixed seeding	5	$2.5\cdot10^{19}$	$1.3\cdot10^{21}$	17
Other simulations				
	P_{in} [MW]	$n_{\text{e,sep}}$ [m^{-3}]	Imp. seeding [es^{-1}]	Cases
Rev. gas puff pos.	5	$2.5\cdot10^{19}$	$\leq 1.8\cdot10^{21}$	16
Tests & others	3.5 – 22	$2.3-4\cdot10^{19}$	$\leq 4.9\cdot10^{21}$	> 100
			Total number of cases:	**666**

Table 5.2: Summary of all SOLPS simulations conducted in this work. Continuation of table 5.1. Due to an overlap between some of the categories, the total number of cases is smaller than the sum of all cases in all individual datasets.

simulation could only be achieved if the number of internal iterations was adjusted and values between one and 25 internal iterations are applied. The number of total external iterations is always set to 10.000. For the size of the time step of a single iteration, values of 10^{-4} s and 10^{-5} s are applied in the basic modeling setup in this work.

5.3 Deviations from the Basic Modeling Setup

In a few simulations presented in this work, the modeling setup deviates from the basic modeling setup described above. Instead of a feedback mechanism on the separatrix density, in a few "feed-forward" simulations presented in section 6.2, a constant deuterium fueling (with different fueling levels) is applied. To study the importance of the impurity seeding gas puff location, the seeding positions of argon

and nitrogen are reversed in section 6.2. In section 6.6.1 simulations are performed with an increased separatrix density and input power, and finally, to investigate the impact of the magnetic field strength, the magnitude of the toroidal magnetic field is rescaled in section 6.6.3. Additionally, purely numerical parameters (like the number of internal iterations, the time step, etc.) are modified to investigate the sensitivity of the simulations on the numerical input parameters (see appendix A.3). Whenever the modeling setup deviates from the basic modeling setup, this is explicitly mentioned in the particular section.

A summary of all simulations which have been performed for this thesis and an overview over the applied modeling parameters is provided in tables 5.1 and 5.2. As some of the simulations have been performed for testing purposes and consistency checks, not all of the listed simulations are displayed in the analysis in chapter 6.

5.4 Convergence Criteria Applied to the Simulations

To ensure the proper convergence of the simulations with constant time traces, the slope m_X of a linear fit to the time trace of a certain parameter X is considered, as described in section 4.2.9. The user specified factor c from equation (4.17) is chosen

SOLPS notation	Description of the parameter
nesepm	Electron density at the outer midplane separatrix ($n_{e,sep}$)
tesepm / tisepm	Electron / ion temperature at the outer midplane separatrix
tmne	Total number of particles
tmte / tmti	Total energy content in the plasma of electrons / ions
nemxap / nemxip	Maximum electron density at the outer / inner target
temxap / temxip	Maximum electron temperature at the outer / inner target
timxap / timxip	Maximum ion temperature at the outer / inner target
fnixap / fnixip	Total particle flux to the outer / inner target
fetxap / fetxip	Total energy flux to the outer / inner target
fchxap / fchxip	Total current to the outer / inner target

Table 5.3: Summary of the SOLPS parameters that are required to be constant in order to consider the simulations as converged.

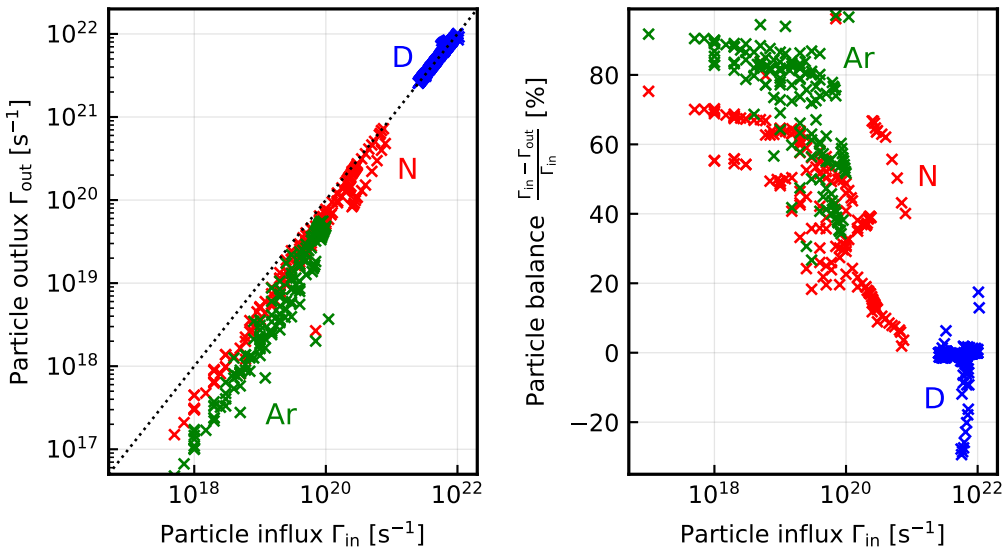

Figure 5.2: Comparison of particle influx and outflux in the simulations, to investigate the particle balance for deuterium, nitrogen and argon. A clear discrepancy between influx and outflux can be observed, especially at low particle throughput.

to be 0.2 in this work to guarantee a shallow slope:

$$m_X \cdot N \leq 0.2\,\Delta X \tag{5.1}$$

$$\xrightarrow{N=10^4} \quad m_X \leq 2 \cdot 10^{-5}\,\Delta X. \tag{5.2}$$

This convergence criterion is applied to several different parameters, as summarized in table 5.3. Additionally, in the feedback cases, it is also required that the deviation of $n_{e,sep}$ from the desired target value is smaller than 1.5 %, and the relative variation of $n_{e,sep}$ during the last run is limited to be smaller than 6.5 % to reject cases with extreme fluctuations, e.g., due to strong Monte Carlo noise.

Considering the particle balance, the relative discrepancy between particle influx Γ_{in} and outflux Γ_{out} for deuterium is observed to be below 5 % in the majority of the simulations, and cases are rejected if the discrepancy exceeds 30 %. For the impurities, a satisfying particle balance could often not be achieved due to the low particle throughput, as it can be seen in figure 5.2, where the particle outflux and the relative discrepancy between influx and outflux are plotted against the particle influx. However, it should be noted, that compared to the recycling flux $\Gamma_{recyc.}$, the discrepancy between particle influx and outflux (i.e., $|\Gamma_{in} - \Gamma_{out}|/\Gamma_{recyc.}$),

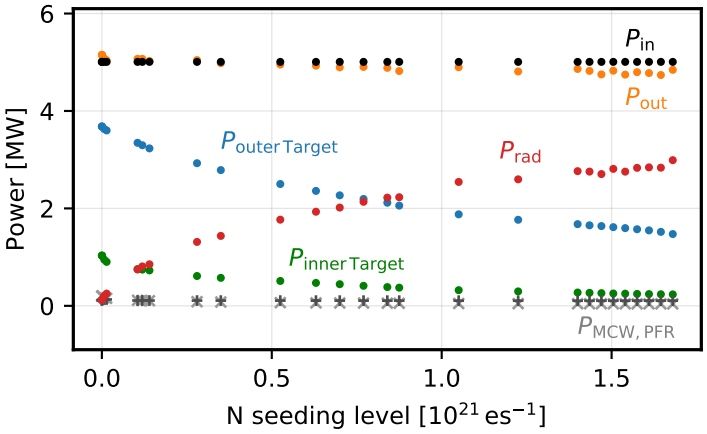

Figure 5.3: The input power P_{in}, P_{out}, and the different contributions to the power balance plotted against the impurity seeding level in the basic modeling setup for the simulations with nitrogen seeding.

is always below 2 % for impurities, even at lowest throughput, and below 0.2 % for deuterium. Therefore, the discrepancy of the particle balance is not expected to have any significant impact on the particle sources in the plasma.

An evaluation of the power balance reveals that the discrepancy between the input power P_{in} and the power leaving the system P_{out} almost always stays well below 10 %, and only approaches this limit in a few cases with very high radiation fractions. The good agreement between P_{in} and P_{out} can also be seen in figure 5.3, where P_{in}, P_{out}, and all contributions of the power flux to the plasma facing components (i.e., to the outer target, to the inner target, to the main chamber wall, MCW, and to the PFR), as well as the radiated power P_{rad} are plotted against the impurity seeding level in the nitrogen seeding scan.

Chapter 6

Numerical Investigation of Argon and Nitrogen Impurity Seeding

This chapter focuses on the interpretative studies and numerical simulations of argon and nitrogen seeded plasmas which were performed using the SOLPS 5.0 code package. The observations that have been made in the simulations are described, the results of the different investigations are presented, and an interpretation and discussion of the results is provided at the end of the chapter.[1]

6.1 Motivation and Outline

The numerical simulations conducted in this work are motivated by the experimental observations discussed in chapter 3. The simulations aim to improve the understanding of the impact of different impurity species on the divertor and plasma performance, and to provide a guidance for future experiments investigating mixed impurity seeding. Previous numerical investigations, as presented in [123], are significantly extended. While in [123] pure argon seeding is investigated, in this work for the first time also mixed impurity seeding in ASDEX Upgrade with simultaneous argon and nitrogen seeding is studied via SOLPS 5.0 simulations. The previous studies mainly focused on the redistribution of the impurity density according to the parallel force balance along field lines in the SOL. In this work, it is additionally found that the impurities have a strong impact on the main ion plasma flows. The resulting feedback on the impurity flow pattern and on the impurity density distribution is self-consistently taken into account and analyzed. Regarding the divertor impurity retention, the general discussion in [55] is extended by a detailed analysis of the impact of impurity seeding on the impurity stagnation point position, which (together with the neutral impurity ionization front position) determines the divertor retention.

[1] Part of this material was already published in [118].

The simulations are based on the ASDEX Upgrade discharge #29256 (see section 5.1) and the modeling setup was already presented in section 5.2. In this chapter systematic argon an nitrogen seeding scans are carried out in section 6.2, and distinctive differences between the different impurity species are emphasized. According to the divertor conditions, the simulations which yield the closest match to the experimental discharge #29256 are obtained at argon seeding levels above $\Gamma_{\mathrm{Ar}} \approx 1.5 \cdot 10^{21}\,\mathrm{es}^{-1}$. An investigation of mixed impurities with simultaneous argon and nitrogen seeding is presented in section 6.3. A detailed analysis of the impurity transport and of the divertor impurity retention is provided in sections 6.4 and 6.5. To extend the analysis to a wider parameter space, simulations with increased input power, separatrix electron density, and modified toroidal magnetic field strength are presented in section 6.6. Finally, a discussion of the results, including an assessment of the expected impact of drifts – which are not included in the present simulations – is provided in section 6.7.

6.2 Impact of Argon and Nitrogen Impurity Seeding on the Plasma Parameters

To investigate the impact of impurities on the plasma, different levels of argon and nitrogen seeding are applied. In this section only pure argon and pure nitrogen seeding is investigated, while simultaneous injection of both argon and nitrogen will be considered in section 6.3. The seeding levels are given in electron equivalent units, i.e., $\Gamma_{\mathrm{Ar,e}} = 18\,\Gamma_{\mathrm{Ar,atoms}}$ and $\Gamma_{\mathrm{N,e}} = 7\,\Gamma_{\mathrm{N,atoms}} = 14\,\Gamma_{\mathrm{N_2,molecules}}$. Seeding levels of up to $1.8 \cdot 10^{21}\,\mathrm{es}^{-1}$ are achieved, whereas higher seeding levels result in high radiation fractions $P_{\mathrm{rad}}/P_{\mathrm{input}}$ of $\gtrsim 60\,\%$ at which the simulations become increasingly unstable.

An overview over the upstream and target profiles of electron density and temperature, as well as the inner and outer target power loads are shown in figures 6.1 and 6.2 for the simulations with argon and nitrogen seeding, respectively. The applied impurity seeding level is indicated by the color coding. As it can be seen, the impurities have a strong impact on the profiles. A detailed analysis of the impact of the impurities on the plasma is presented in the following.

6.2.1 Impurity Density Distribution

Figure 6.3 shows the impurity densities (left) and the corresponding impurity concentrations (right) in different regions plotted against the impurity seeding level for nitrogen (top) and argon (bottom). The displayed values are averaged over the

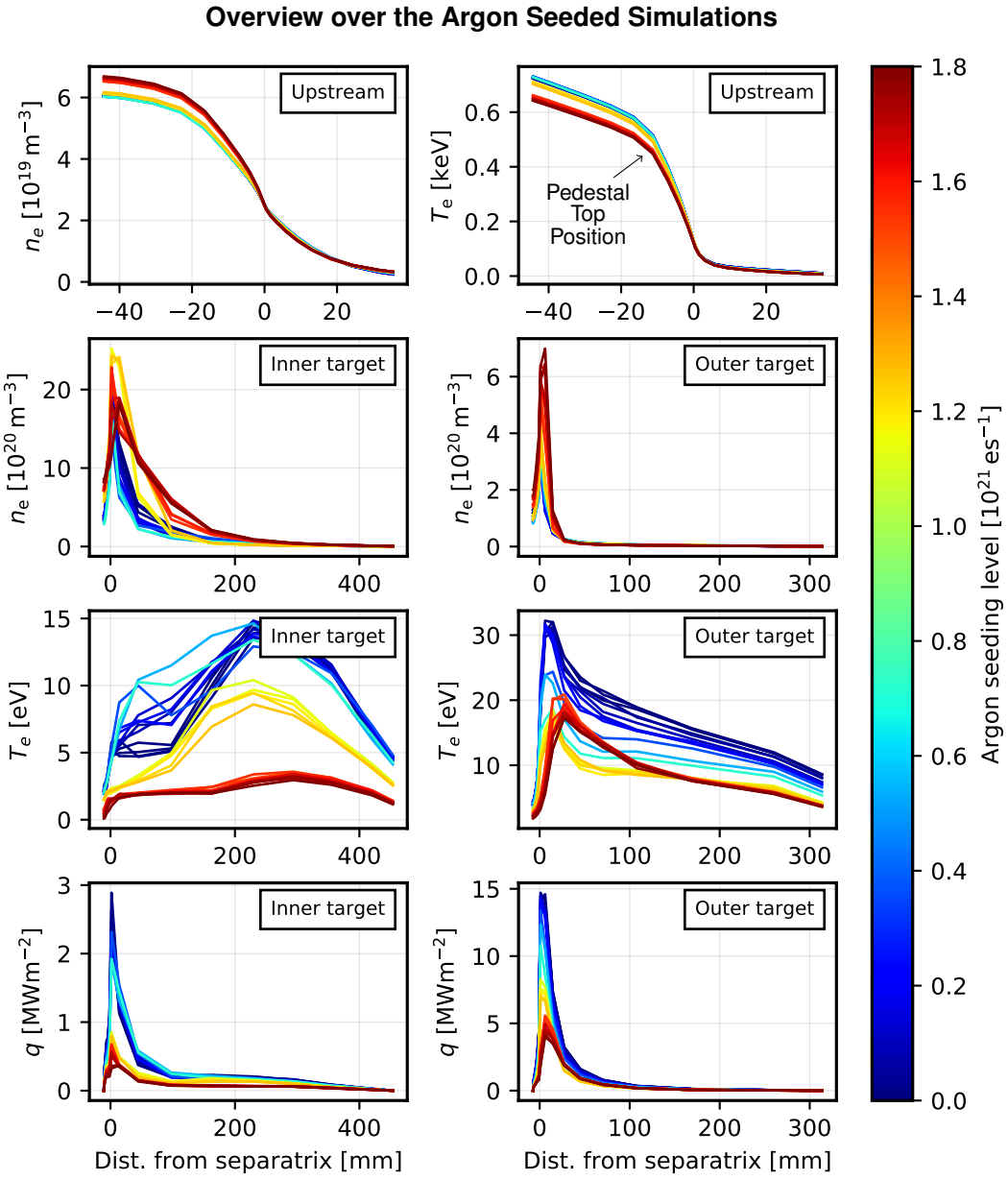

Figure 6.1: Overview over the upstream and target profiles of electron density and temperature and the perpendicular target power loads for the argon seeded simulations in the basic modeling setup. The evolution of the profile shapes with increasing argon seeding level can be deduced from the color coding.

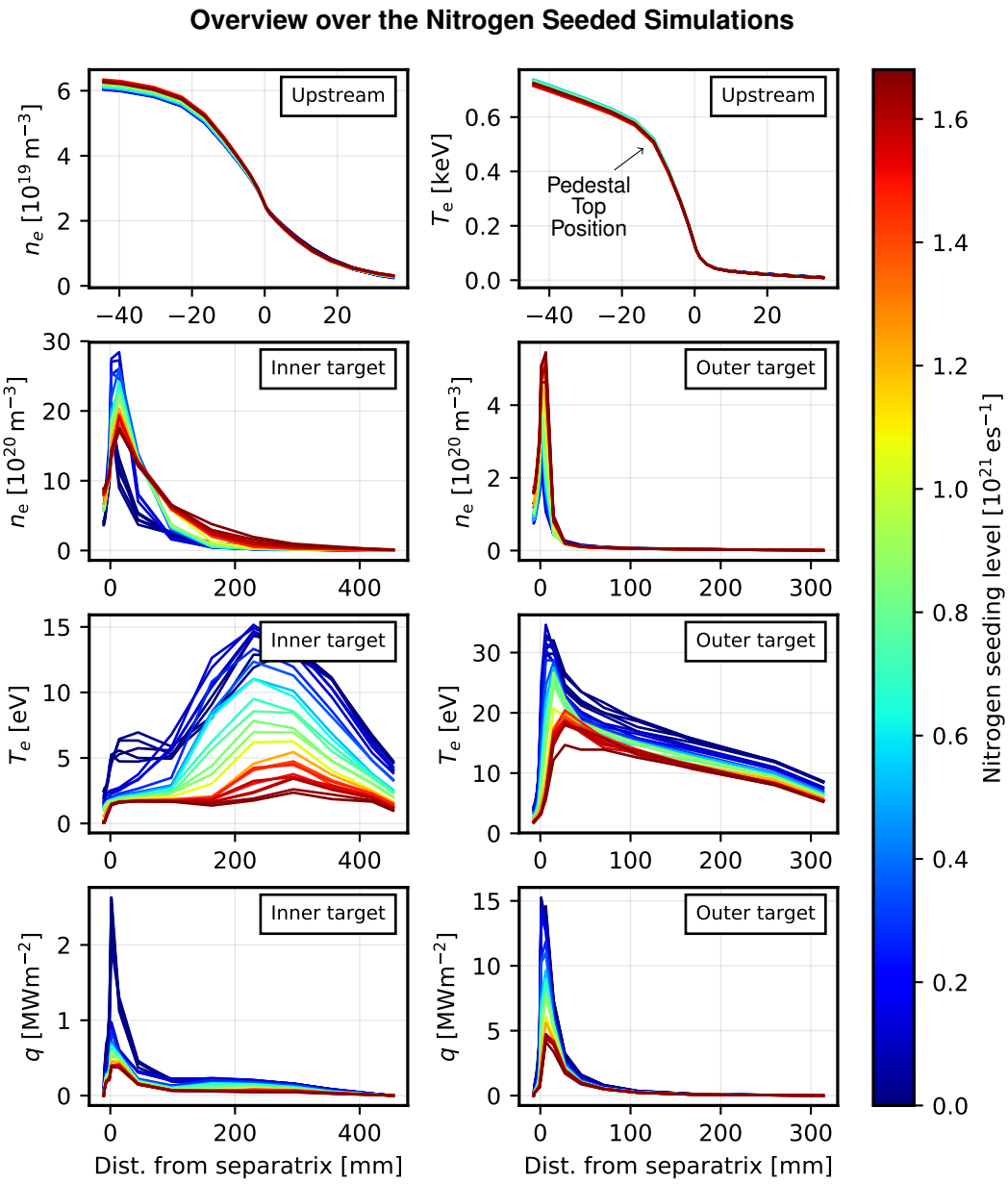

Figure 6.2: Overview over the upstream and target profiles, i.e., the same as figure 6.1, but with nitrogen seeding. The evolution of the profile shapes with increasing nitrogen seeding level can be deduced from the color coding.

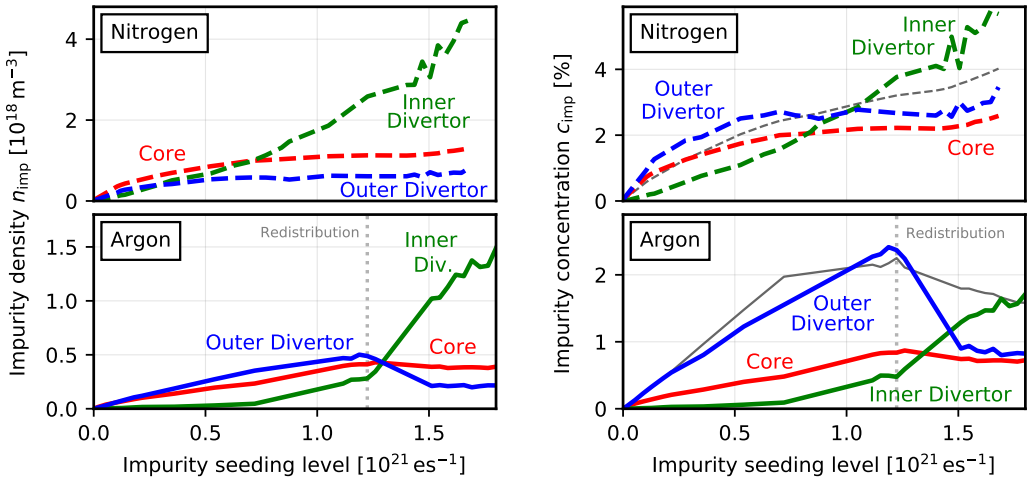

Figure 6.3: Impurity densities n_{imp} (left) and concentrations c_{imp} (right) for the nitrogen seeding scan (top) and the argon seeding scan (bottom) in different regions. Additionally, the ratio of the impurity seeding to the deuterium fueling rate $\frac{\Gamma_{\text{imp}}}{\Gamma_{D^+}+\Gamma_{\text{imp}}}$ is shown (gray lines), which is often used in the experiment to estimate the impurity concentration. Seeding levels are given in electron equivalent units. The core region only denotes the part covered by the computational domain ($0.9 \lesssim \rho_{pol} < 1$) and the divertor regions do not include the private flux region. The vertical dotted lines (here and in the following plots) indicate where the argon impurity density redistribution happens.

computational grid cells within the particular region. Initially, the impurity densities and concentrations steadily increase in all regions with increasing seeding level. However, at high seeding levels in the argon seeding scan the argon density in the outer divertor decreases. At this point, i.e., above a seeding level of $1.22 \cdot 10^{21}$ es^{-1} (dotted vertical lines), argon impurities are shifted from the outer to the inner divertor. In the following this modification of the impurity density distribution will be referred to as "density redistribution", even though it does not describe an actual time dependent redistribution process, but a transition between two different steady-state solutions. The causes for this argon density redistribution are investigated throughout the following sections, particularly in sections 6.4 and 6.5. Above the density redistribution, the argon core density saturates or even begins to decrease slightly, while the argon core radiation (cf. figure 6.4, right) continues to increase until the seeding level cannot be increased any further.

In addition to the impurity concentrations, the ratio of the impurity seeding level

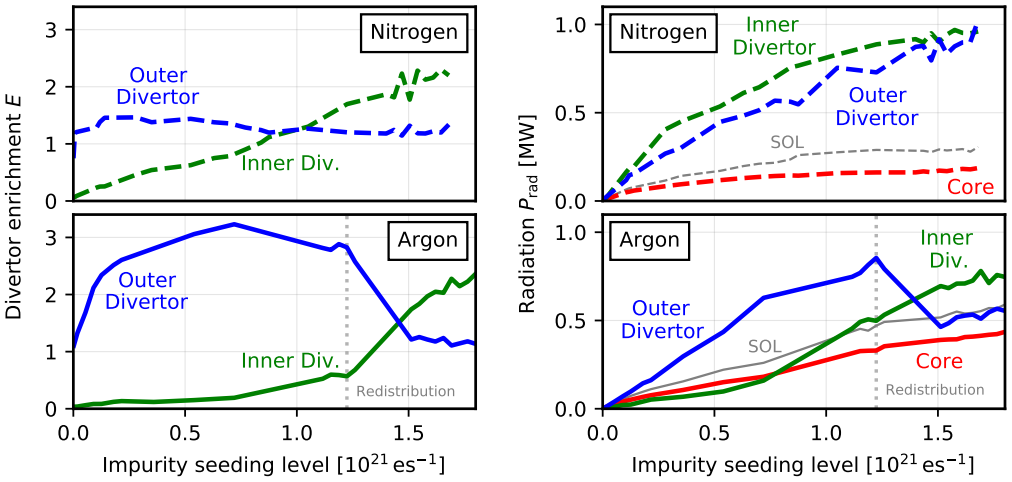

Figure 6.4: Left: Inner and outer divertor enrichment $E = c_{\mathrm{imp,div}} / c_{\mathrm{imp,core}}$ for nitrogen (top) and argon (bottom). Right: Impurity line radiation P_{rad} in different regions.

(in atoms per second) to the deuterium fueling level $\frac{\Gamma_{\mathrm{imp}}}{\Gamma_{\mathrm{D}^+} + \Gamma_{\mathrm{imp}}}$ is shown in figure 6.3, right (gray lines). In the experiment, this ratio is often used to estimate the impurity concentration in the divertor region, as a direct measurement is often not possible due to strong variations of the plasma parameters along the viewing lines of the diagnostics and insufficient quality of the atomic data for spectroscopy [102]. For the present simulations this estimate agrees reasonably well with the actual divertor impurity concentrations. However, the estimate cannot differentiate between the inner and outer divertor. Depending on the actual density distribution, it may yield an intermediate value.

6.2.2 Divertor Enrichment

Figure 6.4 (left) shows the inner and outer divertor enrichment $E = c_{\mathrm{imp,div}} / c_{\mathrm{imp,core}}$, which can be used to assess the impurity retention in the divertor region (cf. section 2.2.3). At seeding levels below $1.22 \cdot 10^{21}\,\mathrm{es}^{-1}$ argon is highly enriched in the outer divertor, while at higher seeding levels, the density redistribution (cf. section 6.2.1) results in a strongly reduced argon enrichment in the outer divertor and an increased enrichment in the inner divertor. A comparable behavior in the nitrogen seeding scan is also visible in figures 6.3 (right) and 6.4 (left), where the nitrogen concentration in the inner divertor exceeds that in the outer divertor above a seeding level of $0.9 \cdot 10^{21}\,\mathrm{es}^{-1}$. However, the effect is much less pronounced for

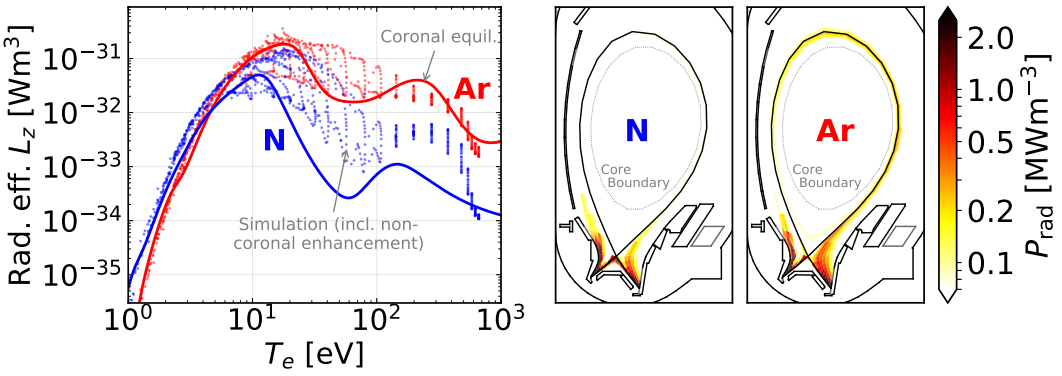

Figure 6.5: Left: Effective radiation efficiencies in the SOLPS simulations obtained as $L_z = P_{\mathrm{rad},z}/(n_e \cdot n_z)$. For comparison the solid lines show the values in coronal equilibrium at $n_e = 10^{19}$ m^{-3} according to the ADAS database [46]. Right: Argon and nitrogen radiation distribution. The data for all plots is obtained from an exemplary simulation with roughly similar total argon and nitrogen radiation, with an argon and nitrogen impurity seeding level of $\Gamma_{\mathrm{Ar}} = 1.0 \cdot 10^{21}$ es^{-1} and $\Gamma_{\mathrm{N}} = 0.8 \cdot 10^{21}$ es^{-1}.

nitrogen. To understand this behavior and the difference between nitrogen and argon we investigate the impurity transport and the divertor impurity retention in more detail in sections 6.4 and 6.5.

6.2.3 Impurity Radiation

In figure 6.4 (right), the power radiated by the impurities in different regions is shown. The argon core radiation exceeds the nitrogen core radiation by a factor of 2, even though the argon density in the core is by a factor of 3 lower compared to the nitrogen density. This high and continuously increasing argon core radiation can be explained by the temperature dependence of the radiation efficiency L_z (cf. section 2.2.3). The radiation efficiency and the differences in the impurity density distribution also explain the asymmetric distribution of the argon impurity radiation between the (colder) inner and (hotter) outer divertor, whereas the asymmetry reverses with the argon density redistribution. Contrary, with nitrogen seeding the impurity radiation is distributed much more symmetrically between inner and outer divertor. The total radiated power summed over the whole computational domain is roughly the same for argon and nitrogen at similar (electron equivalent) impurity seeding levels. For an exemplary simulation with roughly similar total argon and nitrogen radiation, the radiation distribution in the poloidal cross-section is plotted

separately for argon and nitrogen in figure 6.5 (right), which also reveals a stronger argon radiation in the core and SOL regions.

The argon and nitrogen radiation efficiencies in coronal equilibrium, as well as the effective radiation efficiencies obtained in the simulations, including the non-coronal enhancement, are shown in figure 6.5 (left). For a representative simulation at medium argon and nitrogen seeding level, every data point in the figure represents a single computational cell in the grid. This results in the discrete temperature values of the data points at $T_e \gtrsim 10^2$ eV, which originate from closed flux surfaces, while the data with $T_e \lesssim 10^2$ eV is from open flux surfaces. The values in figure 6.5 correspond to a non-equilibrium parameter (cf. section 2.2.3) in the order of $n_e\tau \approx 10^{20}-10^{21}$ m^{-3}ms, or to a characteristic residence time around $\tau \approx 1-10$ ms, which is in agreement with typical values proposed in the literature (see, e.g., [41]).

6.2.4 Electron Density, Electron Temperature and Target Peak Power Loads

While the electron density at the upstream separatrix position is kept fixed (see section 5.2), the average electron density in the core slightly increases at higher seeding levels, as it is shown in figure 6.6. Only in the inner divertor, the impurity seeding has a considerable impact on the electron density. This is due to a modification of the particle flow pattern in the SOL at high seeding levels, which is investigated and discussed in more detail in section 6.4.

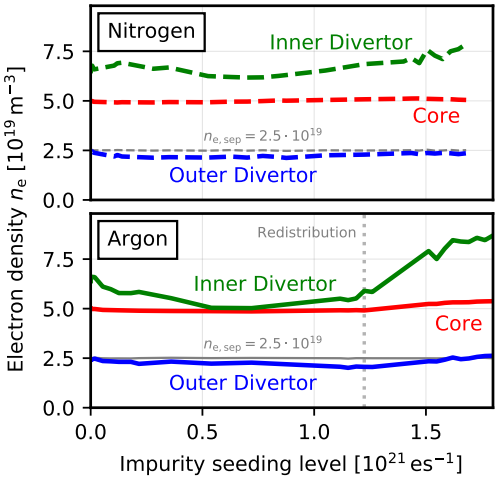

Figure 6.6: Evolution of the average electron density in different regions in the nitrogen (top) and argon (bottom) seeding scan.

The electron temperature in different plasma regions and the maximum inner and outer divertor target power loads are shown in figure 6.7. As expected, the radiative power dissipation leads to a reduction of the temperatures and power loads in all regions. With argon seeding, the strong pedestal top temperature drop of $\Delta T \approx 12\,\%$ compared to the unseeded reference case, caused by the increased argon core radiation, reveals a detrimental impact on the confined plasma. In comparison, such a strong impact on

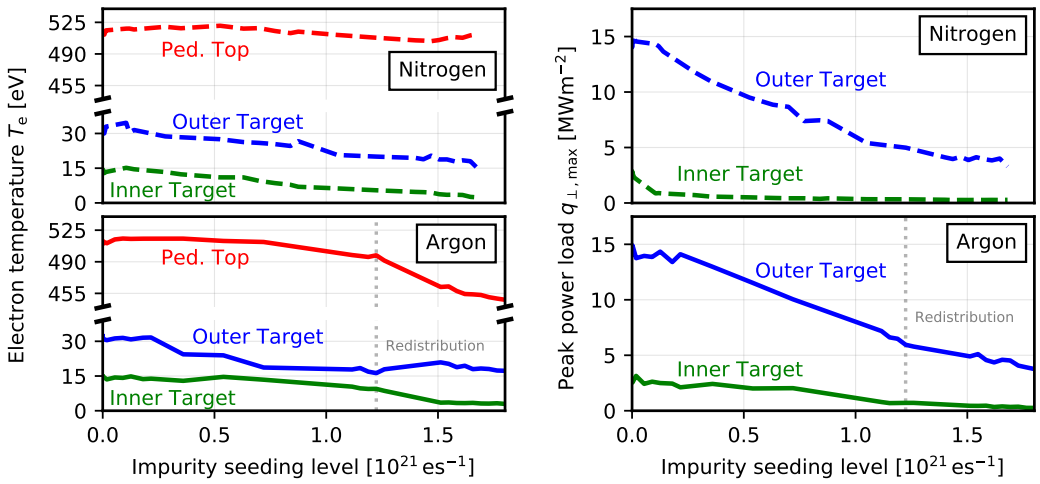

Figure 6.7: Electron temperature T_e in different regions (left) and maximum inner and outer divertor target power loads $q_{\perp,\max}$ (right) for nitrogen (top) and argon (bottom). The target values (green, blue) are the peak values at the particular divertor target and the core value (red) is the average over the closed flux surface at the pedestal top position, i.e., at $\rho_{pol} \approx 0.96$.

the pedestal top temperature is not observed for nitrogen ($\Delta T \lesssim 2\,\%$) at comparable target conditions (i.e., at similar peak power loads and target temperatures).

6.2.5 Impact of the Separatrix Density Feedback Mechanism and the Seeding Location

In all of the simulations presented above, the deuterium fueling rate was feedback controlled to sustain an upstream separatrix electron density of $n_{e,sep} = 2.5 \cdot 10^{19}\,\mathrm{m}^{-3}$, as described in section 5.2. As it can be seen in figure 6.8 (left), showing the averaged deuterium fueling rate in the argon seeding scan, at high seeding levels the deuterium fueling has to be increased considerably (by a factor of 3) to meet this target. This can be understood if one considers that with the power dissipation caused by the impurities, the reaction rate for the ionization of the deuterium atoms is reduced [169]. This results in a lower main particle source in the plasma and in increased neutral pumping, which has to be compensated by increased fueling. Consequently, if instead of the electron density the deuterium fueling rate is kept at a fixed value (colored lines in figure 6.8), the upstream separatrix electron density varies considerably (by more than 40 %, see figure 6.8, right). At higher seeding levels the electron density in the feed-forward

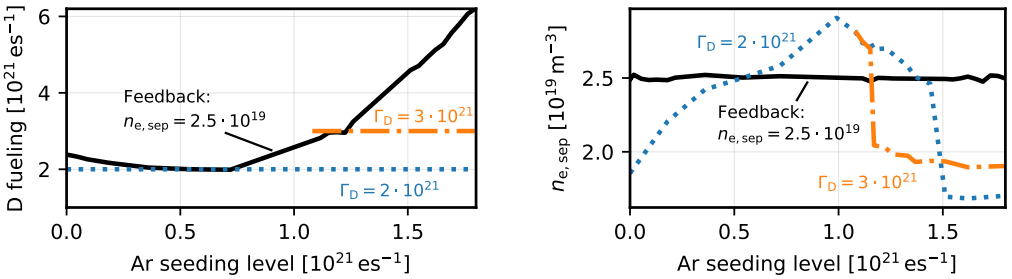

Figure 6.8: Left: Required deuterium fueling rate to sustain an electron density at the outer midplane separatrix of $n_{e,sep} = 2.5 \cdot 10^{19}$ m^{-3} in the argon seeding scan (solid black line). For a comparison two additional argon seeding scans with constant deuterium fueling rates of $\Gamma_D = 2 \cdot 10^{21}$ es^{-1} and $3 \cdot 10^{21}$ es^{-1} have been performed (colored lines). Right: The corresponding electron density at the outer midplane separatrix.

cases strongly decreases. This also leads to strongly increased temperatures in most regions, which makes a comparison of the different cases difficult. Nevertheless, the impurity density distributions and the divertor enrichment in the feed-forward cases (see figure 6.9) show the same qualitative behavior as in the feedback cases, with a clear argon density redistribution at high seeding levels. Therefore, the variation of the deuterium fueling rate itself cannot be the cause for the impurity density redistribution in the feedback cases.

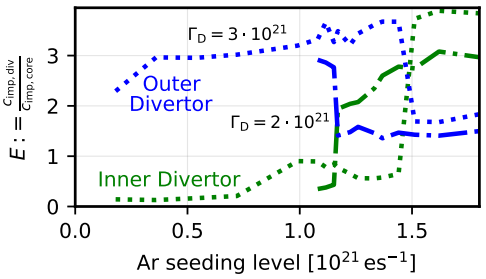

Figure 6.9: Inner and outer divertor enrichment plotted for the argon seeding scans with constant deuterium fueling rates ($\Gamma_D = 2 \cdot 10^{21}$ es^{-1} and $3 \cdot 10^{21}$ es^{-1}). The same qualitative behavior as in the feedback cases with the argon density redistribution can be observed (cf. figure 6.4, bottom left).

Also the location of the impurity seeding position does not have a significant impact on the simulation results under the investigated steady state conditions. The standard seeding positions for argon and nitrogen are indicated in figure 4.1. However, similar results (including the argon density redistribution) are obtained in simulations in which the impurity gas puff positions are reversed, i.e., nitrogen is

injected from the midplane and argon from the PFR. Considering the particle sources in the plasma, this weak impact of the seeding location on the plasma parameters is not surprising. While the impurity gas puff is in the order of $10^{20}\,\mathrm{s}^{-1}$ (in atomic flux), the total recycling rate of the impurities at the walls, mainly at the divertor targets, is usually in the order of $10^{22}\,\mathrm{s}^{-1}$ or even higher. Therefore, recycling is by far the strongest particle source in the plasma, whereas the gas puff and its position are mostly irrelevant. However, it should be noted, that in the nitrogen seeding cases this situation might change if a more realistic surface model is applied, instead of the assumption of full recycling.

In summary, the basic argon and nitrogen seeding scans show a similar behavior as it is observed in the experiment, and as it is expected according to the radiation efficiency. Nitrogen predominantly radiates in the divertor region, while argon also shows considerable radiation in the main chamber SOL and core region. Consequently, argon seeding results in a stronger pedestal top temperature drop, compared to nitrogen seeding. An interesting observation in the simulations is the high argon enrichment in the outer divertor at moderate seeding levels, which drops significantly at higher seeding levels, due to a redistribution of the argon impurities from the outer to the inner divertor. An interpretation of the argon density redistribution is provided in section 6.4 and 6.5, where the impurity transport and the divertor impurity retention are investigated.

6.3 Mixed Impurity Seeding Studies

As already discussed in section 3.3, it might be beneficial to consider mixtures of different impurity species to optimize the impurity seeding recipe. This is investigated in this section via simulations with simultaneous impurity seeding of argon and nitrogen. The experimental conditions from section 3.3 are not exactly reproduced in the simulations, as the modeling has been performed before the experiments. Nevertheless, the plasma conditions are roughly comparable, and the numerical investigations are conducted in accordance with the experimental analysis.

Similar as in figure 3.7 for the experiment, the upstream profiles of electron density and temperature are shown in figure 6.10 for different impurity seeding mixing ratios. The profiles are plotted for a set of simulations with considerable levels of total impurity seeding ($1.0 - 1.8 \cdot 10^{21}\,\mathrm{es}^{-1}$) and comparable divertor conditions, i.e., peak target temperatures[2] at the outer divertor target below 20 eV and peak power loads

[2] As in chapter 2, also here and in the following, the term "target temperature" indicates the plasma temperature in front of the target, and not the temperature of the target plate itself.

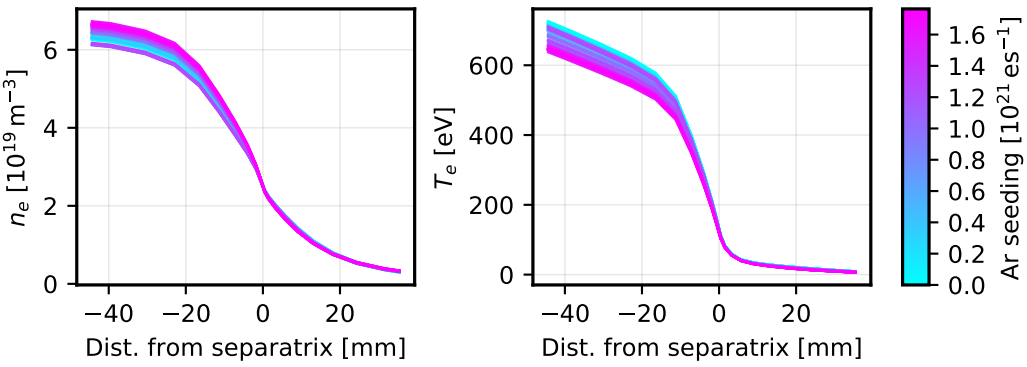

Figure 6.10: Upstream profiles of electron density and temperature from a selection of simulations with mixed argon and nitrogen seeding. Simulations with similar divertor conditions were chosen with total impurity seeding levels between 10^{21} es^{-1} and $1.8 \cdot 10^{21}$ es^{-1}. The argon seeding levels (and hence, the argon fraction) of the particular cases is indicated by the color coding. As the computational domain in the simulations does not cover the whole confined plasma region (cf. figure 4.1), the plotted distance from the separatrix only corresponds to $\rho_{\mathrm{pol}} \approx 0.89 - 1.04$.

below $10\,\mathrm{MWm}^{-2}$. As indicated by the color coding, a significant pedestal top temperature drop can be observed with increasing argon fraction, similarly to what is observed in the experiment (cf. figure 3.7). Also in the simulations, the detrimental impact on the core temperature with increasing argon content is caused by an increasing radiation fraction in the core region (cf. figure 3.9), as expected according to the radiation efficiency. This can be seen in figure 6.11, where the core radiation fraction $P_{\mathrm{rad,core}}$ / $P_{\mathrm{rad,total}}$ is plotted against the argon seeding level (for the same subset of simulations as displayed in figure 6.10).

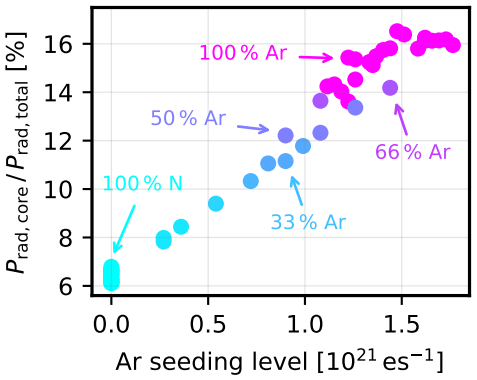

Figure 6.11: Radiation fraction in the core plotted against the argon seeding level in the mixed Ar/N seeding simulations. The argon fraction is additionally indicated by the color coding.

An overview over the operational space can be provided by plotting the peak target temperature and the peak power load against the impact of the impurities

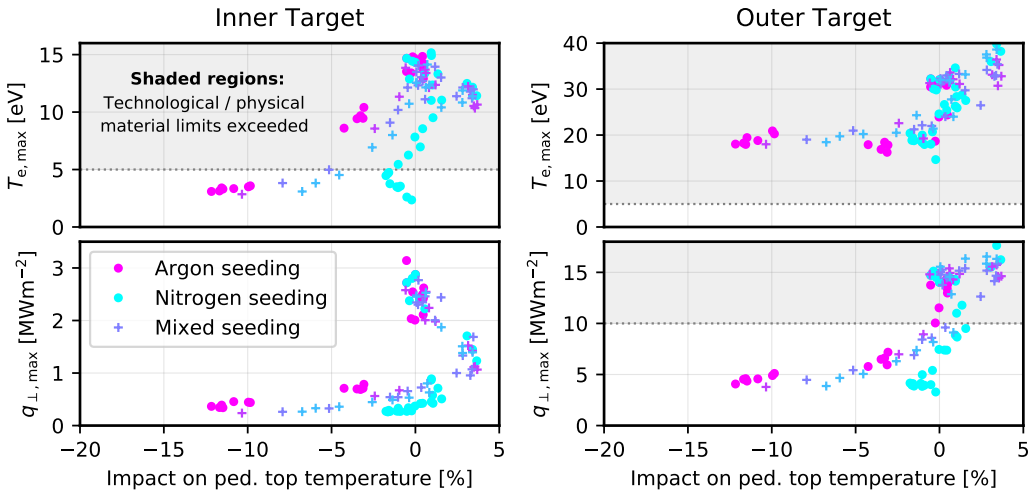

Figure 6.12: Overview over the operational space showing the peak target temperature and divertor power load plotted against the impact on the pedestal top temperature (compared to the unseeded reference case) for the inner target (left) and for the outer target (right). In addition to the pure argon and nitrogen seeding scans, also mixed seeding cases with mixing ratios of $\Gamma_{Ar}:\Gamma_N = 2:1$, $1:1$ and $1:2$ (in terms of atomic fluxes) are shown. The shaded regions indicate the parameter space in which the limits of 5 eV and 10 MWm^{-2} are exceeded.

on the pedestal top temperature. This is shown in figure 6.12 for the inner target (left) and the outer target (right). With sufficient impurity seeding it is possible to meet both the temperature and power load constraints (cf. section 2.2) at the inner target as well as the power load constraint at the outer target. Only for the peak target temperature at the outer target the 5 eV limit is exceeded in all cases. Unfortunately, a further reduction of the outer target temperature cannot be achieved in the simulations, as they become numerically unstable at higher seeding levels. The strongest reduction of the target temperatures and power loads and at the same time the lowest pedestal top temperature drop is obtained with pure nitrogen seeding.

On the other hand, the fuel dilution in the confined region has to be limited, as it reduces the maximum achievable fusion rate in a fusion device. The fuel dilution is defined as the ratio of the main ion species density and the electron density n_{D^+}/n_e. In the experiment, the fuel dilution is not well accessible, but it can readily be calculated in the simulations, where less fuel dilution is obtained with argon seeding than with nitrogen seeding. This is due to the higher argon

radiation efficiency, which results in lower required argon densities at similar power dissipation levels. In figure 6.13 the pedestal top temperature is plotted against the fuel dilution (averaged over the closed flux surface at the pedestal top position). For the highlighted cases shown as thick dots, the target material limits depicted in figure 6.12 are satisfied (with the exception of the outer target temperature limit, where no cases with $T_e < 5\,\mathrm{eV}$ are obtained). According to figure 6.13, the mixing of argon and nitrogen impurities at different mixing ratios allows to achieve a trade-off between pedestal top temperature drop and fuel dilution, i.e., a lower impact on the pedestal top temperature with a higher nitrogen fraction, or less fuel dilution with a higher argon fraction. Depending on which of these two parameters is considered to be more critical in a certain plasma scenario, the impurity mixture can be adjusted accordingly.

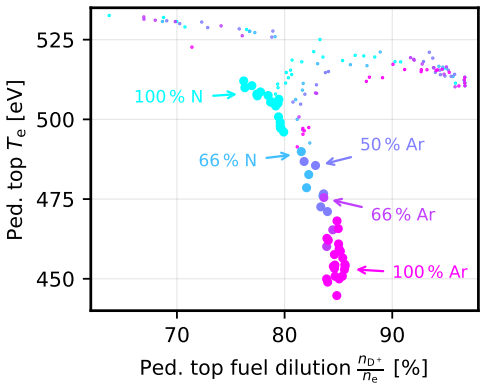

Figure 6.13: Pedestal top temperature plotted against the fuel dilution averaged over the flux surface at the pedestal top position ($\rho_{pol} \approx 0.96$). The highlighted cases (thick dots) satisfy the target material limits as depicted in figure 6.12 (with the exception of the outer target temperature limit). Different argon to nitrogen mixing ratios are distinguished by the color coding.

Additional synergetic effects, like a higher achievable total radiation fraction or a further reduction of the target temperatures and peak power loads are not observed in the simulations with mixed argon and nitrogen seeding. The different impurity species do not affect each other directly. One impurity species affects the other species only indirectly, via a modification of the plasma background (e.g., via a reduction of the temperature, or a modification of the main ion plasma flow), which ultimately has an impact on both species.

In summary, the simulations with mixed argon and nitrogen seeding confirm that the impact of the impurities on the plasma and the radiation distribution can be affected by the choice of the impurity mixing ratio, as it was also observed in the experiment in section 3.3. Additionally, the simulations reveal, that a trade-off between pedestal top temperature drop and fuel dilution can be achieved by an adjustment of the impurity mixing ratio. The results of the analysis can be used as a guidance for future experiments investigating mixed argon and nitrogen seeding.

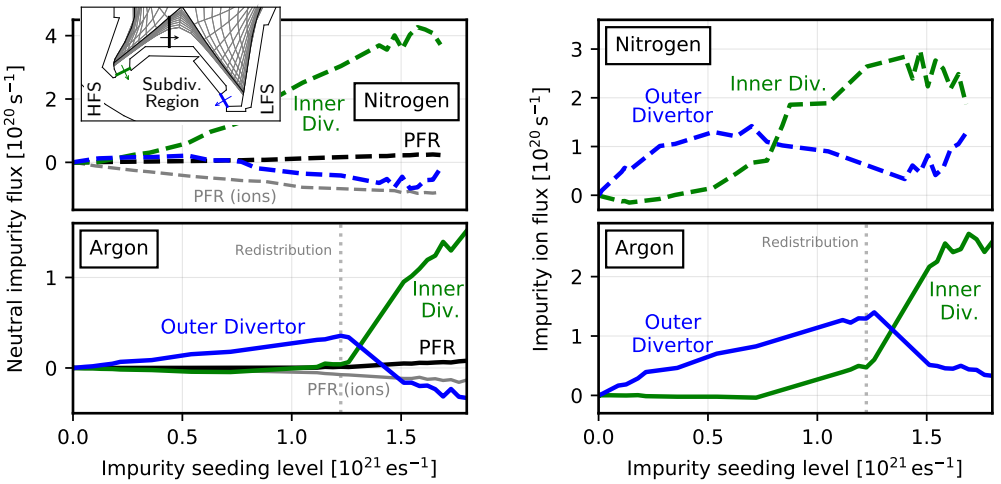

Figure 6.14: Left: Neutral nitrogen and argon fluxes (also considering N_2 molecules) from the HFS PFR to the LFS PFR (black), and towards the subdivertor region from the inner/outer divertor region (green/blue), i.e., across the surfaces displayed in the overlaid plot (with arrows indicating the positive flow direction). For comparison, the gray lines show the parallel impurity ion flux through the PFR (negative values towards the HFS). Right: Total parallel impurity ion fluxes entering the inner and outer divertor regions through the divertor entrance from the main chamber SOL.

6.4 Interpretation of the Argon Density Redistribution

In this section, the impurity transport is investigated in order to facilitate an interpretation of the argon density redistribution, as it was observed in section 6.2. In general, the particle density in a certain region is determined by the particle sources and sinks and the divergence of the flux. Usually, the strongest particle source in the different plasma regions is the ionization of neutral atoms. These either come directly from the gas puff, from volume recombination, or from recycling at the vessel walls, mostly at the divertor targets. For impurities, the volume recombination rate is negligibly low, around $10^9\,\mathrm{s}^{-1}$ at seeding levels in the order of $10^{20}\,\mathrm{s}^{-1}$. On the other hand, the recycling rate is typically in the order of $10^{22}\,\mathrm{s}^{-1}$, and therefore, the dominant contribution. For the redistribution of particle densities, as observed in section 6.2, the neutral fluxes might play an important role, as the neutrals are not necessarily immediately ionized and can travel across different plasma regions, independently of the magnetic field lines. The role of the neutral and ion fluxes in establishing a certain impurity density distribution is discussed in the following.

6.4.1 Neutral Impurity Fluxes

To investigate the importance of the impurity fluxes of neutral argon and nitrogen atoms, as well as N_2 molecules, the left-hand side of figure 6.14 shows the neutral fluxes across different test surfaces. The positions of the test surfaces are indicated in the small overlaid plot. For both argon and nitrogen the neutral fluxes through the PFR (black lines) are always directed from the HFS to the LFS, but small, i.e., below $0.25 \cdot 10^{20}\,\mathrm{s}^{-1}$ for nitrogen and below $0.1 \cdot 10^{20}\,\mathrm{s}^{-1}$ for argon. Due to the strongly increasing impurity densities in the inner divertor (cf. figure 6.3), a large amount of neutrals (up to $4 \cdot 10^{20}\,\mathrm{s}^{-1}$ for nitrogen and $1.5 \cdot 10^{20}\,\mathrm{s}^{-1}$ for argon) escapes from the inner divertor towards the subdivertor region as the impurity seeding level is increased. At low seeding levels also the outer divertor loses neutrals to the subdivertor region. However, at high seeding levels neutrals enter the outer divertor coming from the subdivertor region. This can be interpreted as a neutral particle flux from the inner to the outer divertor through the subdivertor region. Therefore, the neutral fluxes do not explain the modified argon density distribution where particles are shifted from the LFS to the HFS at high seeding levels. Instead, the neutrals rather counteract the redistribution, and balance the increasing parallel impurity ion flux going from the LFS to the HFS through the PFR (see figure 6.14, gray lines) and via the main chamber SOL.

6.4.2 Impurity Ion Fluxes

On the right-hand side of figure 6.14, the net parallel ion influx of impurities into the inner and outer divertor regions coming from the main chamber SOL is shown. The flux enters the divertor volume through the divertor entrance, poloidally at the position of the X-point (see figure 4.1, transition from light blue to green or orange). The high flux values of up to $3 \cdot 10^{20}\,\mathrm{s}^{-1}$ exceeding the applied impurity seeding level (up to $10^{20}\,\mathrm{s}^{-1}$ for argon and $2.6 \cdot 10^{20}\,\mathrm{s}^{-1}$ for nitrogen) are sustained by ionization sources in the main chamber SOL. The neutrals which are ionized in the SOL either originate directly from the recy-

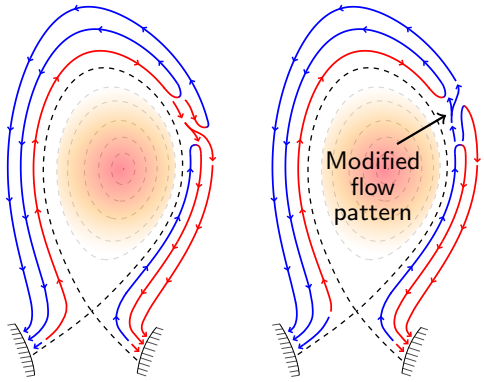

Figure 6.15: Schematic drawing of the typical particle flux patterns (of both, impurities and main ions) as they are observed in the SOLPS 5.0 simulations at low and high impurity seeding levels.

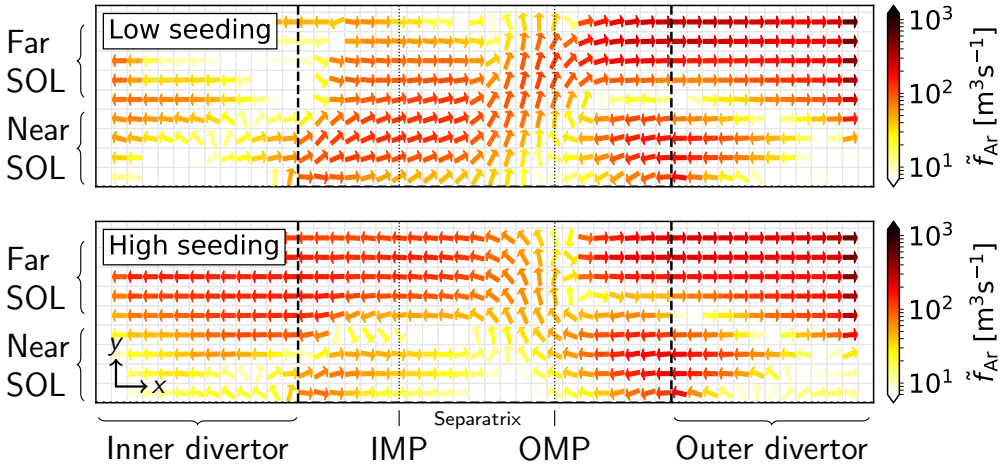

Figure 6.16: Argon particle flux (summed over all charge states and normalized by the argon density) in the SOL for a case at low ($\Gamma_{Ar} = 0.36 \cdot 10^{21}$ es^{-1}) and high argon seeding level ($\Gamma_{Ar} = 1.51 \cdot 10^{21}$ es^{-1}) plotted in the radial-poloidal plane, i.e., in the numerical grid of the SOLPS simulations. As described in figure 4.1, the x-direction corresponds to the poloidal direction and the y-direction to the radial direction.

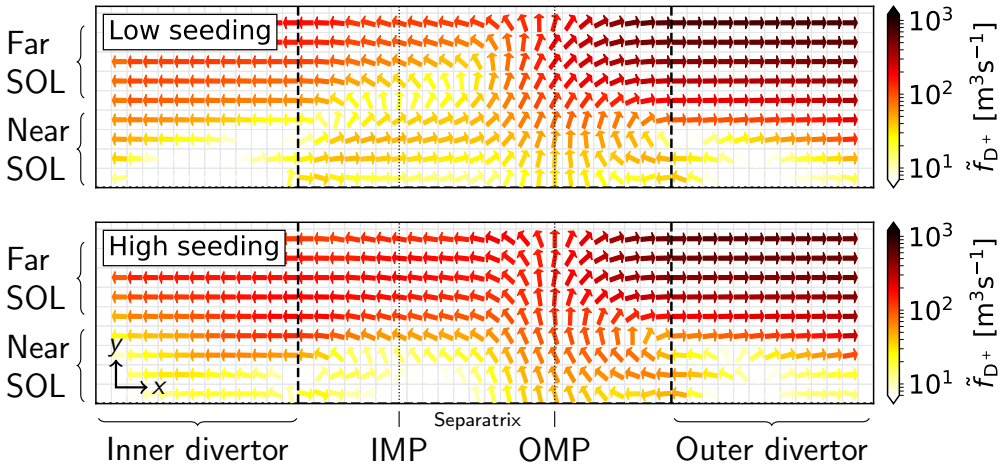

Figure 6.17: Main ion particle flux (normalized by the main ion density) in the SOL for a case at low ($\Gamma_{Ar} = 0.36 \cdot 10^{21}$ es^{-1}) and high argon seeding level ($\Gamma_{Ar} = 1.51 \cdot 10^{21}$ es^{-1}) plotted in the radial-poloidal plane. While the radial transport is determined by diffusion, the parallel main ion flows are driven by the main particle sources and sinks, i.e., mainly by the deuterium ionization sources in the inner and outer divertor regions.

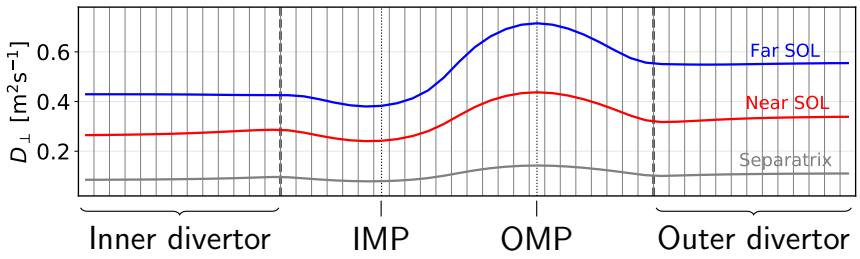

Figure 6.18: Poloidal profiles of the perpendicular particle diffusion coefficient $D_\perp$, illustrating the ballooning of transport (cf. section 5.2), with enhanced perpendicular transport around the outer midplane position. The profiles are plotted for different radial positions, i.e., along a flux tube in the far SOL (with a distance from the separatrix at the outer midplane position of $\Delta s_{\mathrm{omp}} \approx 18\,\mathrm{mm}$), the near SOL ($\Delta s_{\mathrm{omp}} \approx 3\,\mathrm{mm}$) and along the separatrix.

cling of the diffusive perpendicular particle flux onto the main chamber wall, or they are transported into the SOL, mainly from the divertor region. As it can be seen in figure 6.14 (right), at low seeding levels the impurities mostly stream towards the outer divertor, whereas at higher seeding levels the situation is reversed and more particles in the SOL flow towards the inner divertor.

Figure 6.15 schematically shows the typical particle flow pattern in the SOL for a case at low seeding and high seeding as they are observed for both, impurities and main ions. The corresponding normalized argon flux in the numerical grid of the SOLPS 5.0 simulations is shown in figure 6.16. The general main ion and impurity flow direction in most of the SOL is not affected by the impurity seeding (see figure 6.15). However, the actual particle flux (figure 6.16), and more importantly, around the outer midplane position also the qualitative flow patterns (figure 6.15 and figure 6.16), change significantly. At low seeding levels most particles within the SOL are directed towards the outer divertor. Particles escaping the outer divertor in the near SOL cannot reach beyond the outer midplane, as the flux is reversed at this position. Therefore, at low seeding level, effectively no impurity ion can move from the outer divertor to the inner divertor through the SOL. However, at high seeding level, the behavior changes and only a small fraction of particles is returned to the outer divertor, while the majority flows towards the inner divertor. In this situation impurity ions cannot move from the inner to the outer divertor along the SOL.

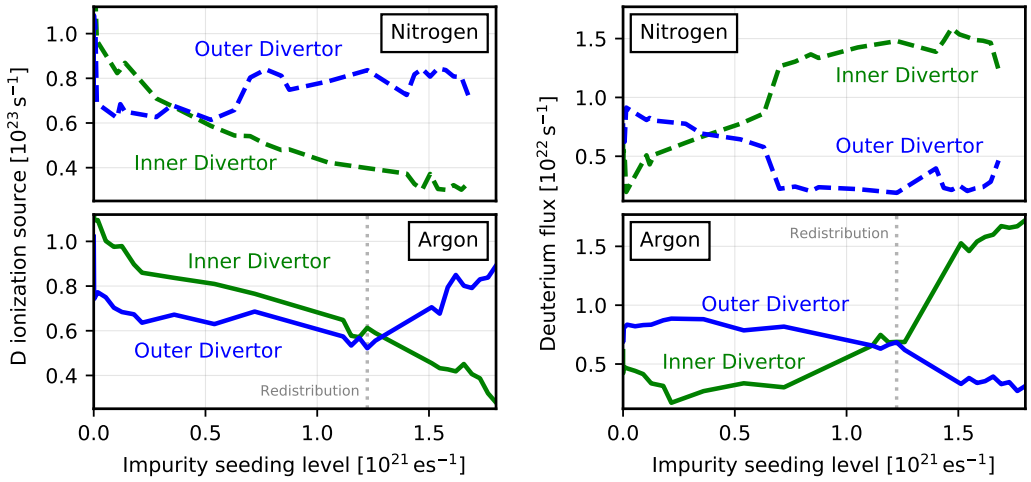

Figure 6.19: Left: Total deuterium ionization source in the inner and outer divertor region for the nitrogen (top) and argon (bottom) seeding scan. Right: Parallel D^+ ion fluxes entering the inner and outer divertor regions.

6.4.3 Impact of the Main Ion Flows

As it can be seen by a comparison of figure 6.16 with figure 6.17, showing the normalized impurity and main ion flows in the SOL, the main cause for the inversion of the impurity flow is a modification of the main ion or background flow pattern. The radial part of these background flow patterns is determined by the diffusive radial transport, which is affected by the ballooning (cf. section 5.2). In figure 6.18 the ballooning is illustrated, showing the increased perpendicular transport coefficients around the outer midplane position. On the other hand, the parallel flows are determined by the particle sources and sinks in the plasma (cf. section 2.2.1), i.e., mainly by the deuterium ionization sources in the inner and outer divertor region. These are shown in figure 6.19 (left) for the argon and nitrogen seeding scans. Due to the changing temperatures and densities, the deuterium ionization is strongly affected by the impurity seeding. The main ion flows entering the inner and outer divertor regions through the divertor entrance (figure 6.19, right) are inverted as soon as the ionization source in the inner divertor drops below the source in the outer divertor (causing the qualitative change of the particle flow patterns, cf. figures 6.15 – 6.17). According to the friction between main ions and impurities (cf. section 2.2.3), this background flow inversion also redistributes the impurities from the outer to the inner divertor.

Comparing nitrogen and argon it can be observed that due to the different radia-

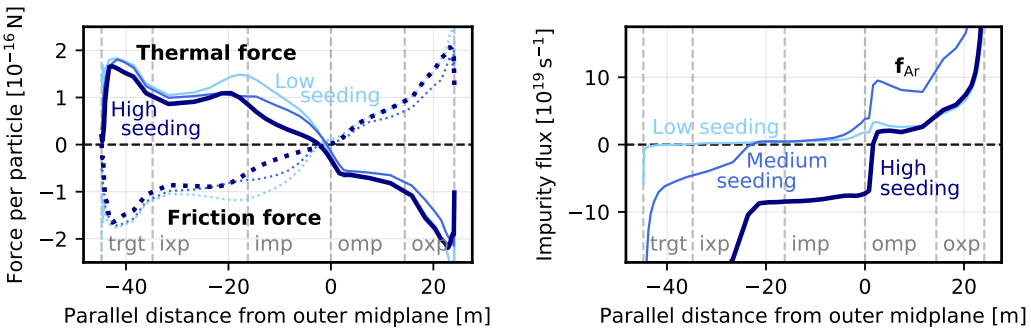

Figure 6.20: Left: Parallel thermal and friction forces acting on a single argon particle (averaged over all charge states) plotted along a flux tube in the near SOL (at $\Delta s_{\mathrm{omp}} \approx 1.5\,\mathrm{mm}$ distance from the separatrix at the OMP) for a case at low, medium and high argon seeding. Right: Total argon particle flux (i.e., sum over all charge states and flux tubes) in the whole SOL. Negative values are directed towards the inner, positive values towards the outer target. The vertical dashed lines mark the inner target, inner X-point, inner midplane, outer midplane, outer X-point and outer target positions.

tion efficiency nitrogen has a stronger impact on the temperature, and therefore also on the main ion ionization source, in the colder inner divertor and a weaker impact in the hotter outer divertor (cf. figure 6.7). Consequently, with nitrogen seeding the deuterium ionization in the inner divertor drops below the ionization rate in the outer divertor already at relatively low seeding levels (figure 6.19, top left). As at this point the nitrogen content is still relatively low, the inversion of the nitrogen concentration (and enrichment) only occurs as a smooth transition (see figures 6.3 and 6.4 around $\Gamma_{\mathrm{N}} = 0.9 \cdot 10^{21}\,\mathrm{es}^{-1}$). In contrast, for argon the redistribution appears at relatively high seeding levels. At this point, with the high argon content, the impact of the impurities on the plasma is strongly affected by the impurity density redistribution, resulting in a further reduction (increase) of the temperature and the deuterium ionization rate in the inner (outer) divertor. Therefore, the flow inversion becomes a self-enhancing process, which explains the sudden change of the flow patterns and the strong and pronounced argon density redistribution.

6.4.4 Thermal Force Acting on the Impurities

Additionally, the modification of the impurity flow pattern is enhanced by the thermal force F_{th} acting on the impurities, resulting in a more pronounced effect in figure 6.16 compared to figure 6.17. As described in section 2.2.3, $F_{\mathrm{th}} \propto \nabla T$ drags

particles away from the targets, due to the parallel temperature profile, which is peaked around the outer midplane position. With increasing seeding level and changing temperature, F_{th} becomes weaker on the HFS, while on the LFS it becomes stronger, resulting in an enhanced drag of particles towards the inner divertor. This can be seen in figure 6.20 (left) showing the thermal force F_{th} and the friction force F_{fr} acting on the argon impurities along a flux tube in the near SOL for three different cases with low ($\Gamma_{\mathrm{Ar}} = 0.36 \cdot 10^{21}\,\mathrm{es}^{-1}$), medium ($1.12 \cdot 10^{21}\,\mathrm{es}^{-1}$) and high argon seeding level ($1.51 \cdot 10^{21}\,\mathrm{es}^{-1}$). As F_{th} results in a deviation of the impurity flow from the background plasma flow, it directly results in an equivalent counteractive friction force $F_{\mathrm{fr}} \approx -F_{\mathrm{th}}$, and therefore, the forces are usually well balanced in the steady state simulations. On the right-hand side of figure 6.20, the total argon particle flux in the entire SOL (i.e., summed over all argon charge states and all flux tubes within the SOL) is plotted for the three cases. The argon flux towards the inner target increases considerably with increasing seeding level (e.g., at the inner divertor entrance from $0\,\mathrm{s}^{-1}$ to $5 \cdot 10^{19}\,\mathrm{s}^{-1}$ to $2.3 \cdot 10^{20}\,\mathrm{s}^{-1}$), which is both due to the modified background plasma flow and the enhanced F_{th}.

6.5 Interpretation of the Outer Divertor Impurity Retention

Considering the total impurity flux through the inner and outer divertor entrances, i.e., the sum of all impurity charge states and all flux tubes in the near and far SOL simultaneously, it could be seen in section 6.4 (figure 6.14, right) that in the entire dataset there are almost no cases with a net outflux of impurities from the two divertor regions. However, if different flux tubes and different impurity charge states are investigated separately, it can be observed that on a local scale certain charge states on certain flux tubes are able to escape the divertor region. A typical argon impurity flux pattern in the outer divertor is depicted in figure 6.21 for a case at medium seeding level ($\Gamma_{\mathrm{Ar}} = 1.12 \cdot 10^{21}\,\mathrm{es}^{-1}$). Qualitatively, similar impurity flux patterns are also observed at different seeding levels, both for nitrogen and argon. While in the far SOL the impurities flow towards the target plate, in the near SOL the impurity flux is reversed at the stagnation point, beyond which particles stream out of the divertor region. The contributions of different charge states to the argon impurity flux across the outer divertor entrance are depicted in figure 6.22 for all SOL flux tubes. The escaping particle flux in the near SOL mostly consists of charge states from Ar^{5+} to Ar^{8+}. In the nitrogen seeding case (not shown here) the same is true for N^{3+} to N^{5+}. Corresponding to the divertor temperatures, higher ionization states are not accessible, while for lower charge states the majority of the particles is ionized before they are able to reach the divertor entrance. In simulations

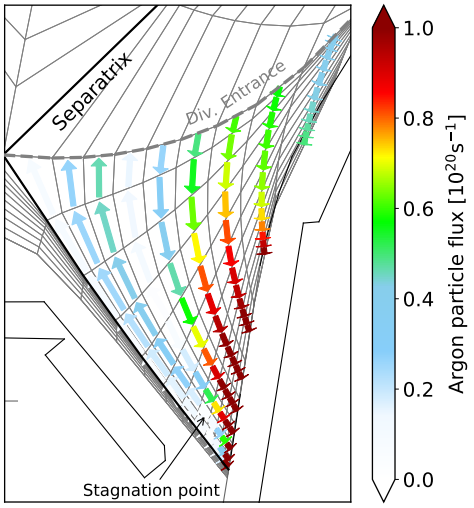

Figure 6.21: Typical argon impurity flux pattern in the outer divertor for a case at medium seeding level ($\Gamma_{\mathrm{Ar}} = 1.12 \cdot 10^{21}\,\mathrm{es}^{-1}$).

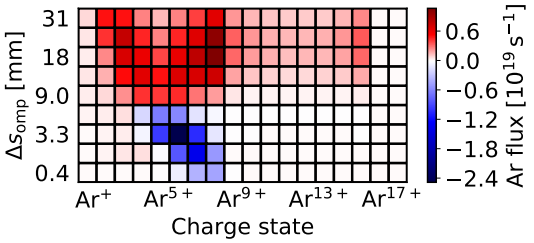

Figure 6.22: Argon particle flux across the outer divertor entrance (i.e., across the dashed gray line in figure 6.21) plotted separately for different flux tubes (i.e., different distances from the separatrix at the OMP Δs_{omp}) and for all argon charge states for a case at medium seeding level ($\Gamma_{\mathrm{Ar}} = 1.12 \cdot 10^{21}\,\mathrm{es}^{-1}$). The negative values (blue) in the near SOL represent an outflux of particles from the divertor region.

with higher divertor temperatures also higher charge states can be obtained in the divertor region. On the other hand, in the colder far SOL also lower charge states can exist, while the existence of particles in higher ionization states can be explained by the impurity transport into the divertor region from hotter regions further upstream.

6.5.1 Role of the Ionization Front Position

As discussed in section 2.2.3, the divertor impurity retention is determined by the relative positions of the ionization front of neutral impurities and the stagnation point of the impurity ion flow. A longer ionization mean free path of the impurity neutrals results in increased divertor leakage. The simulations yield an average ionization mean free path in the outer divertor region (including the PFR) of roughly 6 cm for argon and 9 cm for nitrogen. This is mainly due to the higher mass of argon, which results in a lower thermal velocity at similar temperature. The shorter ionization mean free path explains the superior argon divertor enrichment, while the stronger nitrogen divertor leakage, even at low seeding levels, accounts for the smooth and less pronounced impurity density redistribution with nitrogen (cf. section 6.2). It should be noted, that due to a very short N_2 dissociation mean free path (in the order of only a few micrometers in the simulations), N_2 is almost

immediately dissociated, and identical results are observed in simulations with atomic nitrogen seeding and molecular N_2 seeding.

The impact of the impurity seeding on the divertor retention is schematically illustrated in figure 6.23. With increasing impurity seeding and decreasing temperatures the ionization front is shifted away from the target (going from dashed to solid lines in figure 6.23), according to the ionization potential of the particles. This leads to an increasing fraction of neutral impurity atoms that are able to reach beyond the impurity stagnation point, which contributes to a reduced divertor retention. On the other hand, the impurity seeding also has an impact on the thermal and friction forces (determined by the temperature gradient and the main ion plasma flow), which determine the impurity stagnation point position. This is investigated in more detail in the following.

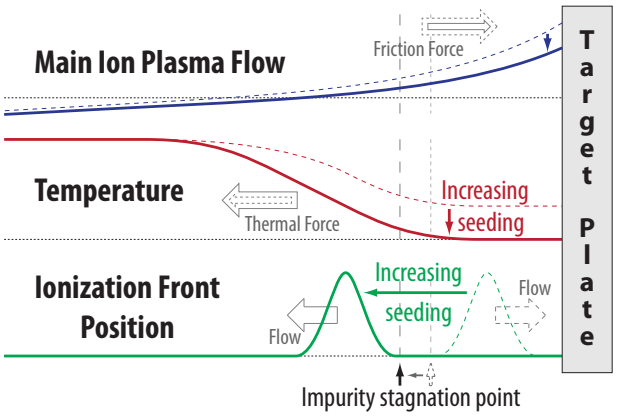

Figure 6.23: Schematic impact of a reduced target temperature and the resulting shifted ionization front position on the divertor impurity retention. For clarity the shift of the ionization front position is strongly exaggerated.

6.5.2 The Impurity Stagnation Point Position

Particles can only escape the divertor region, if they are able to reach beyond the stagnation point (cf. section 2.2.3). Therefore, it is important to investigate what determines the stagnation point position. In the converged steady state case all forces acting on the impurity ions are balanced. As the only relevant forces in the present simulations are the thermal force F_{th} and the friction force F_{fr} we can write (for each impurity charge state separately) [45, 52–54]:

$$F_{\mathrm{th}} \approx -F_{\mathrm{fr}} = -c_{\mathrm{fr}} \left(u_{\mathrm{D}^+} - u_{\mathrm{imp}}\right), \tag{6.1}$$

with the friction coefficient c_{fr} and the parallel velocities of the main ions and impurities u_{D^+} and u_{imp}. Equation (6.1) yields the impurity velocity

$$u_{\mathrm{imp}} \approx u_{\mathrm{D}^+} + F_{\mathrm{th}}/c_{\mathrm{fr}}, \tag{6.2}$$

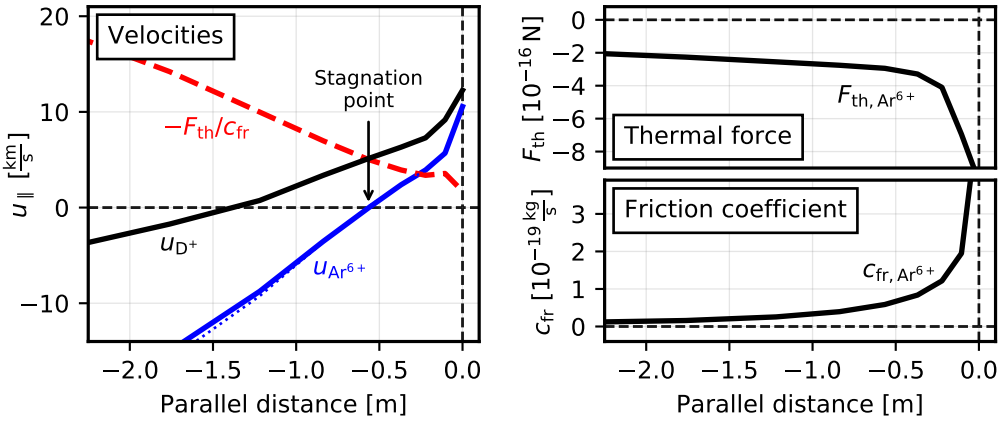

Figure 6.24: Left: Parallel velocities of the main ions u_{D^+} and Ar^{6+} impurities $u_{Ar^{6+}}$ plotted against the distance from the outer target (in the near SOL, $\Delta s_{omp} \approx 1.5\,mm$, for a case at high seeding level, $\Gamma_{Ar} = 1.51 \cdot 10^{21}\,es^{-1}$). Additionally, the ratio of the thermal force and the friction coefficient $-F_{th}/c_{fr}$ is shown, which determines the impurity stagnation point position. Right: Thermal force F_{th} and friction coefficient c_{fr} plotted separately (both for Ar^{6+}).

from which it follows that the impurity stagnation point (i.e., $u_{imp} = 0$) is at the position where the background plasma flow is compensated by the ratio of the thermal force and the friction coefficient:

$$u_{D^+} = -F_{th}/c_{fr}. \tag{6.3}$$

These terms are shown in figure 6.24 exemplary for Ar^{6+} in a case at high seeding level ($\Gamma_{Ar} = 1.51 \cdot 10^{21}\,es^{-1}$), plotted against the parallel distance from the outer divertor target. The discrepancy between the impurity velocity calculated according to equation (6.2) (dotted blue line) and the actual impurity velocity computed in the simulation (solid blue line) is only very small, which confirms the validity of the assumption $F_{th} \approx -F_{fr}$ in equation (6.1). The stagnation point is marked at the position where u_{D^+} (black line) and $-F_{th}/c_{fr}$ (red dashed line) cross. The contributions of F_{th} and c_{fr} are also shown separately in figure 6.24, right. The strong impact of the thermal force can only persist because of a reduction of the friction coefficient c_{fr} in regions with higher temperature, i.e., further away from the target. According to [45], this is expected as the friction coefficient is inversely proportional to the temperature: $c_{fr} \propto n_D Z^2/T^{3/2}$. With $F_{th} \propto Z^2 \cdot \nabla T$, we obtain

$$F_{th}/c_{fr} \propto \frac{T^{3/2} \cdot \nabla T}{n_D}, \tag{6.4}$$

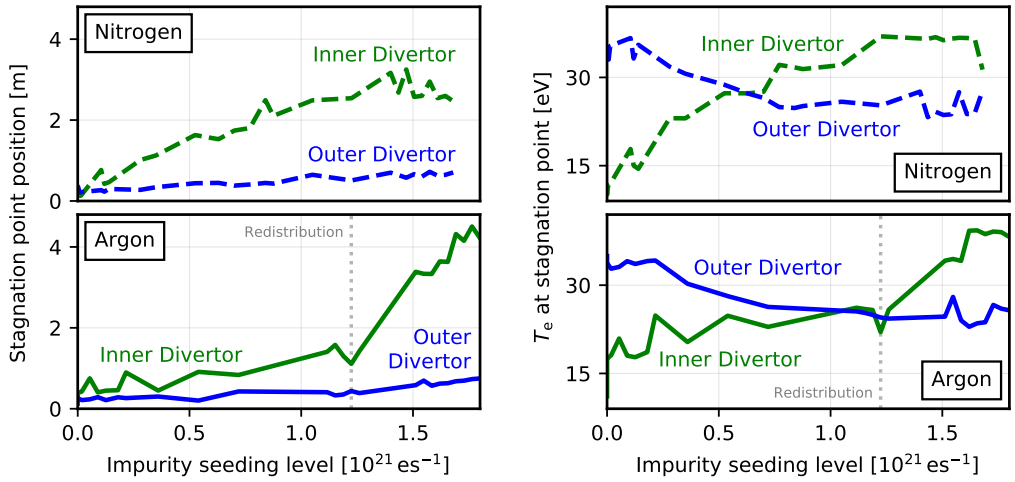

Figure 6.25: Left: Stagnation point position (i.e., the parallel distance of the impurity stagnation point from the target) in the near SOL ($\Delta s_{\mathrm{omp}} \approx 1.5\,\mathrm{mm}$) in the inner and outer divertor plotted against the impurity seeding level for nitrogen (top) and argon (bottom). Right: Electron temperature at the stagnation point position.

where n_{D} is the main ion density and T is the ion temperature.

Considering the impact of impurity seeding on the plasma, we expect decreasing temperature in the divertor region (and usually also increasing density, unless there is significant pressure loss). Under these conditions, impurity seeding results in a reduction of $F_{\mathrm{th}}/c_{\mathrm{fr}}$, according to equation (6.4), which causes a shift of the impurity stagnation point towards the main ion stagnation point and, therefore, further away from the target. This is also confirmed by the simulations, as it can be seen in figure 6.25 (left), where it is shown how the distance of the stagnation point position from the target increases with increasing impurity seeding level in the nitrogen and argon impurity seeding scans. Disregarding the simultaneously shifted neutral ionization front position of the impurities, this indicates a reduced amount of particles reaching beyond the impurity stagnation point, and therefore, an increased divertor impurity retention at higher seeding levels. However, in the overall picture, this mechanism is in competition with the reduced divertor retention caused by the shifted neutral ionization front position, as it was described above.

6.5.3 Semi-Analytic Model for the Divertor Retention

Sections 6.5.1 and 6.5.2 revealed that there is a competition between the shift of the neutral ionization front and the stagnation point position of the impurity ion flow. To

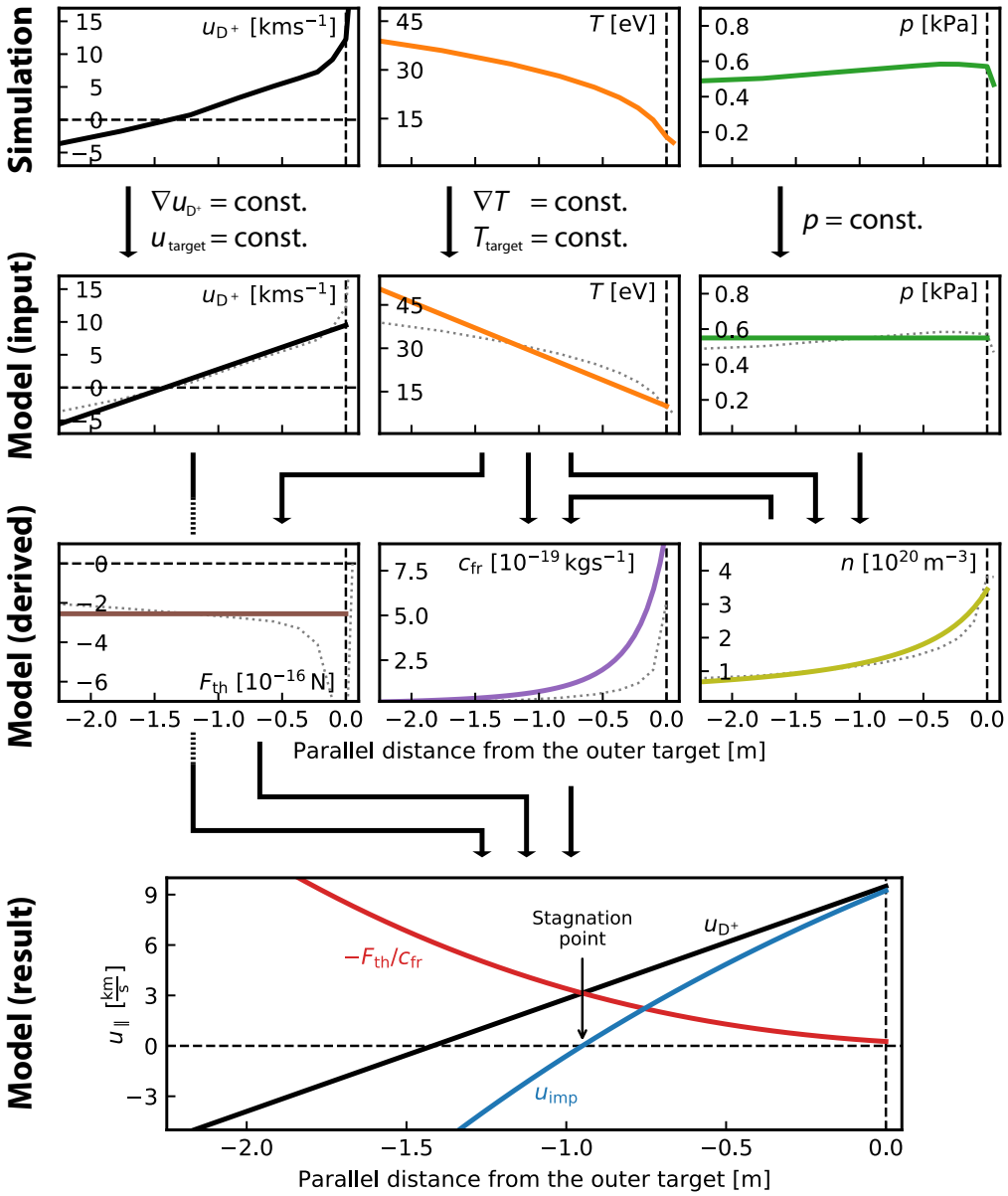

Figure 6.26: Description of the simplified model used to estimate the parameter dependence of the stagnation point position. Motivated by the SOLPS simulations (top row and thin dotted lines), simplified poloidal profiles of the deuterium velocity u_{D^+}, the temperature T and the pressure p in front of the outer target are set up (second row). With constant gradients in the simplified model, the profiles can be described by only a few parameters. According to equations (6.1–6.7), F_{th}/c_{fr} and the stagnation point position (bottom row) are calculated. The arrows indicate according to which input the derived parameters are determined.

investigate under which conditions which of these two mechanisms dominates, the stagnation point position was calculated according to the above equations (6.1 – 6.4) for various different combinations of parameters in a simplified semi-analytic model. The working principle of this simplified model is illustrated in figure 6.26. First, based on the simulation results (figure 6.26, top row), simplified poloidal profiles (second row) are set up under the following assumptions:

- Linearly decreasing velocity of the main ion plasma flow u_{D^+} with increasing distance from the target, either with a fixed velocity at the target $u_{D^+,\mathrm{trgt}}$, or with the sound speed $u_{D^+,\mathrm{trgt}} = c_s = \sqrt{T/m_{D^+}}$,
- linearly increasing temperatures ($T = T_\mathrm{e} = T_i$) with increasing distance from the target,
- either a constant plasma density n throughout the whole divertor region, or a constant pressure p, resulting in $n = p/T$.

From the profiles, the derived parameters can be calculated (figure 6.26, third row), which finally yield the ratio of the thermal force and the friction coefficient $F_\mathrm{th}/c_\mathrm{fr}$ and the stagnation point position. The exact values of F_th and c_fr are calculated according to [45] (section 6.5.3) as

$$F_\mathrm{th} = \frac{3\Big(\mu + 5\,Z_\mathrm{imp}^2\sqrt{2}\left(1.1\mu^{5/2} - 0.35\mu^{3/2}\right) - 1\Big)}{2.6 - 2\mu + 5.4\mu^2}\,\nabla T \tag{6.5}$$

with

$$\mu = m_\mathrm{imp}/\left(m_\mathrm{imp} + m_{\mathrm{D}^+}\right) \tag{6.6}$$

and

$$c_\mathrm{fr} = \frac{m_\mathrm{imp}}{\tau_\mathrm{s,imp}} = Z_\mathrm{imp}^2 \frac{\left(1 + m_{\mathrm{D}^+}/m_\mathrm{imp}\right) n \ln\Lambda}{1.47\cdot 10^{13}\,T\left(T/m_{\mathrm{D}^+}\right)^{1/2}} \tag{6.7}$$

where m_{D^+} is the deuterium mass, m_imp is the impurity mass, $\tau_\mathrm{s,imp}$ is the so-called "stopping time" of the impurity and $\ln\Lambda$ is the coulomb logarithm which is set to $\ln\Lambda = 15$ [45]. For comparison also the actual values computed in the simulation are displayed in figure 6.26 as dotted lines, which follow the trends of the model. As the model is only used to study trends and not absolute values, an exact agreement between the model and the simulations is not pursued. With the above simplifications, the remaining free parameters in the model are the target temperature T_trgt, the temperature gradient ∇T, the main ion velocity gradient ∇u_{D^+}, the target velocity $u_{D^+,\mathrm{trgt}}$ (unless $u_{D^+,\mathrm{trgt}} = c_s$), the density n or the pressure p and the impurity mass m_imp and charge Z_imp. With this variety of parameters, it is in general necessary

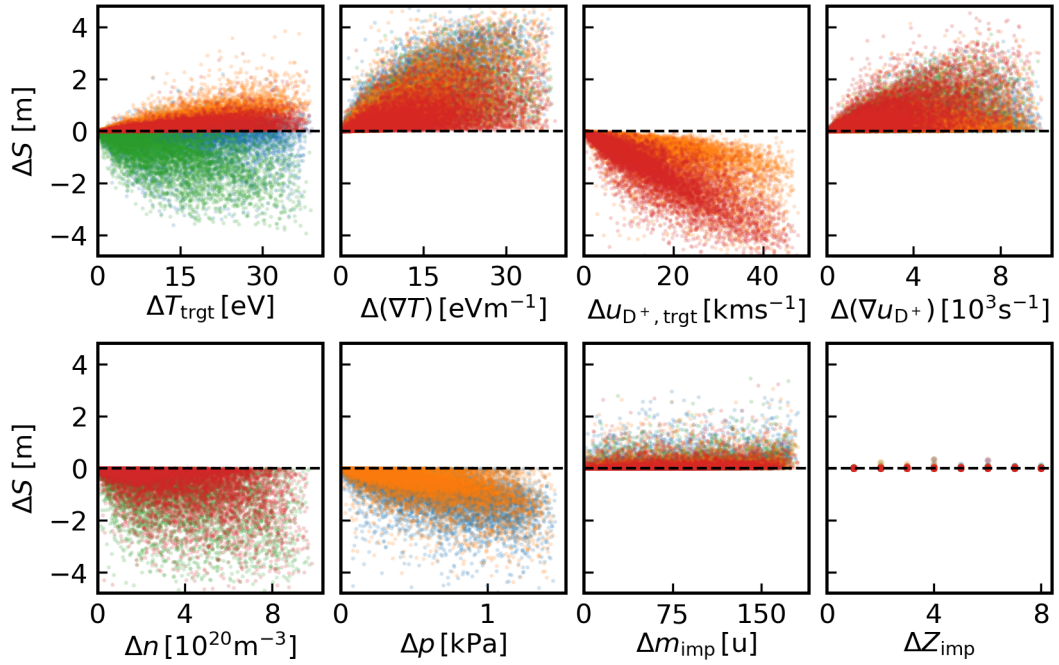

Figure 6.27: Results from the simplified model under a consideration of more than 400.000 randomly chosen different sets of input parameters. The plots show the calculated shift of the stagnation point position ΔS under a modification of the different input parameters. Negative values of ΔS indicate that the stagnation point is shifted away from the target, positive values that it is shifted towards the target when the corresponding input parameter is increased. Different colors of the data points indicate different assumptions in the model as described in the text. Red: Fixed density n and fixed main ion velocity at the target $u_{\mathrm{D}^+,\mathrm{trgt}}$. Orange: Fixed pressure p ($\Rightarrow n = p/T$) and fixed $u_{\mathrm{D}^+,\mathrm{trgt}}$. Green: Fixed n and $u_{\mathrm{D}^+,\mathrm{trgt}} = c_s$. Blue: Fixed p and $u_{\mathrm{D}^+,\mathrm{trgt}} = c_s$.

to consider any specific case separately, in order to investigate the exact behavior. However, to identify general trends, the shift of the stagnation point position under the variation of the above mentioned parameters was calculated for a set of more than 400.000 different randomly chosen parameter combinations.

The results of this analysis are displayed in figure 6.27. The different plots in the figure show the shift of the stagnation point position ΔS under a modification of a particular input parameter as indicated on the x-axis, while all remaining input parameters are kept fixed. As only qualitative trends are investigated here, it is

Increasing parameter X		Stagnation point position $\frac{dS}{dX}$	Temperature at stagn. point $\frac{dT}{dX}$
T_{trgt}	$\in [1, 40\,\mathrm{eV}]$	$\rightleftarrows\vert$	$\nearrow$
∇T	$\in [1, 40\,\mathrm{eVm^{-1}}]$[3]	$\rightarrow\vert$	$\uparrow\downarrow$
$u_{D^+,\mathrm{trgt}}$	$\in [1, 50\,\mathrm{kms^{-1}}]$	$\leftarrow\vert$	$\nearrow$
∇u_{D^+}	$\in [10^2, 10^4\,\mathrm{s^{-1}}]$	$\rightarrow\vert$	$\searrow$
n	$\in [10^{18}, 10^{21}\,\mathrm{m^{-3}}]$	$\leftarrow\vert$	$\nearrow$
p	$\in [1, 1500\,\mathrm{Pa}]$	$\leftarrow\vert$	$\nearrow$
m_{imp}	$\in [2, 184\,\mathrm{u}]$	$\rightarrow\vert$	$\searrow$
Z_{imp}	$\in [2, 10]$	$\rightarrow\vert$	$\searrow$

Table 6.1: Summary of the results from the simplified model, showing the parameter dependence of the stagnation point position and of the temperature at the stagnation point. The arrows indicate if the stagnation point position is shifted away from the target ($\leftarrow\vert$) or towards the target ($\rightarrow\vert$), and if it is shifted to higher ($\nearrow$) or lower ($\searrow$) temperatures, as the corresponding parameter in the first column is increased within the indicated limits.

only important, if the stagnation point position is shifted towards the target or away from the target, i.e., if the data in figure 6.27 is positive or negative. If both positive and negative values are obtained, the stagnation point position can either be shifted towards the target or away from the target, depending on the specific set of the remaining input parameters. Additionally, the results of the analysis are also summarized in table 6.1. The arrows in the middle column of table 6.1 indicate whether the stagnation point is shifted away from the target ($\leftarrow\vert$) or towards the target ($\rightarrow\vert$) as the parameter in the first column is increased.

As discussed above, with a fixed $u_{D^+,\mathrm{trgt}}$, the stagnation point is always shifted away from the target with decreasing target temperatures T_{trgt}. However, if $u_{D^+,\mathrm{trgt}} = c_s$, with the sound speed being deduced from the temperature, the stagnation point can either be shifted away from the target or towards the target, depending on the remaining parameters. This can be seen in figure 6.27 where positive and negative values are obtained for the stagnation point shift ΔS as T_{trgt} is increased, and it is indicated in table 6.1 by the "$\rightleftarrows\vert$" sign. The stagnation point position is almost independent of the charge state Z_{imp}, which appears both in F_{th} and F_{fr} and cancels

[3] As the actual value of the temperature gradient ∇T is negative (cf. figure 6.26), in the present studies ∇T always denotes the absolute value of the gradient, such that a higher value of ∇T corresponds to a steeper temperature profile.

out of the equations, except for a constant offset in F_{th} (cf. equation (6.5)), which results in a marginal shift of the stagnation point position away from the target at low charge states (i.e., with decreasing Z_{imp}). At high impurity masses m_{imp}, the stagnation point is also independent of m_{imp}, and only at low masses it moves away from the target with decreasing m_{imp} due to the $(1 + m_{\mathrm{D}^+}/m_{\mathrm{imp}})$ term in the friction coefficient (cf. equation (6.7)). This indicates a better divertor retention for light impurities (under the assumption of an identical ionization mean free path of the neutral impurity atoms). According to this factor, the friction coefficient for nitrogen is about 9 % larger than that for argon, which already has a small but noticeable impact on the stagnation point position (with the absolute impact depending on the various parameters in the model). However, the reader should be reminded, that with the longer ionization mean free path of nitrogen, nitrogen still shows a stronger divertor leakage than argon.

To be able to correlate the shift of the impurity stagnation point with the shift of the impurity ionization front, one can investigate the parameter dependence of the temperature at the stagnation point position, as the temperature largely determines the ionization front position. This is shown in figure 6.28 and summarized in the third column of table 6.1. For an enhanced divertor retention, the impurity stagnation point should be at a position with high temperature. In this case many impurity neutrals are already ionized before they can reach beyond the impurity stagnation point, and therefore, the particles stay confined in the divertor region. On the other hand, if the temperature at the stagnation point is low, more neutrals can reach beyond the stagnation point, which results in divertor leakage.

The crucial result from the simplified model is that with decreasing target temperatures, the impurity stagnation point is always shifted to lower temperatures in all investigated cases (i.e., ΔT_{S} is always positive for increasing T_{trgt}, see figure 6.28). Therefore, despite the shifted stagnation point position, the dominant mechanism is expected to be the shift of the neutral impurity ionization front, which results in a reduction of the divertor impurity retention with decreasing temperature. Under the simplified assumption, that impurity seeding only affects the temperature, while all other parameters remain roughly constant, this means that increasing impurity seeding always leads to reduced divertor retention. This is also confirmed by the SOLPS simulations in the outer divertor, see figure 6.25 (right). On the other hand, in the inner divertor, the opposite behavior is observed, with increasing temperatures at the stagnation point position at higher seeding levels, indicating an increased divertor retention in the inner divertor. This can be explained by the strongly increasing densities in the inner divertor (cf. figures 6.3 and 6.6), which shift the stagnation point further away from the target towards higher temperatures.

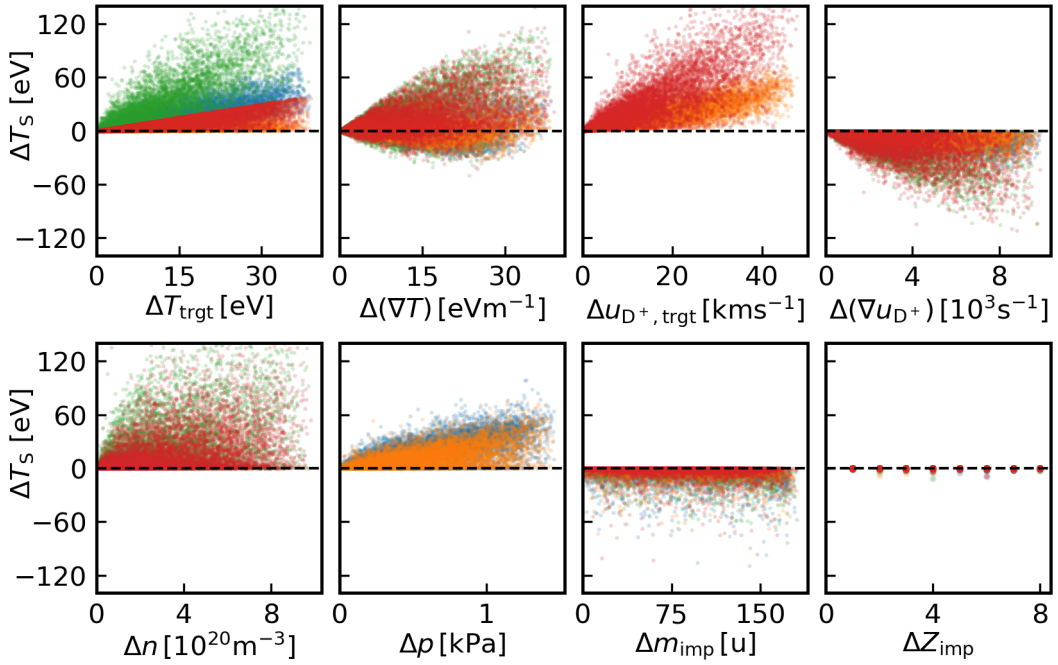

Figure 6.28: Impact of the different input parameters in the simplified model on the temperature T_S at the stagnation point position. Positive values of ΔT_S indicate that the temperature at the stagnation point position increases when the corresponding input parameter is increased. As in figure 6.27, different colors of the data points indicate different assumptions in the model. Red: Fixed density n and fixed main ion velocity at the target $u_{D^+,trgt}$. Orange: Fixed pressure p ($\Rightarrow n = p/T$) and fixed $u_{D^+,trgt}$. Green: Fixed n and $u_{D^+,trgt} = c_s$. Blue: Fixed p and $u_{D^+,trgt} = c_s$.

The increasing divertor retention at the inner divertor and the decreasing retention at the outer divertor contribute to the observed impurity density redistribution (cf. sections 6.2 and 6.4). However, for the outer divertor, the results of this analysis yield a critical conclusion. At low target temperatures, which are required to prevent severe damage of the plasma facing components, a reduced divertor retention is expected, which results in less radiation in the divertor region and in a stronger core contamination. The result is a smaller operational window for the impurity seeding recipe, making it even more challenging to overcome the power exhaust problem.

6.6 Additional Parameter Scans and Open Issues

In this section, a few additional studies are presented which are not directly related to mixed impurities, impurity transport or the divertor retention. To investigate the dependence of the simulation results on the input power, the upstream separatrix density, and the toroidal magnetic field strength, coarse scans of the corresponding parameters have been conducted. However, due to numerical instabilities that were encountered with some of these simulations, only a limited number of converged simulations could be obtained, and therefore, the aspects considered in this section largely remain open issues.

6.6.1 High Power Simulations

In order to extend the analysis to a parameter range which is more relevant for future fusion devices, it is essential to consider simulations with higher input power and separatrix density. For this purpose a coarse input power and density scan has been conducted. The simulations are performed with an input power crossing the core boundary of 5 – 25 MW and densities at the outer midplane separatrix position between $2.5 \cdot 10^{19}\,\mathrm{m}^{-3}$ and $5 \cdot 10^{19}\,\mathrm{m}^{-3}$. Apart from these modifications, the basic modeling setup as described in section 5.2 applies. Unfortunately, the simulations with high input power and increased upstream separatrix electron densities are numerically challenging and require intense maintenance, and only a few converged simulations could be obtained. Furthermore, at increased input power the issue with the deficient particle balance (cf. section 4.2.9) turns out to be even more critical, despite constant time traces in the simulations. Therefore, the particle balance is disregarded as convergence criterion, and the results of the high power simulations have to be considered with care.

With higher input power also much higher seeding levels can be achieved in the simulations (cf. table 5.2). Nevertheless, the simulations show, that with high input power ($\geq 10\,\mathrm{MeV}$) and low plasma density ($n_{\mathrm{e,sep}} = 2.5 \cdot 10^{19}\,\mathrm{m}^{-3}$), the power exhaust cannot be handled, as the material constraints are strongly exceeded even at highest impurity seeding levels. Therefore, higher densities are required, as according to equation (2.7) the radiated power increases linearly with the electron density. Additionally, as the density is expected to increase faster in the divertor region than upstream ($n_{\mathrm{target}} \propto n_{\mathrm{e,sep}}^3$) [45], an increased upstream density will even result in considerably stronger divertor radiation.

With the wide range of parameters in the dataset, an overview over the operational space can be provided. For this purpose, a parameter should be investigated,

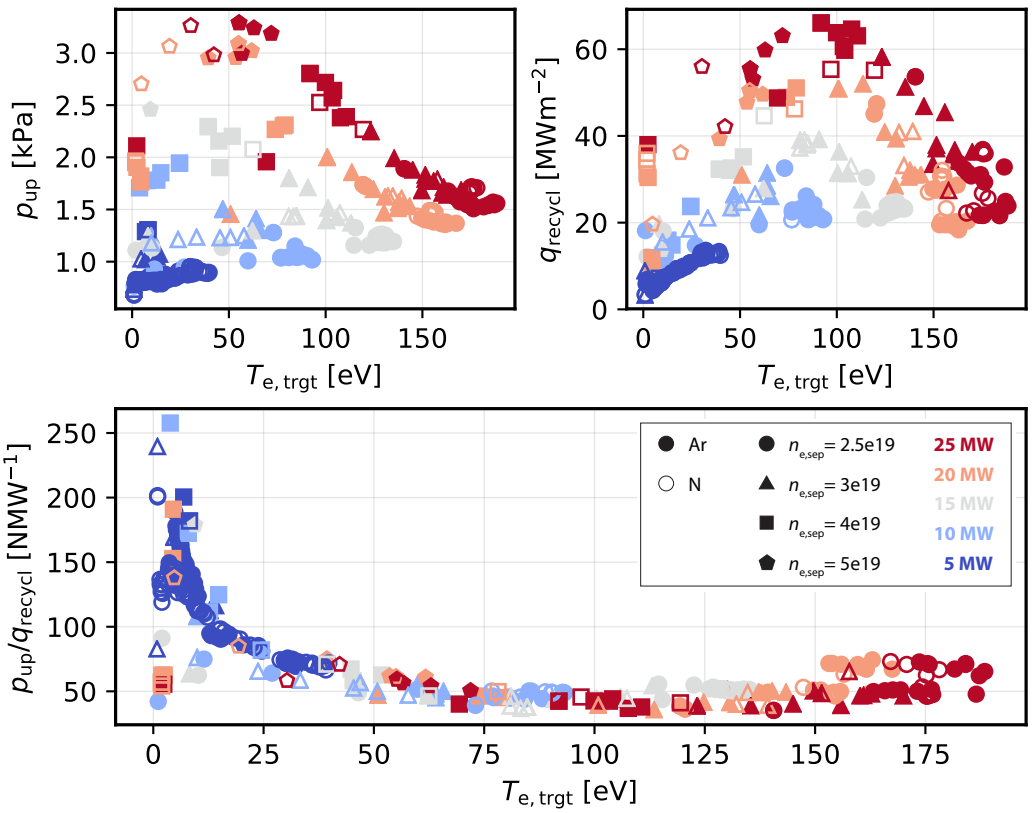

Figure 6.29: Upstream pressure p_{up} and power reaching the recycling region q_{recycl} as well as the ratio p_{up}/q_{recycl} plotted against the outer target temperature $T_{e,trgt}$. The values are taken from a flux tube in the near SOL ($\Delta s_{omp} \approx 1.5\,mm$). Different symbols indicate which upstream separatrix electron density was specified and if argon or nitrogen seeding was applied. The input power can be deduced from the color coding.

which is decisive for the divertor conditions, independently of the input power and upstream density. According to [170], the critical parameter which determines the divertor conditions is the ratio of the upstream plasma pressure p_{up} to the power flux reaching the recycling region q_{recycl}. As in [170], q_{recycl} is defined as the power flux at the position where the integrated deuterium ionization rate within the flux tube reaches 85 % of the total ionization rate between target and outer midplane. For the whole dataset of simulations with increased input power and upstream density, the values of p_{up}, q_{recycl} and p_{up}/q_{recycl} are displayed in figure 6.29,

plotted against the outer target temperature $T_{e,trgt}$, for a flux tube in the near SOL (at $\Delta s_{omp} \approx 1.5\,mm$ distance from the separatrix at the OMP). While p_{up} and q_{recycl} alone show no correlation to the target temperature $T_{e,trgt}$, the ratio p_{up}/q_{recycl} turns out to be correlated to $T_{e,trgt}$ throughout all investigated plasma parameter combinations. This confirms that p_{up}/q_{recycl} is an important parameter for power exhaust. According to the low power simulations with considerable impurity seeding levels and significantly reduced target temperatures and peak power loads, a value of $p_{up}/q_{recycl} \gtrsim 120\,NMW^{-1}$ is required. As it can be seen in figure 6.29, it is only possible in a few high power cases to sufficiently increase p_{up}/q_{recycl} and reach reasonable divertor conditions via a high plasma density or by significant impurity seeding in the present simulations. Therefore, the high power simulations are not yet well suited for further detailed investigations, which should be continued in future studies.

6.6.2 Upstream Plasma Pressure vs. Power Flux to the Recycling Region

For the low power simulations, figure 6.30 shows p_{up}/q_{recycl} plotted against the total radiation fraction in the SOL. As expected, higher radiation fractions are achieved with increasing impurity seeding levels. However, as soon as a certain radiation fraction in the SOL of roughly 50 % is reached, it remains almost constant, even though the impurity seeding level is increased further. It might be reasonable, to consider this point where the maximum achievable radiation fraction is first reached as the point with the optimum impurity seeding level. At higher seeding levels there is (almost) no more further benefit, and the impurities might start to develop a detrimental impact on the confined plasma. Interestingly, at this point, p_{up}/q_{recycl} keeps increasing in the feedback cases, while it begins to decrease in the feed-forward cases. This can be understood, if one considers the impact of the impurity seeding on the upstream density. As discussed in section 6.2.5, with a feedback mechanism on the upstream separatrix density, the deuterium fueling has

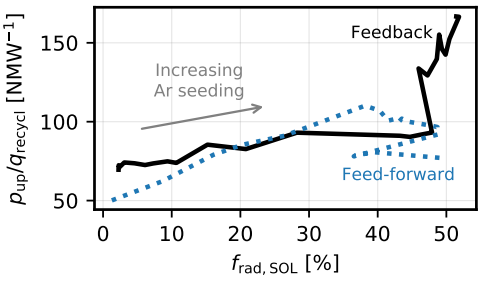

Figure 6.30: Ratio of the upstream plasma pressure to the power reaching the recycling region p_{up}/q_{recycl} plotted against the total radiation fraction in the SOL $f_{rad,SOL} = P_{rad,SOL}/P_{sep}$ (where P_{sep} is the power crossing the separatrix). Displayed are the feedback and feed-forward simulations (with a deuterium fueling rate of $\Gamma_D = 2 \cdot 10^{21}\,es^{-1}$) with argon seeding.

to be increased considerably at higher seeding levels to keep the density constant. On the other hand, with strong impurity seeding and constant deuterium fueling, the upstream density and with it the upstream pressure decreases significantly, which consequently also results in a reduction of $p_{\mathrm{up}}/q_{\mathrm{recycl}}$. Therefore, there is a maximum value of $p_{\mathrm{up}}/q_{\mathrm{recycl}}$ in the feed-forward cases, which also seems to be correlated to the maximum achievable radiation fraction in the SOL. It should be investigated in more detail, if the maximum value of $p_{\mathrm{up}}/q_{\mathrm{recycl}}$ can be used to identify the optimum impurity seeding level, at least with constant deuterium fueling. Unfortunately, with the limited number of feed-forward simulations in this work, the results do not allow a final conclusion in this regard.

6.6.3 Toroidal Magnetic Field Scan

The importance of the magnetic field for power exhaust is discussed in [171]. The studies are based on empirical scalings and a 0D exhaust model and indicate that the parallel heat flux in the SOL scales strongly with the toroidal magnetic field $q_{\parallel} \sim B_{\mathrm{t}}^{2.52}$. To assess the influence of the magnetic field in the simulations, the strength of the toroidal magnetic field B_{t} has been rescaled to obtain values of $B_{\mathrm{t}} = 1\,\mathrm{T}$, $2\,\mathrm{T}$, $2.5\,\mathrm{T}$ (as in the basic modeling setup), $3\,\mathrm{T}$, $4\,\mathrm{T}$, $5\,\mathrm{T}$ and $6\,\mathrm{T}$, while the poloidal magnetic field is kept constant. It should be noted, that the maximum magnetic field strength accessible in ASDEX Upgrade is 3.9 T, and the presented analysis is a purely numerical exercise. Different cases have been set up without impurity seeding, with pure argon seeding ($\Gamma_{\mathrm{Ar}} = 1.12 \cdot 10^{21}\,\mathrm{es}^{-1}$), with pure nitrogen seeding ($\Gamma_{\mathrm{N}} = 1.4 \cdot 10^{21}\,\mathrm{es}^{-1}$) and with mixed impurity seeding ($\Gamma_{\mathrm{N}} = 0.56 \cdot 10^{21}\,\mathrm{es}^{-1}$ and $\Gamma_{\mathrm{Ar}} = 0.72 \cdot 10^{21}\,\mathrm{es}^{-1}$). Apart from the mentioned modifications, the basic modeling setup as described in section 5.2 is applied.

The simulations show that a modification of the magnetic field strength has a significant impact on the plasma solution, even though drifts, which depend as $1/B$ on the magnetic field, are not activated. The most fundamental difference between simulations with different toroidal magnetic field strength is the parallel connection length between the upstream position and the divertor targets. A stronger toroidal magnetic field directly leads to an increased connection length, as (with a constant poloidal magnetic field strength) the stronger toroidal field results in more toroidal turns of the magnetic field lines in one poloidal turn. Consequently, with an increased connection length the parallel gradients are reduced, which strongly affects the particle and energy transport equations. Additionally, it takes a longer time for particles and energy to reach the divertor targets, which in turn allows more radial transport in the SOL. The enhanced radial transport can be seen in figure 6.31

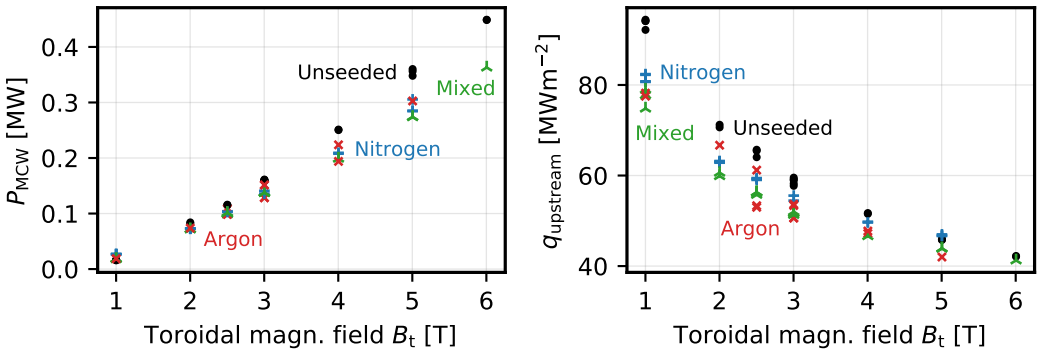

Figure 6.31: Total radial power flux towards the main chamber wall P_{MCW} and the poloidal upstream power flux q_{upstream} in the near SOL, plotted against the toroidal magnetic field strength B_t.

(left), showing the radial power flux onto the main chamber wall, plotted against the magnetic field strength B_t. A significant amount of power is transported radially outwards with increasing B_t. The stronger magnetic field also results in a significant reduction of the poloidal upstream power flux (figure 6.31, right). The power width λ_q increases from roughly 1.5 mm to 2.5 mm going from $B_t = 1\,\mathrm{T}$ to $B_t = 6\,\mathrm{T}$ in the unseeded scenario.

With the reduction of the poloidal power flux at higher B_t, a comparison of the simulation results with the scaling from [171] is difficult. As $q_{\parallel} = \frac{B}{B_p} q_{\mathrm{pol}} \approx \frac{B_t}{B_p} q_{\mathrm{pol}}$, the parallel power flux still increases with B_t, however with a much lower rate as discussed in [171]. It has to be concluded, that the simulations are not well suited for a comparison with a simple 0D scaling, as a modification of the magnetic field (or to be more precise, the resulting modification of the connection length) has a significant impact on the heat and particle transport, resulting in completely altered plasma solutions. Nevertheless, a detailed analysis of the magnetic field scan and a comparison to the analysis from sections 6.2 – 6.5 revealed, that also with a modified magnetic field, the impact of impurities on the plasma can be attributed to the same physical mechanisms as described previously in this chapter, confirming the previous conclusions.

6.7 Validity of the Simulation Results

Impurity seeding will be an important prerequisite for a safe operation of future fusion devices. A valuable tool to study impurity seeded plasmas is provided by

the SOLPS 5.0 code. Unfortunately, the simulations have limitations and constraints which often cause a deficient agreement between the simulated and experimental results or between the specified control parameters required to obtain similar plasma conditions. However, it should be kept in mind, that the simulations do not attempt to perfectly reconstruct the experiment or reality. In contrast, simplified models are applied in the simulations to allow an identification of the most important physical mechanisms which are crucial for the explanation of certain phenomena, and to facilitate improved understanding. For this purpose, a perfect match between experiment and simulation is usually not required, and an increased complexity of the simulations might even hinder a comprehensive analysis. Nevertheless, the limitations and constraints of the code should be considered when it comes to interpretation and the major limitation which apply in this work are discussed in the following.

6.7.1 Atomic and Molecular Effects

A comparison of simulations with atomic nitrogen seeding and molecular N_2 seeding revealed identical results, as N_2 is almost immediately dissociated, due to its short mean free path in the order of only a few micrometers. Additional surface interactions and molecular effects like ammonia production, which might result in additional power loss due to the impurities, are not taken into account. These effects are an open area of research [172–174] and they are not provided in the atomic reaction database used in this work [158]. Also the assumption of fully recycling nitrogen at the boundaries of the computational grid has to be considered. With a recycling coefficient smaller than one, higher nitrogen seeding levels might be required to obtain similar radiation fractions, due to wall pumping of nitrogen. On the other hand, after the nitrogen content on the walls is saturated, which happens on timescales in the order of seconds in the experiment, all incident nitrogen is reemitted [168, 175], and hence, the assumption of full recycling is well satisfied. Regarding the neutral divertor pressure, it should be noted, that there is a discrepancy between experiment and simulation [176]. This issue can only be resolved with activated drift terms and modified SOL transport [85], which is not attempted in this work. In the present simulations, the neutral divertor pressure is in the order of only 0.1 Pa, which results in reduced neutral pumping and particle throughput. This explains why the fueling and seeding rates in the simulations often differ from the experimentally applied values at similar plasma conditions. However, as the main particle sources in the plasma originate from recycling, the discrepancy in the fueling and seeding rates is not expected to have any significant impact on the simulations.

6.7.2 Perpendicular Transport

Another limitation of the simulations is the purely diffusive approach of the perpendicular transport with fixed transport coefficients. In the present simulations, a detailed match between the simulations and any particular experimental discharge is not attempted. The transport coefficients are not readjusted in the simulations at higher seeding levels, even though in reality the impurity seeding might affect the transport. It is observed in the simulations that with increasing seeding levels (for both argon and nitrogen) the radial fall-off lengths of the upstream density λ_{n_e} and power flux λ_q slightly decrease, and while λ_{T_e} stays rather constant, λ_{T_i} shows a slight increase, as it can be seen in figure 6.32. However, the deviations are small. The fall-off lengths in the different simulations only deviate by the following values from the average value within the whole dataset: $\lambda_{n_e} \approx 16 \pm 2\,\mathrm{mm}$, $\lambda_{T_i} \approx 7.8 \pm 0.8\,\mathrm{mm}$, $\lambda_{T_e} \approx 4.4 \pm 0.3\,\mathrm{mm}$ and $\lambda_q \approx 1.9 \pm 0.3\,\mathrm{mm}$. Therefore, the fixed transport coefficients are not expected to have a significant impact on the results of the analysis. Additionally, modifying the transport coefficients within the dataset would add another degree of freedom and even further enhance the difficulty of disentangling the causes for certain effects. Hence, it is concluded that the best comparability of different simulations is provided with the transport coefficients kept fixed.

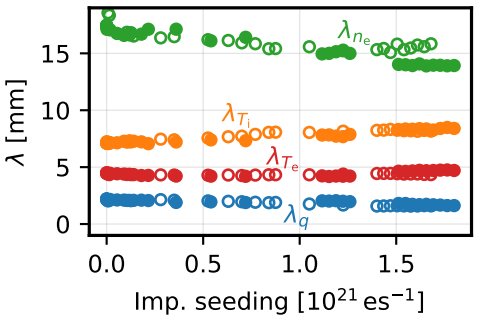

Figure 6.32: Fall-off lengths of the radial upstream profiles of electron density λ_{n_e}, electron temperature λ_{T_e}, ion temperature λ_{T_i} and the power flux λ_q in the simulations. Cases with nitrogen seeding are represented by hollow symbols, argon seeding by filled symbols.

It should also be taken into account, that in a future fusion device the pedestal and edge impurity transport is expected to differ from that in a smaller machine like ASDEX Upgrade [177]. Nevertheless, the underlying physical mechanisms that were investigated in this work are fundamentally valid. Furthermore, without ELMs [31, 153], an important mechanism for the edge and core transport is not accounted for. Consequently, the impurity concentrations and enrichment values do not necessarily agree with experimental values. Nevertheless, the simulation results are valid for steady inter-ELM phases, while the impact of ELMs is an active field of study not considered in this work.

6.7.3 Impact of Drifts

One of the most important limitations of the simulations in this work is the absence of fluid drifts. The activation of drift terms in the simulations can result in a strongly non-linear response of the plasma solution and rearrange the plasma considerably. Therefore, it is very difficult to give any reliable prediction concerning the impact of drifts. Nevertheless, at least qualitatively, the expected directions of the drift flows are shown in figure 6.33, for which the drift formulas of the $E{\times}B$ drift and the diamagnetic drift (equations (4.14) and (4.15)) have been calculated according to the background plasma parameters from a non-drift simulation. This simulation was performed at a medium argon seeding level ($\Gamma_{\mathrm{Ar}} = 1.12 \cdot 10^{21}\,\mathrm{es}^{-1}$) and in forward field direction ($\nabla \boldsymbol{B}$ drift pointing down). Whereas the $E{\times}B$ drift is the same for all species and charge states, for the diamagnetic drift, the density weighted average ($\bar{v}_{\mathrm{dia}} = \sum v_{\mathrm{dia,cs}} n_{\mathrm{cs}} / \sum n_{\mathrm{cs}}$) of all argon charge states is depicted. On the LFS in the common SOL the poloidal drifts (both $E{\times}B$ and diamagnetic) shift the particles towards the outer divertor. The radial drift velocities indicate an increased cross-field transport of particles into the core region on the low-field side between the outer midplane and X-point positions, and an outward transport above

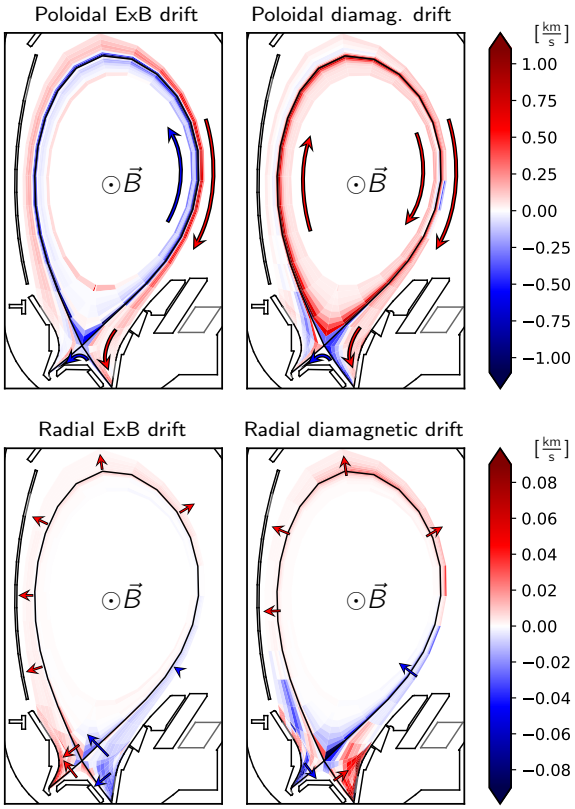

Figure 6.33: Expected poloidal and radial $E{\times}B$ and diamagnetic impurity drift velocities, calculated according to the plasma parameters in a medium argon seeding case ($\Gamma_{\mathrm{Ar}} = 1.12 \cdot 10^{21}\,\mathrm{es}^{-1}$). The arrows indicate the direction of the flow, whereas the strength of the flow can be deduced from the background color. Positive values (red) are pointing poloidally towards the outer divertor or radially outwards, and negative values (blue) are pointing poloidally towards the inner divertor or radially inwards.

the outer midplane and on the high-field side. In the divertor and private flux regions, the radial $E \times B$ and diamagnetic drifts act against each other at comparable strengths (calculated on the non-drift background), and it is difficult to give a prediction on the impact of the drifts in these regions.

The impact of drifts has been investigated thoroughly, both in experiment and simulations [55, 85, 178–181]. It is commonly observed, that drifts enhance the asymmetry between the inner and outer target temperature, i.e., drifts contribute to higher (lower) temperatures at the outer (inner) target. Increased ion fluxes at the inner target (unless detachment sets in) and reduced fluxes at the outer target are reported. The drifts also lead to parallel Pfirsch-Schlüter flows [182] and shift particles (both main ions and impurities) in the common SOL towards the outer divertor. This will have an impact on the main ion and impurity particle flow patterns in the SOL (see figures 6.16 and 6.17), that were identified to be crucial for the explanation of the impurity density redistribution in the non-drift simulations discussed in this work. With an increased temperature at the outer target, also the reduction of the outer divertor retention, as discussed in section 6.5, might be mitigated. Therefore, it can be assumed, that with drifts the argon density redistribution will be mitigated or shifted to higher impurity seeding levels.

According to [55], where SOLPS-ITER impurity transport investigations for ASDEX Upgrade and ITER with nitrogen and neon seeding including drift terms were performed, the divertor impurity retention is mostly determined by the relative positions of the ionization fronts of the main ion and impurity neutrals. This confirms the importance of the ionization front positions, as it was also discussed in section 6.5. However, the results presented in [55] indicate that with drifts activated the ionization front positions are considerably shifted away from the target. In the simulations presented in this work (i.e., without drifts) the position of the maximum neutral ionization rate is always within the first one or two computational grid cells directly in front of the target (which means a few mm away from the target). Therefore, a direct comparison of the present simulations (without drifts) with the conclusions from [55] is not possible.

The constraints of the simulations discussed above have to be kept in mind. Nevertheless, the physical understanding gained by the analysis is fundamentally valid and the impact of additional mechanisms (like drifts) can only be understood in its entirety if the situation without these additional mechanisms is well-understood.

6.7.4 Comparison to the Literature

The observed differences between the impact of argon and nitrogen on the plasma in the SOLPS 5.0 simulations agree well with the experimental observations reported in [41] (cf. section 3.1.2), with the stronger impact of argon on the confined plasma. For an experimental analysis of mixed argon and nitrogen impurities on ASDEX Upgrade, dedicated discharges have been performed (section 3.3). An analysis of the discharges confirms, that the impact of the impurities on the plasma, and the radiation distribution can be affected by an adjustment of the impurity mixture, as observed in the simulations. Regarding the impurity transport, the observed flow patterns of main ions and impurities (cf. figure 6.15) slightly differ from the flows observed in the SOLPS-ITER simulations for ASDEX Upgrade presented in [55] (cf. section 4.3), which most probably can be attributed to the impact of drifts. Attempts to experimentally assess the divertor retention are, e.g., reported in [59, 60]. In [60] at higher densities an improved divertor retention is observed, while after detachment the divertor retention decreased. This is consistent with the expectations from the simplified semi-analytic model described in section 6.5. On the other hand, in [59], a reduced divertor retention with increasing divertor temperature is observed, which contradicts the simplified model. Possibly, this might be explained by a modified main ion plasma flow due to the higher heating power, which is related to higher divertor temperatures in [59].

Chapter 7

Summary and Conclusions

Power exhaust will be a critical issue in future fusion devices. In an unmitigated scenario the material limits of the power flux to the divertor targets will easily be exceeded. The technological constraints suggest that the peak power loads have to stay below $5-10\,\mathrm{MWm^{-2}}$, and the plasma temperature in front of the target plates must be kept below $5\,\mathrm{eV}$ to avoid excessive erosion of target material. In order to reduce the peak power loads and temperatures at the divertor targets, an intentional injection of impurity species into the plasma – so-called impurity seeding – is required. As a result, due to the radiative power dissipation of the impurities, the power is distributed more uniformly onto the vessel walls instead of being focused onto a small area on the divertor targets. However, if the impurities reach the main plasma, they can result in a considerable confinement degradation and fuel dilution. Therefore, to avoid a detrimental impact on the confined plasma and the burn conditions, the impurity seeding recipe has to be optimized.

For this purpose, different studies investigating argon and nitrogen seeding, as well as mixtures of both species, were performed in this work. At the given temperatures, nitrogen radiates mainly in the divertor region, while argon shows enhanced radiation in the core and edge region, which is due to differences between the argon and nitrogen radiation efficiencies. A set of dedicated ASDEX Upgrade high-confinement (H-mode) discharges with different impurity seeding mixtures of argon and nitrogen was analyzed in chapter 3. The experimental observations reveal a different behavior depending on the impurity mixing ratio. With increasing argon fraction, a considerable temperature drop in the core region of about $25-30\,\%$ is observed compared to the scenario with pure nitrogen seeding, while apart from that similar plasma and divertor conditions prevail, i.e., similar profiles of the ion saturation current at the outer divertor target and similar upstream electron densities are measured. The core temperature drop with increasing argon fraction can be explained by the enhanced core radiation. The results of the analysis indicate that the radiation distribution and the impact of the impurities on the plasma can be affected by the choice of the impurity mixing ratio.

Motivated by the experimental observations, a more detailed analysis of argon and nitrogen seeded plasmas was performed via numerical simulations with the SOLPS 5.0 scrape-off layer transport code, which is described in detail in chapter 4. The modeling setup of the simulations, as well as the argon seeded ASDEX Upgrade H-mode discharge on which the simulations are based, are discussed in chapter 5. An extensive dataset of simulations with different plasma parameters has been generated (cf. tables 5.1 and 5.2). The basic results of the simulations, presented in sections 6.2 and 6.3, agree well with the experimental observations, showing a considerably stronger core radiation with argon than with nitrogen, which is caused by the differences in the radiation efficiency. Consequently, argon seeding results in a significant temperature drop of up to 12 % in the plasma edge (i.e., at the pedestal top), compared to the unseeded reference case. Such a detrimental impact is not observed with nitrogen, where the temperature drop stays below 2 % at similar divertor conditions, i.e., with similar peak power loads and temperatures at the divertor targets. However, the simulations show that nitrogen results in a stronger fuel dilution in the plasma edge of $n_{D^+}/n_e \approx 76-80\,\%$, compared to argon with $n_{D^+}/n_e \approx 84-86\,\%$. The fuel dilution should be limited, as it reduces the maximum achievable fusion rate in a future fusion reactor. A trade-off between fuel dilution and pedestal top temperature drop can be achieved by mixing both impurities. Apart from this, no synergetic effects (like, e.g., a higher achievable total radiation fraction) are observed with mixed impurities. The different impurity species do not affect each other directly. However, they can affect each other indirectly, as one impurity species can modify the plasma background, which then can also have an impact on the radiative properties and the impurity transport of both species.

As indicated above, for impurities introduced into the plasma in order to cause radiative power dissipation in the divertor region, it is important that the impurities are well retained in the divertor volume, such that they do not dilute the main plasma. To asses the impurity retention in the divertor region, an important parameter is the divertor enrichment E, which is defined as the ratio of the impurity concentrations in the divertor region and in the plasma core. At moderate impurity seeding levels an exceptionally high argon enrichment is observed in the simulations in the outer divertor, with values around $E \approx 3$, whereas the enrichment does not exceed $E \approx 1.5$ for nitrogen. However, as a certain seeding level is exceeded, the argon enrichment in the outer divertor suddenly drops significantly (to $E \approx 1$), while at the same time it increases considerably in the inner divertor. To study this redistribution of the argon impurities from the outer to the inner divertor, a detailed analysis of the impurity transport and the divertor impurity retention was performed.

Regarding the impurity transport (section 6.4), the simulations show that the impurity seeding has a strong impact on the particle flow patterns in the SOL. Due to the friction between main and impurity ions, the impurities essentially follow the main ion flow, which is mainly determined by the sources and sinks of main ions in the plasma. While the major particle sink is the flow onto the divertor targets, the dominant contribution to the main ion sources is the ionization of recycled particles in the divertor region. The simulations reveal that due to their impact on the temperature in the divertor region, the impurities strongly affect the main ion ionization sources. Therefore, the impurity seeding has a strong impact on the main ion flow pattern, which consequently also affects the impurity transport. At low seeding levels, a flow reversal at the outer midplane position results in a situation in which ions (i.e., main ions as well as impurity ions) are not able to move from the outer divertor to the inner divertor through the SOL. However, due to the impact of the impurities on the particle flow pattern, at high seeding levels the situation is reversed, and ions are not able to move from the inner to the outer divertor. This qualitative change of the particle flow patterns is especially pronounced with argon seeding, where the redistribution of the impurities from the outer to the inner divertor becomes a self-enhancing process. Due to the different radiation efficiency, nitrogen has a stronger impact on the main ion ionization sources in the colder inner divertor compared to argon, and a weaker impact in the hotter outer divertor, which results in a weaker impact on the particle flow patterns and a less sudden impurity density redistribution. With both argon and nitrogen, the modification of the impurity flow pattern is additionally enhanced by an increasing thermal force acting on the impurities in the SOL, resulting in an increased drag of particles towards the inner divertor.

Regarding the divertor impurity retention (section 6.5), one has to consider the impurity ion flows in the divertor region and the ionization front position of the neutral impurities. According to the particle flow patterns (cf. figure 6.21), there is a stagnation point of the impurity ion flow in front of the divertor target in the near SOL. Directly in front of the divertor target the impurity ions stream towards the target plate. However, beyond the stagnation point they stream out of the divertor region towards the outer midplane. Therefore, impurities can only escape the divertor region if they are able to reach beyond the impurity stagnation point. For particles which are recycled at the divertor targets – which is the strongest particle source in the plasma – this is only possible if they are not ionized before they reach the stagnation point. Consequently, the divertor impurity retention is determined by the relative positions of the ionization front of the neutral impurities and the stagnation point of the impurity ion flow (cf. figure 6.23). A better divertor retention

can be expected for impurity species with a shorter neutral ionization mean free path. In the simulations the average mean free path within the outer divertor region is in the order of 6 cm for argon and around 9 cm for nitrogen. This explains the better argon divertor enrichment. Apart from the species dependence the neutral ionization front position is largely determined by the temperature, according to the ionization potential, whereas the stagnation point position is determined by the ratio of the thermal force acting on the impurities and the friction force between main and impurity ions. Both, ionization front and stagnation point are shifted away from the target with decreasing temperature, e.g., induced by increasing impurity seeding. To study the competition between these two mechanisms, a simplified model has been developed in section 6.5.3, which captures the key features relevant for the impact of different parameters on the stagnation point position. The results from this simplified model show, that with a reduction of the divertor temperature (i.e., with increasing impurity seeding), the divertor retention is reduced in all investigated cases.

With the modified impurity transport and the reduced outer divertor impurity retention at higher seeding levels, it is possible to explain the argon density redistribution from the outer to the inner divertor. The reason why the impurity density redistribution is less pronounced for nitrogen is the initially stronger nitrogen divertor leakage, due to its longer mean free path, and the weaker impact of the nitrogen impurities on the background plasma flow, as described above.

In summary, power exhaust remains a critical issue for future fusion devices. With the requirement of a minimal detrimental impact on the confined plasma, and at the same time a significant reduction of the peak heat loads and temperatures at the divertor targets, only a small operational window remains available. With the detailed numerical investigations of argon and nitrogen seeding, this work contributes to an increasing physical understanding of the impact of impurities on the plasma. This facilitates a further optimization of the impurity seeding recipe and the power exhaust scenario. The simulations can be used as a guidance for future numerical and experimental studies of impurity seeded plasmas, especially with mixed argon and nitrogen seeding, which are still required in order to find a final solution to the power exhaust challenge.

Appendix A

Difficulties and Limitations Encountered with the SOLPS 5.0 Code

Various issues can arise in the SOLPS numerical simulations and complicate or even prevent code convergence. Such difficulties can either be of real physical nature, be caused by the applied numerical methods, or simply be due to faulty user input. The symptoms can vary from crashing simulations or strange behavior of the plasma solution, to solutions which look perfectly valid and only reveal unphysical features under a more detailed investigation. The latter case is especially critical, as the problem might remain undetected and result in false interpretations of the simulation results. A few difficulties that were reported previously and especially issues that were encountered during the work on this thesis are discussed in this appendix.

A.1 Deficient Particle Balance at Low Particle Throughput

The issue of the deficient particle balance at low particle throughput has already been mentioned in sections 4.2.9 and 5.4. It is a problem which is known in the community, but for which no satisfactory solution could be provided so far. Also within the scope of this work the deficiency could not be resolved, even though several attempts have been made to improve the situation. For testing purposes a few already converged simulations were continued for more than 10^6 iterations, without any improvement of the particle balance, e.g., going from a nitrogen particle balance of 38.9 % in the original case to 39.1 %. Also different modifications of the input parameters could not solve the issue, and only a slight improvement could be achieved with a smaller time step, which however, still resulted in a very unsatisfactory particle balance.

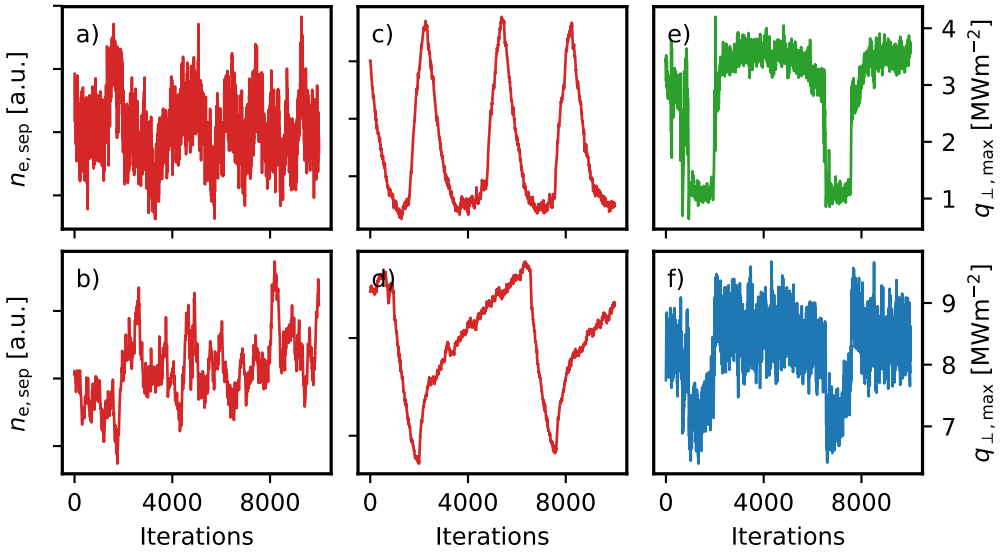

Figure A.1: Exemplary time traces of different SOLPS simulations: a) "Constant" time trace showing $n_{e,sep}$, illustrating the Monte Carlo noise introduced by EIRENE. b) Increasing $n_{e,sep}$ time trace, which is not considered as constant according to the convergence criterion applied in this work. c) Oscillating $n_{e,sep}$ time trace of a feed-forward simulation (i.e., without feedback). d) Fluctuating $n_{e,sep}$ time trace, and the corresponding fluctuating peak power flux to the inner (e) and outer (f) divertor target of the same simulation.

A.2 Parameter Oscillations and Fluctuations

In several cases oscillations and fluctuations of various plasma parameters can be observed in the simulations. One explanation for such an oscillating behavior can be a resonance in the feedback scheme. If this is the cause, the problem can often simply be solved by a modification of the specific reaction time of the feedback mechanism. However, in many cases the oscillations are persistent and a stable steady state solution in the specified parameter space does not seem to exist – even though sometimes a stable solution exists for an adjacent position in the input parameter space (e.g., at a slightly increased or decreased impurity seeding level). The persistence becomes evident, if one considers feed-forward simulations with constant deuterium fueling (i.e., simulations without a feedback mechanism activated), in which the oscillations can also be observed. An example for the $n_{e,sep}$ time trace of an oscillating feed-forward case is shown in figure A.1c, as well as a fluctuating

$n_{e,sep}$ time trace and the corresponding time traces of the peak power flux to the inner and outer divertor targets in figure A.1d-f.

Such oscillations have also been reported in [183], where a dataset of SOLPS 5.0 simulations was produced for an ITER-sized tokamak with constant fueling, without drifts, with fluid neutrals only (i.e., without EIRENE) and with aggressive charge state bundling. With this modeling setup the simulations are not very well comparable to the simulations performed in this work, however, also in this dataset up to 20 % of the simulations did not converge to a stationary solution, due to oscillations of the plasma parameters. According to [183] the oscillating behavior is not sensitive to a change of the time step or to the grid resolution, and hence, a physical origin of the oscillations is concluded. One explanation might be, that several different solutions exist for the particular set of input parameters or that the system is close to an instability, like a transition from high recycling to detached divertor conditions [156, 184, 185].

Under such conditions the maintenance of the simulations becomes quite challenging. In order to reach convergence, various small changes to the numerical input parameters (like the feedback scheme, number of internal iterations, the time step, etc.) have to be tested by trial and error. This, however, only leads to success in a few cases, and increases the total required time to reach convergence from a few weeks to several months (even without drifts), while often a stationary solution cannot be achieved at all. Additionally, the oscillations and fluctuations are often not detected as such in the automatic post-processing routines, and the simulations are continued for a long time before they are even identified as critical cases.

A.3 Dependence of the Numerical Solution on the Initial Plasma State and on Numerical Parameters

As indicated above, different solutions can exist for a given set of input parameters. However, in some cases the system does not jump from one solution to the other, but instead, the different solutions are numerically stable. This is illustrated in figure A.2, where electron density, electron temperature and ion temperature profiles are plotted, for two different simulations with completely identical input parameters which are fully converged (including almost perfect deuterium particle balance below 0.1 % and 0.7 %). Despite identical input parameters, the solutions differ considerably, especially for the ion temperature at the inner target, whereas the upstream profiles are roughly similar. The only difference between the two simulations is that they were started (several thousand iterations ago) from two different initial (converged)

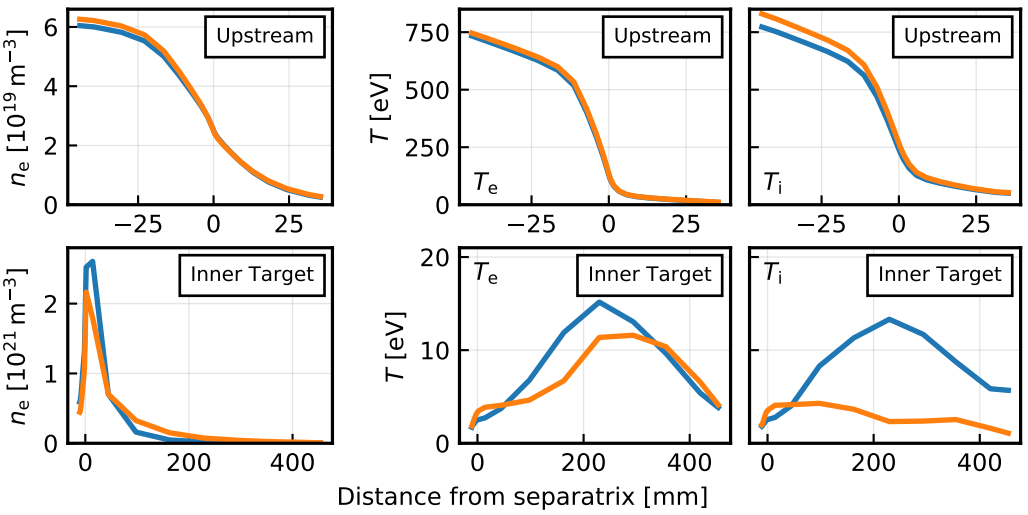

Figure A.2: Radial profiles of the electron density, electron temperature and ion temperature at the outer midplane and at the inner divertor target. Shown are two different fully converged simulations, that were performed with exactly identical input parameters. Nevertheless, the results differ considerably.

plasma states. This makes the interpretation and the reliability of the simulations difficult, as results are not necessarily directly reproducible. However, on the other hand, sometimes it is possible to facilitate convergence of a critical case (e.g., of an oscillating case, see above) if the simulation is restarted with an initial plasma state of a different converged simulation. In any case, if convergence is reached, the result is a numerically valid solution, even though it is not necessarily the only possible solution.

A similar problem can arise if only purely numerical input parameters differ, like the size of the time step, or the number of internal iterations, as it is also reported in [186]. As such parameters are only used internally in the code (e.g., for faster convergence), ideally, they should not affect the final outcome of the simulations. In the simulations discussed above and shown in figure A.2, also these parameters were exactly identical. However, for testing purposes in a few random samples also simulations have been performed, where the impact of such numerical input parameters on the simulation results was investigated. It is observed that in a parameter space where the simulations converge quickly and without complications, the plasma solutions are not sensitive to the numerical input parameters. However, in regions of the input parameter space where also complications occur, it can

be observed that a different choice of numerical input parameters also results in different plasma solutions, similar as it is shown in figure A.2.

A.4 Implications of the Encountered Limitations for the Simulation Results

Even though certain issues can arise when operating SOLPS 5.0, or any fluid plasma code, the simulations still provide numerically valid solutions to the equations solved in the code. Despite the discussed simplifications, assumptions or limitations, the physical processes which are included in the code, can still be investigated without restrictions and provide new and valid insight. Nevertheless, care has to be taken to ensure well convergence of the simulations, and in an ideal case the results should always be verified via experimental investigations, which unfortunately, is not always possible or feasible. However, even the mere identification of certain limitations of the code is an important step for the development and improvement of future code versions.

Appendix B

Acknowledgments

First of all I want to thank my academic supervisor Prof. Ulrich Stroth, for giving me the opportunity to work in such an interesting and active field of research, despite the fact, that I did not bring any previous knowledge in the field of fusion research. Of course, many thanks also go to my direct supervisor Marco Wischmeier, who patiently provided me with valuable support throughout the whole thesis. Without his advise and expertise this work would not have been possible.

Furthermore, I would also like to thank all of my (previous) office mates, and all the (former) colleagues at the IPP and also from other institutes, who were always happy to help, regarding various different issues. Thanks to all these people, I was able to thrive in a pleasant and enjoyable working environment.

Finally, I want to express my gratitude to all my friends and my family, and most of all to my precious girlfriend, for all the strong support during a challenging time.

Bibliography

[1] R. K. Pachauri and L. A. Meyer (eds.) *Climate Change 2014: Synthesis Report. Contribution of Working Groups I, II and III to the Fifth Assessment Report of the Intergovernmental Panel on Climate Change*. IPCC, Geneva, Switzerland, 2014.

[2] U.S. Energy Information Administration. *International Energy Outlook 2019*. Office of Energy Analysis, U.S. Department of Energy, 2019.

[3] N. Armaroli and V. Balzani. "The Future of Energy Supply: Challenges and Opportunities". In: *Angewandte Chemie International Edition* 46.1-2 (2006), pp. 52–66. DOI: 10.1002/anie.200602373.

[4] P. G. V. Sampaio and M. O. A. González. "Photovoltaic solar energy: Conceptual framework". In: *Renewable and Sustainable Energy Reviews* 74 (2017), pp. 590–601. DOI: 10.1016/j.rser.2017.02.081.

[5] E. Kabir et al. "Solar energy: Potential and future prospects". In: *Renewable and Sustainable Energy Reviews* 82.1 (2018), pp. 894–900. DOI: 10.1016/j.rser.2017.09.094.

[6] T. J. Hammons. "Integrating renewable energy sources into European grids". In: *International Journal of Electrical Power & Energy Systems* 30.8 (2008), pp. 462–475. DOI: 10.1016/j.ijepes.2008.04.010.

[7] W. F. Pickard. "Where renewable electricity is concerned, how costly is "too costly"?" In: *Energy Policy* 49 (2012), pp. 346–354. DOI: 10.1016/j.enpol.2012.06.036.

[8] G. Alva et al. "Thermal energy storage materials and systems for solar energy applications". In: *Renewable and Sustainable Energy Reviews* 68.1 (2017), pp. 693–706. DOI: 10.1016/j.rser.2016.10.021.

[9] A. Dreos et al. "Exploring the potential of a hybrid device combining solar water heating and molecular solar thermal energy storage". In: *Energy & Environmental Science* 10.3 (2017), pp. 728–734. DOI: 10.1039/C6EE01952H.

[10] Q. Li et al. "Solar energy storage in the rechargeable batteries". In: *Nano Today* 16 (2017), pp. 46–60. DOI: 10.1016/j.nantod.2017.08.007.

[11] V. D. Shafranov. "The initial period in the history of nuclear fusion research at the Kurchatov Institute". In: *Physics-Uspekhi* 44.8 (2001). DOI: 10.1070/PU2001v044n08ABEH001068.

[12] J. Ongena et al. "Magnetic-confinement fusion". In: *Nature Physics* 12 (2016), pp. 398–410. DOI: 10.1038/nphys3745.

[13] Max-Planck-Gesellschaft. *TECHMAX, Die Sonne im Tank - Wie Fusionsforscher das Feuer einfangen*. 2007. URL: https://www.max-wissen.de/230648/Techmax-09-Web.pdf.

[14] W. Bahm, I. Milch, and R. P. Schorn. *Kernfusion*. Hrsg.: IPP, FZK, FZJ. 2006.

[15] H.-S. Bosch and G.M. Hale. "Improved formulas for fusion cross-sections and thermal reactivities". In: *Nuclear Fusion* 32.4 (1992). DOI: 10.1088/0029-5515/32/4/I07.

[16] J. D. Lawson. "Some Criteria for a Power Producing Thermonuclear Reactor". In: *Proceedings of the Physical Society Section B* 70.1 (1957). DOI: 10.1088/0370-1301/70/1/303.

[17] E. I. Moses. "Ignition on the National Ignition Facility: a path towards inertial fusion energy". In: *Nuclear Fusion* 49.10 (2009). DOI: 10.1088/0029-5515/49/10/104022.

[18] B. Bigot. "Inertial fusion science in Europe". In: *Journal de Physique IV France* 133 (2006), pp. 3–8. DOI: 10.1051/jp4:2006133002.

[19] J. Lindl. "Development of the indirect-drive approach to inertial confinement fusion and the target physics basis for ignition and gain". In: *Physics of Plasmas* 2.3933 (1995). DOI: 10.1063/1.871025.

[20] H. J. Kull. "Theory of the Rayleigh-Taylor instability". In: *Physics Reports* 206.5 (1991), pp. 197–325. DOI: 10.1016/0370-1573(91)90153-D.

[21] IPP Grafik. URL: https://svcumulus.ipp.mpg.de/.

[22] R. C. Wolf et al. "Major results from the first plasma campaign of the Wendelstein 7-X stellarator". In: *Nuclear Fusion* 57.10 (2017). DOI: 10.1088/1741-4326/aa770d.

[23] H. Zohm. *Magnetohydrodynamic Stability of Tokamaks*. Wiley-VCH, 2015.

[24] M. Kotschenreuther et al. "Magnetic geometry and physics of advanced divertors: The X-divertor and the snowflake". In: *Physics of Plasmas* 20.102507 (2013). DOI: 10.1063/1.4824735.

[25] P. M. Valanju et al. "Super-X divertors and high power density fusion devices". In: *Physics of Plasmas* 16.056110 (2009). DOI: 10.1063/1.3110984.

[26] D. D. Ryutov et al. “The magnetic field structure of a snowflake divertor”. In: *Physics of Plasmas* 15.092501 (2008). DOI: 10.1063/1.2967900.

[27] D. D. Ryutov and V. A. Soukhanovskii. “The snowflake divertor”. In: *Physics of Plasmas* 22.110901 (2015). DOI: 10.1063/1.4935115.

[28] F. Wagner. “A quarter-century of H-mode studies”. In: *Plasma Physics and Controlled Fusion* 49.12B (2007). DOI: 10.1088/0741-3335/49/12B/S01.

[29] E. J. Doyle (Chair Transport Physics) et al. “Chapter 2: Plasma confinement and transport”. In: *Nuclear Fusion* 47.6 (2007). DOI: 10.1088/0029-5515/47/6/S02.

[30] ITER Physics Expert Group on Confinement, Transport, et al. “Chapter 2: Plasma confinement and transport”. In: *Nuclear Fusion* 39.12 (1999). DOI: 10.1088/0029-5515/39/12/302.

[31] H. Zohm. “Edge localized modes (ELMs)”. In: *Plasma Physics and Controled Fusion* 38.2 (1996). DOI: 10.1088/0741-3335/38/2/001.

[32] M. Keilhacker et al. “High fusion performance from deuterium-tritium plasmas in JET”. In: *Nuclear Fusion* 39.2 (1999). DOI: 10.1088/0029-5515/39/2/306.

[33] M. Shimada et al. “Progress in the ITER Physics Basis, Chapter 1: Overview and summary”. In: *Nuclear Fusion* 47.6 (2007). DOI: 10.1088/0029-5515/47/6/S01.

[34] G. Federici et al. “Overview of the design approach and prioritization of R&D activities towards an EU DEMO”. In: *Fusion Engineering and Design* 109–111 (2016), pp. 1464–1474. DOI: 10.1016/j.fusengdes.2015.11.050.

[35] V. Mukhovatov et al. “Chapter 9: ITER contributions for Demo plasma development”. In: *Nuclear Fusion* 47.6 (2007). DOI: 10.1088/0029-5515/47/6/S09.

[36] R. A. Pitts et al. “Physics basis for the first ITER tungsten divertor”. In: *Nuclear Materials and Energy* 20.100696 (2019). DOI: 10.1016/j.nme.2019.100696.

[37] F. Reimold et al. “Divertor studies in nitrogen induced completely detached H-modes in full tungsten ASDEX Upgrade”. In: *Nuclear Fusion* 55.3 (2015). DOI: 10.1088/0029-5515/55/3/033004.

[38] D. Naujoks et al. “Tungsten as target material in fusion devices”. In: *Nuclear Fusion* 36.6 (1996). DOI: 10.1088/0029-5515/36/6/I01.

[39] A. Loarte et al. In: *Nuclear Fusion* 47.6 (2007), S203–S263. DOI: 10.1088/0029-5515/47/6/S04.

[40] R. A. Pitts et al. "Physics basis and design of the ITER plasma-facing components". In: *Journal of Nuclear Materials* 415.1 (2011), S957–S964. DOI: 10.1016/j.jnucmat.2011.01.114.

[41] A. Kallenbach et al. "Impurity seeding for tokamak power exhaust: from present devices via ITER to DEMO". In: *Plasma Physics and Controlled Fusion* 55.12 (2013). DOI: 10.1088/0741-3335/55/12/124041.

[42] M. Wischmeier. "High density operation for reactor-relevant power exhaust". In: *Journal of Nuclear Materials* 463 (2015), pp. 22–29. DOI: 10.1016/j.jnucmat.2014.12.078.

[43] J. P. Gunn et al. "Surface heat loads on the ITER divertor vertical targets". In: *Nuclear Fusion* 57.4 (2017). DOI: 10.1088/1741-4326/aa5e2a.

[44] K.-U. Riemann. "Plasma—sheath transition and Bohm criterion". In: *Contributions to Plasma Physics* 32.3-4 (1992), pp. 231–236. DOI: 10.1002/ctpp.2150320309.

[45] P. C. Stangeby. *The Plasma Boundary of Magnetic Fusion Devices*. 2000. DOI: 10.1201/9781420033328.

[46] H. P. Summers. *The ADAS user manual*. 2004.

[47] M. Siccinio et al. "Impact of an integrated core/SOL description on the R and BT optimization of tokamak fusion reactors". In: *Nuclear Fusion* 58.1 (2018). DOI: 10.1088/1741-4326/aa9583.

[48] T. Pütterich et al. "Determination of the tolerable impurity concentrations in a fusion reactor using a consistent set of cooling factors". In: *Nuclear Fusion* 59.5 (2019). DOI: 10.1088/1741-4326/ab0384.

[49] P. G. Carolan and V. A. Piotrowicz. "The behaviour of impurities out of coronal equilibrium". In: *Plasma Phys.* 25.10 (1983). DOI: 10.1088/0032-1028/25/10/001.

[50] J. F. Drake. "Marfes: Radiative condensation in tokamak edge plasma". In: *The Physics of Fluids* 30.2429 (1987). DOI: 10.1063/1.866133.

[51] K. Shimizu, T. Takizuka, and A. Sakasai. "A review on impurity transport in divertors". In: *Journal of Nuclear Materials* 241–243 (1997), pp. 167–181. DOI: 10.1016/S0022-3115(97)80038-4.

[52] P. J. Harbour and J. G. Morgan. "The Transport of Impurity Ions in a Scrape-off Plasma". In: *Controlled Fusion and Plasma Physics (Proc. 11th Eur. Conf. Aachen, 1983), Vol. 7D, Part II, European Physical Society* (1983), pp. 427–430.

[53] J. Neuhauser et al. "Modelling of impurity flow in the tokamak scrape-off layer". In: *Nuclear Fusion* 24.1 (1984). DOI: 10.1088/0029-5515/24/1/004.

[54] P. C. Stangeby and J. D. Elder. "Impurity retention by divertors. I. One dimensional models". In: *Nuclear Fusion* 35.11 (1995). DOI: 10.1088/0029-5515/35/11/I06.

[55] I. Yu. Senichenkov et al. "On mechanisms of impurity leakage and retention in the tokamak divertor". In: *Plasma Physics and Controlled Fusion* 61.4 (2019). DOI: 10.1088/1361-6587/ab04d0.

[56] A. Kallenbach et al. "Partial detachment of high power discharges in ASDEX Upgrade". In: *Nuclear Fusion* 55.5 (2015). DOI: 10.1088/0029-5515/55/5/053026.

[57] F. Reimold. "Experimental Studies and Modeling of Divertor Plasma Detachment in H-Mode Discharges in the ASDEX Upgrade Tokamak". PhD thesis. Technische Universität München (TUM), 2014.

[58] S. Potzel et al. "Characterization of the fluctuating detachment state in ASDEX Upgrade". In: *Journal of Nuclear Materials* 438 (2013), S285–S290. DOI: 10.1016/j.jnucmat.2013.01.048.

[59] J. Roth, K. Krieger, and G. Fussmann. "Divertor retention for recycling impurities". In: *Nuclear Fusion* 32.10 (1992). DOI: 10.1088/0029-5515/32/10/I11.

[60] G. M. McCracken et al. "Impurity transport in the divertor of the Alcator C-Mod tokamak". In: *Journal of Nuclear Materials* 220–222 (1995), pp. 264–268. DOI: 10.1016/0022-3115(94)00425-0.

[61] J. A. Goetz et al. "High confinement dissipative divertor operation on Alcator C-Mod". In: *Physics of Plasmas* 6.1899 (1999). DOI: 10.1063/1.873447.

[62] H. Kubo et al. "Radiation enhancement and impurity behavior in JT-60U reversed shear discharges". In: *Journal of Nuclear Materials* 313–316 (2003), pp. 1197–1201. DOI: 10.1016/S0022-3115(02)01531-3.

[63] P. Monier-Garbet et al. "Impurity-seeded ELMy H-modes in JET, with high density and reduced heat load". In: *Nuclear Fusion* 45.11 (2005). DOI: 10.1088/0029-5515/45/11/022.

[64] T. W. Petrie et al. “Compatibility of the radiating divertor with high performance plasmas in DIII-D”. In: *Journal of Nuclear Materials* 363–365 (2007), pp. 416–420. DOI: 10.1016/j.jnucmat.2007.01.131.

[65] T. W. Petrie et al. “Impurity behaviour under puff-and-pump radiating divertor conditions”. In: *Nuclear Fusion* 49.6 (2009). DOI: 10.1088/0029-5515/49/6/065013.

[66] C. Giroud et al. “Integration of a radiative divertor for heat load control into JET high triangularity ELMy H-mode plasmas”. In: *Nuclear Fusion* 52.6 (2012). DOI: 10.1088/0029-5515/52/6/063022.

[67] C. Giroud et al. “Impact of nitrogen seeding on confinement and power load control of a high-triangularity JET ELMy H-mode plasma with a metal wall”. In: *Nuclear Fusion* 53.11 (2013). DOI: 10.1088/0029-5515/53/11/113025.

[68] S. Potzel et al. “Formation of the high density front in the inner far SOL at ASDEX Upgrade and JET”. In: *Journal of Nuclear Materials* 463 (2015), pp. 541–545. DOI: 10.1016/j.jnucmat.2014.12.008.

[69] C. Guillemaut et al. “Real-time control of divertor detachment in H-mode with impurity seeding using Langmuir probe feedback in JET-ITER-like wall”. In: *Plasma Physics and Controlled Fusion* 59.4 (2017). DOI: 10.1088/1361-6587/aa5951.

[70] M. Bernert et al. “Power exhaust by SOL and pedestal radiation at ASDEX Upgrade and JET”. In: *Nuclear Materials and Energy* 12 (2017), pp. 111–118. DOI: 10.1016/j.nme.2016.12.029.

[71] D. Brunner et al. “Surface heat flux feedback controlled impurity seeding experiments with Alcator C-Mod’s high-Z vertical target plate divertor: performance, limitations and implications for fusion power reactors”. In: *Nuclear Fusion* 57.8 (2017). DOI: 10.1088/1741-4326/aa7923.

[72] M. G. Dunne. “Impact of impurity seeding and divertor conditions on transitions, pedestal structure and ELMs”. In: *Nuclear Fusion* 57.2 (2017). DOI: 10.1088/0029-5515/57/2/025002.

[73] S. S. Henderson et al. *Report of T17-AUG (2018): Optimisation of seeded detachment regimes with multiple species towards high confinement, high radiation and robust control using ITER/DEMO relevant observers and actuators*. Presentation. 2018.

[74] S. Glöggler et al. “Characterisation of highly radiating neon seeded plasmas in JET-ILW”. In: *Nuclear Fusion* 59.12 (2019). DOI: 10.1088/1741-4326/ab3f7a.

[75] P. H. Rebut, R. J. Bickerton, and B. E. Keen. “The Joint European Torus: installation, first results and prospects”. In: *Nuclear Fusion* 25.9 (1985). DOI: 10.1088/0029-5515/25/9/003.

[76] G. F. Matthews et al. “JET ITER-like wall—overview and experimental programme*”. In: *Physica Scripta* 2011 (2011). DOI: 10.1088/0031-8949/2011/T145/014001.

[77] I. H. Hutchinson et al. “First results from Alcator-C-MOD*”. In: *Physics of Plasmas* 1.1511 (1994). DOI: 10.1063/1.870701.

[78] E. S. Marmar. “The Alcator C-Mod Program”. In: *Fusion Science and Technology* 51 (2007), pp. 261–265. DOI: 10.13182/FST07-A1421.

[79] Y. Lin et al. “Hydrogen control in Alcator C-Mod walls and plasmas”. In: *Journal of Nuclear Materials* 363–365 (2007), pp. 920–924. DOI: 10.1016/j.jnucmat.2007.01.115.

[80] J. L. Luxon. “A design retrospective of the DIII-D tokamak”. In: *Nuclear Fusion* 42.5 (2002). DOI: 10.1088/0029-5515/42/5/313.

[81] H. Ninomiya et al. “JT-60 upgrade device for confinement and steady state studies”. In: *Plasma Devices and Operations* 1.1 (1990), pp. 43–65. DOI: 10.1080/10519999008225528.

[82] P. Barabaschi, Y. Kamada, and H. Shirai. “Progress of the JT-60SA project”. In: *Nuclear Fusion* 59.11 (2019). DOI: 10.1088/1741-4326/ab03f6.

[83] Wan Yuanxi, Li Jiangang, and Weng Peide. “First Engineering Commissioning of EAST Tokamak”. In: *Plasma Science and Technology* 8.3 (2006). DOI: 10.1088/1009-0630/8/3/01.

[84] B. LaBombard et al. “Scaling of the power exhaust channel in Alcator C-Mod”. In: *Physics of Plasmas* 18.056104 (2011). DOI: 10.1063/1.3566059.

[85] F. Reimold et al. “The high field side high density region in SOLPS-modeling of nitrogen-seeded H-modes in ASDEX Upgrade”. In: *Nuclear Materials and Energy* 12 (2017), pp. 193–199. DOI: 10.1016/j.nme.2017.01.010.

[86] S. Potzel et al. “On the high density in the HFS far SOL at ASDEX Upgrade and its impact on plasma confinement”. In: (2015). EPS 2015, Lisbon, Portugal.

[87] A. Kallenbach et al. “Divertor power load feedback with nitrogen seeding in ASDEX Upgrade”. In: *Plasma Physics and Controlled Fusion* 52.5 (2010). DOI: 10.1088/0741-3335/52/5/055002.

[88] J. Schweinzer et al. “Confinement of ’improved H-modes’ in the all-tungsten ASDEX Upgrade with nitrogen seeding”. In: *Nuclear Fusion* 51.11 (2011). DOI: 10.1088/0029-5515/51/11/113003.

[89] M. Kikuchi. “A note on the Mirnov signal analysis in tokamaks”. In: *Nuclear Fusion* 26.1 (1986). DOI: 10.1088/0029-5515/26/1/009.

[90] P. J. McCarthy, P. Martin, and W. Schneider. *The CLISTE Interpretive Equilibrium Code*. IPP-Report 5/85. Max-Planck-Institut für Plasmaphysik, Garching, 1999. URL: http://hdl.handle.net/11858/00-001M-0000-0027-6023-D.

[91] P. J. McCarthy. “Analytical solutions to the Grad–Shafranov equation for tokamak equilibrium with dissimilar source functions”. In: *Physics of Plasmas* 6.3554 (1999). DOI: 10.1063/1.873630.

[92] J. Illerhaus. *Estimation, Validation and Uncertainty of the Position of the Separatrix Contour at ASDEX Upgrade*. Diploma Thesis, Technische Universität München. Max-Planck-Institut für Plasmaphysik, 2019. DOI: 10.17617/2.3049518.

[93] H. Murmann et al. “The Thomson scattering systems of the ASDEX upgrade tokamak”. In: *Review of Scientific Instruments* 63.4941 (1992). DOI: 10.1063/1.1143504.

[94] A. W. DeSilva. “The Evolution of Light Scattering as a Plasma Diagnostic”. In: *Contributions to Plasma Physics* 40.1-2 (2000). DOI: 10.1002/(SICI)1521-3986(200004)40:1/2<23::AID-CTPP23>3.0.CO;2-7.

[95] J. Schweinzer et al. “Reconstruction of plasma edge density profiles from Li I (2s-2p) emission profiles”. In: *Plasma Physics and Controlled Fusion* 34.7 (1992). DOI: 10.1088/0741-3335/34/7/001.

[96] R. Fischer, E. Wolfrum, and J. Schweinzer. “Probabilistic lithium beam data analysis”. In: *Plasma Physics and Controlled Fusion* 50.8 (2008). DOI: 10.1088/0741-3335/50/8/085009.

[97] S. K. Rathgeber et al. “Estimation of edge electron temperature profiles via forward modelling of the electron cyclotron radiation transport at ASDEX Upgrade”. In: *Plasma Physics and Controlled Fusion* 55.2 (2013). DOI: 10.1088/0741-3335/55/2/025004.

[98] A. Mlynek et al. “Design of a digital multiradian phase detector and its application in fusion plasma interferometry”. In: *Review of Scientific Instruments* 81.033507 (2010). DOI: 10.1063/1.3340944.

[99] S. Potzel et al. “Electron density determination in the divertor volume of ASDEX Upgrade via Stark broadening of the Balmer lines”. In: *Plasma Physics and Controlled Fusion* 56.2 (2014). DOI: 10.1088/0741-3335/56/2/025010.

[100] B. A. Lomanowski et al. “Inferring divertor plasma properties from hydrogen Balmer and Paschen series spectroscopy in JET-ILW”. In: *Nuclear Fusion* 55.12 (2015). DOI: 10.1088/0029-5515/55/12/123028.

[101] A. Yu Pigarov, J. L. Terry, and B. Lipschultz. “Study of the discrete-to-continuum transition in a Balmer spectrum from Alcator C-Mod divertor plasmas”. In: *Plasma Physics and Controlled Fusion* 40.12 (1998). DOI: 10.1088/0741-3335/40/12/006.

[102] A. Kallenbach et al. “Neutral pressure and separatrix density related models for seed impurity divertor radiation in ASDEX Upgrade”. In: *Nuclear Materials and Energy* 18 (2019), pp. 166–174. DOI: 10.1016/j.nme.2018.12.021.

[103] S. S. Henderson et al. “Determination of volumetric plasma parameters from spectroscopic N II and N III line ratio measurements in the ASDEX Upgrade divertor”. In: *Nuclear Fusion* 58.1 (2018). DOI: 10.1088/1741-4326/aa96be.

[104] S. S. Henderson et al. “An assessment of nitrogen concentrations from spectroscopic measurements in the JET and ASDEX upgrade divertor”. In: *Nuclear Materials and Energy* 18 (2019), pp. 147–152. DOI: 10.1016/j.nme.2018.12.012.

[105] M. Bernert. “Analysis of the H-mode density limit in the ASDEX Upgrade tokamak using bolometry”. PhD thesis. Ludwig-Maximilians-Universität München, 2013.

[106] L. Giannone et al. “Prototype of a radiation hard resistive bolometer for ITER”. In: *Plasma Physics and Controlled Fusion* 47.12 (2005). DOI: 10.1088/0741-3335/47/12/004.

[107] M. Bernert et al. “Application of AXUV diode detectors at ASDEX Upgrade”. In: *Review of Scientific Instruments* 85.033503 (2014). DOI: 10.1063/1.4867662.

[108] B. Sieglin et al. “Real time capable infrared thermography for ASDEX Upgrade”. In: *Review of Scientific Instruments* 86.113502 (2015). DOI: 10.1063/1.4935580.

[109] A. Herrmann et al. “Energy flux to the ASDEX-Upgrade diverter plates determined by thermography and calorimetry”. In: *Plasma Physics and Controlled Fusion* 37.1 (1995). DOI: 10.1088/0741-3335/37/1/002.

[110] G. Haas and H-S. Bosch. “In vessel pressure measurement in nuclear fusion experiments with asdex gauges”. In: *Vacuum* 51.1 (1998), pp. 39–46. DOI: 10.1016/S0042-207X(98)00131-6.

[111] A. Scarabosio et al. “Measurements of neutral gas fluxes under different plasma and divertor regimes in ASDEX Upgrade”. In: *Journal of Nuclear Materials* 390–391 (2009), pp. 494–497. DOI: 10.1016/j.jnucmat.2009.01.057.

[112] M. Weinlich. *Elektrostatische Sonden in starken Magnetfeldern*. Technical Report IPP 5/64. Garching: Max-Planck-Institut für Plasmaphysik, Dec. 1995.

[113] M. Weinlich and A. Carlson. “Flush mounted probes in ASDEX Upgrade - Can they be operated as triple probes?” In: *Contributions to Plasma Physics* 36 (1996), pp. 53–60. DOI: 10.1002/ctpp.19960360109.

[114] A. Kallenbach et al. “Electric currents in the scrape-off layer in ASDEX Upgrade”. In: *Journal of Nuclear Materials* 290–293 (2001), pp. 639–643. DOI: 10.1016/S0022-3115(00)00445-1.

[115] B. Streibl et al. “Chapter 2: Machine Design, Fueling, and Heating in ASDEX Upgrade”. In: *Fusion Science and Technology* 44 (2003), pp. 578–592. DOI: 10.13182/FST03-A400.

[116] B. Streibl et al. “Operational behaviour of the ASDEX upgrade in-vessel cryo pump”. In: *Fusion Engineering and Design* 56-57 (2001), pp. 867–872. DOI: 10.1016/S0920-3796(01)00368-4.

[117] H. Zohm et al. “On the physics guidelines for a tokamak DEMO”. In: *Nuclear Fusion* 53.7 (2013). DOI: 10.1088/0029-5515/53/7/073019.

[118] F. Hitzler et al. “Impurity transport and divertor retention in Ar and N seeded SOLPS 5.0 simulations for ASDEX Upgrade”. In: *Plasma Physics and Controlled Fusion* (2020). DOI: 10.1088/1361-6587/ab9b00.

[119] R. M. McDermott et al. “Evaluation of impurity densities from charge exchange recombination spectroscopy measurements at ASDEX Upgrade”. In: *Plasma Physycs and Controlled Fusion* 60.9 (2018). DOI: 10.1088/1361-6587/aad256.

[120] A. Järvinen et al. “Simulations of tungsten transport in the edge of JET ELMy H-mode plasmas”. In: *Journal of Nuclear Materials* 438 (2013), S1005–S1009. DOI: 10.1016/j.jnucmat.2013.01.219.

[121] M. S. Islam, Y. Nakashima, and A Hatayama. “Investigation of plasma behavior during noble gas injection in the end-cell of GAMMA 10/PDX by using the multi-fluid code ’LINDA’”. In: *Plasma Physics and Controlled Fusion* 59.12 (2017). DOI: 10.1088/1361-6587/aa8d02.

[122] X. J. Liu et al. “Modeling study of radiation characteristics with different impurity species seeding in EAST”. In: *Physics of Plasmas* 24.122509 (2017). DOI: 10.1063/1.4997101.

[123] L. Xiang et al. “Modeling of argon seeding in ASDEX Upgrade H-mode plasma with SOLPS5.0”. In: *Nuclear Materials and Energy* 12 (2017), pp. 1146–1151. DOI: 10.1016/j.nme.2017.02.017.

[124] D. Hailong et al. “Exploring SF- in-out asymmetry and detachment bifurcation in HL-2M with ExB by SOLPS”. In: *Nuclear Materials and Energy* 22.100719 (2020). DOI: 10.1016/j.nme.2019.100719.

[125] O. Pan et al. “SOLPS-ITER modeling with activated drifts for a snowflake divertor in ASDEX Upgrade”. In: *Plasma Physics and Controlled Fusion* (2020). DOI: 10.1088/1361-6587/ab7108.

[126] Zhong-Ping Chen et al. “SOLPS-ITER modeling of boosted carbon radiation through non-coronal effects in an X-divertor facilitating detachment in DIII-D”. In: *Nuclear Fusion* (2020). DOI: 10.1088/1741-4326/ab71bc.

[127] E. Sytova et al. “Comparing N versus Ne as divertor radiators in ASDEX-upgrade and ITER”. In: *Nuclear Materials and Energy* 19 (2019), pp. 72–78. DOI: 10.1016/j.nme.2019.02.019.

[128] S. Yamoto et al. “Simulation study of mixed-impurity seeding with extension of integrated divertor code SONIC”. In: *Plasma Physics and Controlled Fusion* 62.4 (2020). DOI: 10.1088/1361-6587/ab6f9b.

[129] R. Schneider et al. “Plasma Edge Physics with B2-Eirene”. In: *Contributions to Plasma Physics* 46 (2006). DOI: 10.1002/ctpp.200610001.

[130] S. Wiesen et al. “The new SOLPS-ITER code package”. In: *Journal of Nuclear Materials* 463 (2015), pp. 480–484. DOI: 10.1016/j.jnucmat.2014.10.012.

[131] X. Bonnin et al. “Presentation of the New SOLPS-ITER Code Package for Tokamak Plasma Edge Modelling”. In: *Plasma and Fusion Research* 11 (2016), p. 1403102. DOI: 10.1585/pfr.11.1403102.

[132] R. Simonini et al. “Models and Numerics in the Multi-Fluid 2-D Edge Plasma Code EDGE2D/U”. In: *Contributions to Plasma Physics* 34 (1994), pp. 368–373. DOI: 10.1002/ctpp.2150340242.

[133] T. D. Rognlien et al. “2-D Fluid Transport Simulations of Gaseous/Radiative Divertors”. In: *Contributions to Plasma Physics* 34 (1994), pp. 362–367. DOI: 10.1002/ctpp.2150340241.

[134] M. Borchardt et al. “W7-X edge modelling with the 3D SOL fluid code BoRiS”. In: *Journal of Nuclear Materials* 290–293 (2001), pp. 546–550. DOI: 10.1016/S0022-3115(00)00593-6.

[135] P. Tamain et al. “The TOKAM3X code for edge turbulence fluid simulations of tokamak plasmas in versatile magnetic geometries”. In: *Journal of Computational Physics* 321 (2016), pp. 606–623. DOI: 10.1016/j.jcp.2016.05.038.

[136] Y. Feng et al. “A 3D Monte Carlo code for plasma transport in island divertors”. In: *Journal of Nuclear Materials* 241–243 (1997), pp. 930–934. DOI: 10.1016/S0022-3115(97)80168-7.

[137] D. Brida et al. “Heat flux pattern in detached L-modes and ELM mitigated H-modes with rotating magnetic perturbations in ASDEX Upgrade”. In: *Nuclear Fusion* 57.11 (2017). DOI: 10.1088/1741-4326/aa78b9.

[138] D.P. Coster et al. “An overview of JET edge modelling activities”. In: *Journal of Nuclear Materials* 313–316 (2003), pp. 868–872. DOI: 10.1016/S0022-3115(02)01466-6.

[139] D. Reiter. *The EIRENE code, version: January 1992: users manual*. Tech. rep. Juel-2599. Forschungszentrum Jülich, 1992.

[140] S. Wiesen et al. “EDGE2D/EIRENE code interface report”. In: (2006). JET ITC-Report. URL: http://www.eirene.de/e2deir_report_30jun06.pdf.

[141] Y. Feng, F. Sardei, and J. Kisslinger. “3D fluid modelling of the edge plasma by means of a Monte Carlo technique”. In: *Journal of Nuclear Materials* 266–269 (1999), pp. 812–818. DOI: 10.1016/S0022-3115(98)00844-7.

[142] U. Stroth. *Plasmaphysik Phänomene, Grundlagen und Anwendungen*. 2nd edition. Springer, 2018.

[143] L. Spitzer and R Härm. “Transport Phenomena in a Completely Ionized Gas”. In: *Physical Review* 89.5 (1953), p. 977. DOI: 10.1103/PhysRev.89.977.

[144] R. Balescu. *Transport processes in plasmas*. North Holland, New York, 1988.

[145] D. P. Coster et al. *SOLPS 5.0 User Manual*. 2015.

[146] V. Kotov, D. Reiter, and A. S. Kukushkin. *Numerical study of the ITER divertor plasma with the B2-EIRENE code package*. Jül-4257. Forschungszentrums Jülich GmbH, Jülich, Germany, 2007.

[147] A.V. Chankin, D.P. Coster, and G. Meisl. "Development and Benchmarking of a New Kinetic Code for Plasma Periphery (KIPP)". In: *Contributions to Plasma Physics* 52.5-6 (2012), pp. 500–504. DOI: 10.1002/ctpp.201210039.

[148] M. Zhao. "Towards a More Complete Description of Tokamak Edge Plasmas: SOLPS Simulations with Kinetic Electron Effects". Max-Planck-Institut für Plasmaphysik. PhD thesis. Technische Universität München (TUM), 2018.

[149] M. Zhao, A. Chankin, and D. Coster. "SOLPS simulations with electron kinetic effects". In: *Plasma Physics and Controlled Fusion* 61.2 (2019). DOI: 10.1088/1361-6587/aaf4ea.

[150] D. A. D'Ippolito et al. "Blob Transport in the Tokamak Scrape-off-Layer". In: *Contributions to Plasma Physics* 44.1-3 (2004), pp. 205–216. DOI: 10.1002/ctpp.200410030.

[151] D. A. D'Ippolito, J. R. Myra, and S. J. Zweben. "Convective transport by intermittent blob-filaments: Comparison of theory and experiment". In: *Physics of Plasmas* 18.060501 (2011). DOI: 10.1063/1.3594609.

[152] L. Casali et al. "Modelling of nitrogen seeding experiments in the ASDEX Upgrade tokamak". In: *Physics of Plasmas* 25.032506 (2018). DOI: 10.1063/1.5019913.

[153] T. Pütterich et al. "ELM flushing and impurity transport in the H-mode edge barrier in ASDEX Upgrade". In: *Journal of Nuclear Materials* 415 (2011), pp. 334–339. DOI: 10.1016/j.jnucmat.2010.09.052.

[154] J. E. Allen. "The plasma–sheath boundary: its history and Langmuir's definition of the sheath edge". In: *Plasma Sources Science and Technology* 18.1 (2009). DOI: 10.1088/0963-0252/18/1/014004.

[155] M. Blommaert et al. "A spatially hybrid fluid-kinetic neutral model for SOLPS-ITER plasma edge simulations". In: *Nuclear Materials and Energy* 19 (2019), pp. 28–33. DOI: 10.1016/j.nme.2019.01.022.

[156] D. Reiter et al. "The EIRENE and B2-EIRENE codes". In: *Fusion Science and Technology* 47 (2005).

[157] D. Reiter. *The EIRENE Code User Manual*. Tech. rep. Forschungszentrum Jülich, 2019.

[158] D. Reiter. *The data file AMJUEL: Additional Atomic and Molecular Data for EIRENE*. FZ, Forschungszentrum Jülich GmbH. 2011.

[159] D. Reiter. *The data file HYDHEL: Atomic and Molecular Data for EIRENE based upon: Janev, Langer, Evans, Post, "Elementary Processes in Hydrogen-Helium Plasmas", Springer 1987*. FZ, Forschungszentrum Jülich GmbH.

[160] D. Reiter. *The data file METHANE: Additional Atomic and Molecular Data for EIRENE*. FZ, Forschungszentrum Jülich GmbH. 2013.

[161] S. Wiesen et al. *SOLPS Development for ITER Design Work: Upgrading from SOLPS4 to SOLPS5*. Report. Forschungszentrum Jülich GmbH, IEK-4 Plasmaphysik, 2013.

[162] V. Kotov and D. Reiter. *B2-B2.5 Code Benchmarking, Part III: Convergence issues of the B2-EIRENE code*. Institut für Energie- und Klimaforschung, Berichte des Forschungszentrums Jülich, Plasmaphysik (IEK-4), Jül-4371, 2014.

[163] E. Kaveeva et al. "Speed-up of SOLPS-ITER code for tokamak edge modeling". In: *Nuclear Fusion* 58.12 (2018). DOI: 10.1088/1741-4326/aae162.

[164] D. Eldon et al. "Controlling marginally detached divertor plasmas". In: *Nuclear Fusion* 57.6 (2017). DOI: 10.1088/1741-4326/aa6b16.

[165] M. Wensing et al. "SOLPS-ITER simulations of the TCV divertor upgrade". In: *Plasma Physics and Controlled Fusion* 61.8 (2019). DOI: 10.1088/1361-6587/ab2b1f.

[166] M. Wensing et al. "X-point potential well formation in diverted tokamaks with unfavorable magnetic field direction". In: *Nuclear Fusion* 60.5 (2020). DOI: 10.1088/1741-4326/ab7d4f.

[167] YiPing Chen et al. "SOLPS-ITER modelling of SOL-Divertor plasmas with different configurations in EAST". In: *Nuclear Fusion* (2020). DOI: 10.1088/1741-4326/ab69e3.

[168] G. Meisl et al. "Implantation and erosion of nitrogen in tungsten". In: *New Journal of Physics* 16.093018 (2014). DOI: 10.1088/1367-2630/16/9/093018.

[169] S. I. Krasheninnikov et al. "Divertor plasma detachment". In: *Physics of Plasmas* 23.055602 (2016). DOI: 10.1063/1.4948273.

[170] A. A. Pshenov, A. S. Kukushkin, and S. I. Krasheninnikov. "Energy balance in plasma detachment". In: *Nuclear Materials and Energy* 12 (2017), pp. 948–952. DOI: 10.1016/j.nme.2017.03.019.

[171] M. L. Reinke. “Heat flux mitigation by impurity seeding in high-field tokamaks”. In: *Nuclear Fusion* 57.3 (2017). DOI: 10.1088/1741-4326/aa5145.

[172] R. Perillo et al. “Studying the influence of nitrogen seeding in a detached-like hydrogen plasma by means of numerical simulations”. In: *Plasma Physics and Controlled Fusion* 60.10 (2018). DOI: 10.1088/1361-6587/aad703.

[173] A. Drenik et al. “Evolution of nitrogen concentration and ammonia production in N2-seeded H-mode discharges at ASDEX Upgrade”. In: *Nuclear Fusion* 59.4 (2019). DOI: 10.1088/1741-4326/aafe23.

[174] N. Ezumi et al. “Synergistic effect of nitrogen and hydrogen seeding gases on plasma detachment in the GAMMA 10/PDX tandem mirror”. In: *Nuclear Fusion* 59.6 (2019). DOI: 10.1088/1741-4326/ab1a4a.

[175] G. Meisl et al. “Nitrogen retention in ASDEX Upgrade”. In: *Journal of Nuclear Materials* 463 (2015), pp. 668–671. DOI: 10.1016/j.jnucmat.2014.10.031.

[176] F. Reimold et al. “Experimental studies and modeling of complete H-mode divertor detachment in ASDEX Upgrade”. In: *Journal of Nuclear Materials* 463 (2015), pp. 128–134. DOI: 10.1016/j.jnucmat.2014.12.019.

[177] R. Dux et al. “Transport of tungsten in the H-mode edge transport barrier of ITER”. In: *Plasma Physics and Controlled Fusion* 56.12 (2014). DOI: 10.1088/0741-3335/56/12/124003.

[178] A.V. Chankin. “Classical drifts in the tokamak SOL and divertor: models and experiment”. In: *Journal of Nuclear Materials* 241–243 (1997), pp. 199–213. DOI: 10.1016/S0022-3115(97)80040-2.

[179] N. Asakura. “Understanding the SOL flow in L-mode plasma on divertor tokamaks, and its influence on the plasma transport”. In: *Journal of Nuclear Materials* 363–365 (2007), pp. 41–51. DOI: 10.1016/j.jnucmat.2006.12.029.

[180] A.V. Chankin and D.P. Coster. “The role of drifts in the plasma transport at the tokamak core–SOL interface”. In: *Journal of Nuclear Materials* 438 (2013), S463–S466. DOI: 10.1016/j.jnucmat.2013.01.094.

[181] L. Aho-Mantila et al. “Assessment of SOLPS5.0 divertor solutions with drifts and currents against L-mode experiments in ASDEX Upgrade and JET”. In: *Plasma Physics and Controlled Fusion* 59.3 (2017). DOI: 10.1088/1361-6587/59/3/035003.

[182] A. V. Chankin et al. “Interpretation of SOL flows and target asymmetries in JET using EDGE2D code calculations”. In: *Journal of Nuclear Materials* 290-293 (2001), pp. 518–524. DOI: 10.1016/S0022-3115(00)00516-X.

[183] D. P. Coster. “Characterization of oscillations observed in reduced physics SOLPS simulations”. In: *Contributions to Plasma Physics* 58.6-8 (2018), pp. 666–674. DOI: 10.1002/ctpp.201700159.

[184] A. S. Kukushkin and S. I. Krasheninnikov. “Bifurcations and oscillations in divertor plasma”. In: *Plasma Physics and Controlled Fusion* 61.7 (2019). DOI: 10.1088/1361-6587/ab1bba.

[185] P. Heinrich et al. “Self-sustained divertor oscillations in ASDEX Upgrade”. In: *Nuclear Fusion* 60.7 (2020). DOI: 10.1088/1741-4326/ab8a05.

[186] V. Kotov. *Non-local effect of saturated residuals in B2-EIRENE (SOLPS) simulations*. Presentation. 2016.